Reconstruction of Extensive Air Showers and Measurement of the Cosmic Ray Energy Spectrum in the Range of 1 – 80 PeV at the South Pole

DISSERTATION

zur Erlangung des akademischen Grades
doctor rerum naturalium
(Dr. rer. nat.)
im Fach Physik

eingereicht an der
Mathematisch-Naturwissenschaftlichen Fakultät I
Humboldt-Universität zu Berlin

von
Herr Dipl.-Phys. Stefan Klepser
geboren am 26.11.1977 in Heilbronn-Neckargartach

Präsident der Humboldt-Universität zu Berlin:
Prof. Dr. Dr. h. c. Christoph Markschies

Dekan der Mathematisch-Naturwissenschaftlichen Fakultät I:
Prof. Dr. Lutz-Helmut Schön

Gutachter:

1. Prof. Dr. Hermann Kolanoski
2. Prof. Dr. Thomas K. Gaisser
3. Prof. Dr. Thomas Lohse

eingereicht am:	24.04.2008
Tag der mündlichen Prüfung:	24.06.2008

Abstract

IceTop is a km^2 scale detector array for highly energetic cosmic radiation. It is a part of the IceCube Observatory that is presently being built at the geographic South Pole. It aims for the detection of huge particle cascades induced by PeV cosmic rays in the atmosphere. These extensive air showers are detected by cylindrical ice tanks that collect the Cherenkov light produced by penetrating particles. The main goal of IceTop is the investigation of the energy distribution and chemical composition of PeV to EeV cosmic rays. This thesis presents the first analysis of highly energetic cosmic ray data taken with IceTop.

First, the light response of the IceTop tanks is parametrised as a function of energy and particle type. An expectation function for the distribution of shower signals in the detector plane is developed. The likelihood fit based on that can reconstruct the recorded shower events with resolutions of 1.5 ° in direction, 9 m in location of the shower center, and 12 % in energy. This is well competitive with other experiments.

The resulting energy response of the array is studied to set up response matrices for different primary nuclei and inclinations. These allow for a deconvolution of the distribution of reconstructed energies to derive the real energy spectrum. Two unfolding algorithms are implemented and studied, and response matrices are modeled for four different composition assumptions. With each assumption, energy spectra are unfolded for three different bins in inclination, using a data sample with an exposure of $3.86 \cdot 10^{11}\,\mathrm{m}^2\,\mathrm{s}\,\mathrm{sr}$, taken in August 2007. The range of the spectrum is $1 - 80\,\mathrm{PeV}$.

Finally, a new analysis method is developed that uses the fact that cosmic rays in the PeV range are expected to be isotropic. It is shown that this requirement can be used for a likelihood estimation that is sensitive to composition without using additional information from other detector components. The analysis shows a clear preference of the mixed composition models over pure proton or iron assumption.

The spectrum with the highest likelihood shows good agreement with results from other experiments within the systematic uncertainties. The found position of the so-called knee feature is $3.1 \pm 0.3\,(\mathrm{stat.}) \pm 0.3\,(\mathrm{sys.})$ PeV, the power indices before and after that are $\gamma_1 = -2.71 \pm 0.07\,(\mathrm{stat.})$ and $\gamma_2 = -3.110 \pm 0.014\,(\mathrm{stat.}) \pm 0.08\,(\mathrm{sys.})$.

Keywords:
IceCube, IceTop, Energy Spectrum, Cosmic Rays

Zusammenfassung

IceTop ist ein Detektorfeld für hochenergetische kosmische Strahlung, das momentan am geographischen Südpol errichtet wird. Es ist ein Teil des IceCube-Observatoriums und wird nach Fertigstellung eine Fläche von einem Quadratkilometer überspannen. Es zielt auf den Nachweis hochenergetischer Teilchenkaskaden ab, die von kosmischer Strahlung mit Energien im PeV-Bereich induziert werden. Diese Luftschauer werden mit Hilfe zylindrischer Eistanks aufgezeichnet, in denen von den Sekundärteilchen produziertes Tscherenkov-Licht gemessen wird. Die vorliegende Dissertation beinhaltet die erste Analyse hochenergetischer kosmischer Strahlung mit dem IceTop-Detektor.

Zunächst wird hierfür die Lichtausbeute der Detektortanks in Abhängigkeit von Energie und Teilchensorte parametrisiert. Dies ermöglicht die Erstellung einer Funktion zur Beschreibung der Erwartungswertverteilung der Schauersignale in der Detektorebene, und eines entsprechenden Anpassungsverfahrens, dass zur Rekonstruktion der Schauer verwendet wird. Die damit erreichten Auflösungen sind $1{,}5\,^\circ$ in der Richtung, $9\,\mathrm{m}$ in der Position des Schauerzentrum, und etwa $12\,\%$ in der Primärnergie, was vergleichbar ist mit denen anderer Experimente derselben Größe.

Nachdem die Ereignisrekonstruktion verifiziert wurde, wird das Ansprechverhalten von IceTop im Bezug auf die Energie genauer evaluiert. Aus den Ergebnissen werden Faltungsmatrizen für unterschiedliche Primärteilchensorten und Zenithwinkel-Abschnitte extrahiert. Diese können dazu dienen, unter einer bestimmten Primär-Kompositionsannahme eine Entfaltung der gemessenen Verteilungen vorzunehnehmen, was zum tatsächlichen Energiespektrum führt.

Zu diesem Zweck werden zwei Entfaltungsalgorithmen vorgestellt, und vier unterschiedliche Faltungsmatrizen für verschiedene Kompositionsannahmen berechnet. Im August 2007 genommene Daten mit einer Exposition von $3{,}86 \cdot 10^{11}\,\mathrm{m}^2\,\mathrm{s}\,\mathrm{sr}$ werden in drei Zenithwinkel-Abschnitte eingeteilt und separat mit den vier Kompositionsmodellen entfaltet. Die gewonnenen Spektren decken einen Energiebereich von $1 - 80\,\mathrm{PeV}$ ab.

Um die Ergebnisse auszuwerten, wird die Tatsache zu Hilfe genommen, dass der Fluss der kosmischen Strahlung im PeV-Bereich vollkommen isotrop zu erwarten ist. Mit dieser Forderung lassen sich Wahrscheinlichkeiten definieren, die sensitiv sind auf die Konsistenz, und somit auf die Korrektheit der Kompositionsannahmen. Diese neue Methode ermöglicht prinzipiell eine

Untersuchung der Komposition ohne Zuhilfenahme weiterer Detektorkomponenten. Die Analyse zeigt eine klare Präferenz der Modelle mit gemischter Komposition.

Schließlich wird das Spektrum mit der höchsten relativen Wahrscheinlichkeit mit Ergebnissen aus anderen Experimenten verglichen. Die gemessenen Parameter stimmen innerhalb der systematischen Unsicherheiten gut überein. Die ermittelte Position des sogenannten Knies des Spektrums ist $3{,}1 \pm 0{,}3\,(\text{stat.}) \pm 0{,}3\,(\text{sys.})\,\text{PeV}$, die Exponenten davor und danach sind $\gamma_1 = -2{,}71 \pm 0{,}07\,(\text{stat.})$ und $\gamma_2 = -3{,}110 \pm 0{,}014\,(\text{stat.}) \pm 0{,}08\,(\text{sys.})$.

Schlagwörter:
IceCube, IceTop, Energiespektrum, Kosmische Strahlung

Contents

Preface

> *"Ein Stück der großen Dunkelheit, der die Städte wie leuchtender Christbaumschmuck aufgesteckt sind, war in die Straßen gesickert und teilte den wenigen, die es aushalten konnten, etwas über die Weite unbewohnter Räume mit, über das Universum und dessen vollkommene Unabhängigkeit von aller menschlicher Existenz*[1]*."*
>
> Juli Zeh,
> *Spieltrieb*

Observing the universe is one of the first scientific disciplines ever pursued. Probably the sky and its large variety of nightly features was observed ever since, and definitely long before the first telescope was invented in the 17th century, which strongly enhanced the visibility of astronomical objects. Yet two hundred years passed by before astronomers discovered that stars cannot only be seen in the light that human eyes percept, but also in other wavelengths. Each new detector that enabled astrophysicists to observe the known stars in a new light band led to the discovery of new objects, unobserved in the previously investigated wavelengths. The latest examples of this for instance are the unidentified TeV gamma ray sources discovered by ground based Cherenkov telescopes.

Besides photon-based observations of the universe, charged cosmic rays have by now become important messengers of distant objects of various types. They have been discovered in 1912 by the Austrian Victor Hess [1], and were extensively studied in different energy regimes and with many different detection techniques. In contrast to photon observations, charged cosmic rays, mainly being protons and heavier nuclei, are deflected by magnetic or electric fields, such as those of our Galaxy, the Sun, or of the Earth.

Thus they do not carry any direction information when they arrive at Earth, which makes it impossible to assign a measured particle to its actual source. In fact, the flux of cosmic rays is highly diffuse for most energies. Only at ultrahigh energies, when particles have sufficient momentum to penetrate the typical magnetic fields between and inside galaxies without deflection, the radiation might actually serve for real astronomy.

Because of its isotropy, the main fields of investigation in high energy cosmic ray physics are the study of the energy spectrum, and the examination of the chemical composition. Both analyses deliver information about possible production processes and therewith the possible source objects of the particles. IceTop is a new square kilometer detector under construction at the South Pole, with hard- and software still being developed. This thesis will be devoted to the reconstruction of the energies of cosmic ray particles and the extraction of an initial energy spectrum with IceTop data taken in 2007.

In the introductory chapter, an overview will be given on the phenomenology of charged cosmic rays and the air shower generation that makes it possible to detect them at high energies. Furthermore, some of the currently discussed models to explain their acceleration and propagation will be shortly outlined. In chapter 2, the IceCube Observatory will be introduced with a focus on the IceTop part of it, which is dedicated to charged cosmic ray physics, but also has other functions. The data of the IceTop experiment, including the acquisition, processing and interpretation of it, is subject of chapter 3. Chapter 4 will present a detector simulation of different particle responses that will be used to develop air shower reconstruction algorithms in chapter 5. An analytic characterisation of the IceTop energy response, and the measured distributions of reconstructed energy are discussed in chapter 6. To interpret these, two unfolding algorithms that can be applied on the measured distributions are introduced in chapter 7. Based on all that, the final result of this thesis, an all-particle energy spectrum will be derived in chapter 8, using one month of 2007 IceTop data. This reveals a sensitivity of the analysis to the chemical composition. The final results will be summarised in the last chapter.

---

[1] Some part of the big darkness, that the cities are attached to like shining christmas lights, had oozed into the streets and was telling those who could bear it about the vastness of uninhabited spaces, about the universe and its complete independence of any human existence.

Chapter 1

Charged Cosmic Rays

1.1 Overview

Cosmic rays have been observed in an energy range that covers 10 orders of magnitude, starting at some hundreds of MeV, and ending at around $2 \cdot 10^{20}$ eV, where the flux becomes too low to be measured with presently available experimental devices. Figure 1.1 shows a compilation of measured spectra for all energies and several particle types [2]. The flux in the GeV range is partly of solar origin and up to $\sim 10\,\text{GeV}$ fluctuates in time, following the solar wind [3]. Also, this regime is influenced by the Earth's magnetic field, so the radiation is not isotropic but has an east-west anisotropy [4]. The flux of these particles per unit area, solid angle and time, $I = d^5N/dA\,d\Omega\,dt$, is high enough to be measured for different particle types directly in balloon and satellite experiments. This allows very precise measurements of the energy spectra of all occuring particles.

The energy spectra of all nuclei show an increase up to several GeV, and after that follow a power law decrease

$$\frac{dI}{dE} = I_0 \left(\frac{E}{E_0}\right)^{\gamma} . \tag{1.1}$$

Here, I_0 is the differential flux at E_0. The power index γ is around -2.7 up to the end of the directly measurable energy range at several hundreds of TeV. At low energies, protons are the most abundant particles (86%), followed by helium (11%) and heavier nuclei. At the higher end of the spectrum, the relative helium abundance with respect to the protons is increasing, which, following the power indices given in [5] or [6], might lead to a crossing of the two spectra at an energy of some tens of TeV.

This, and the further evolution of the spectrum, can only be measured indirectly, since the fluxes are too low and require a much larger detection

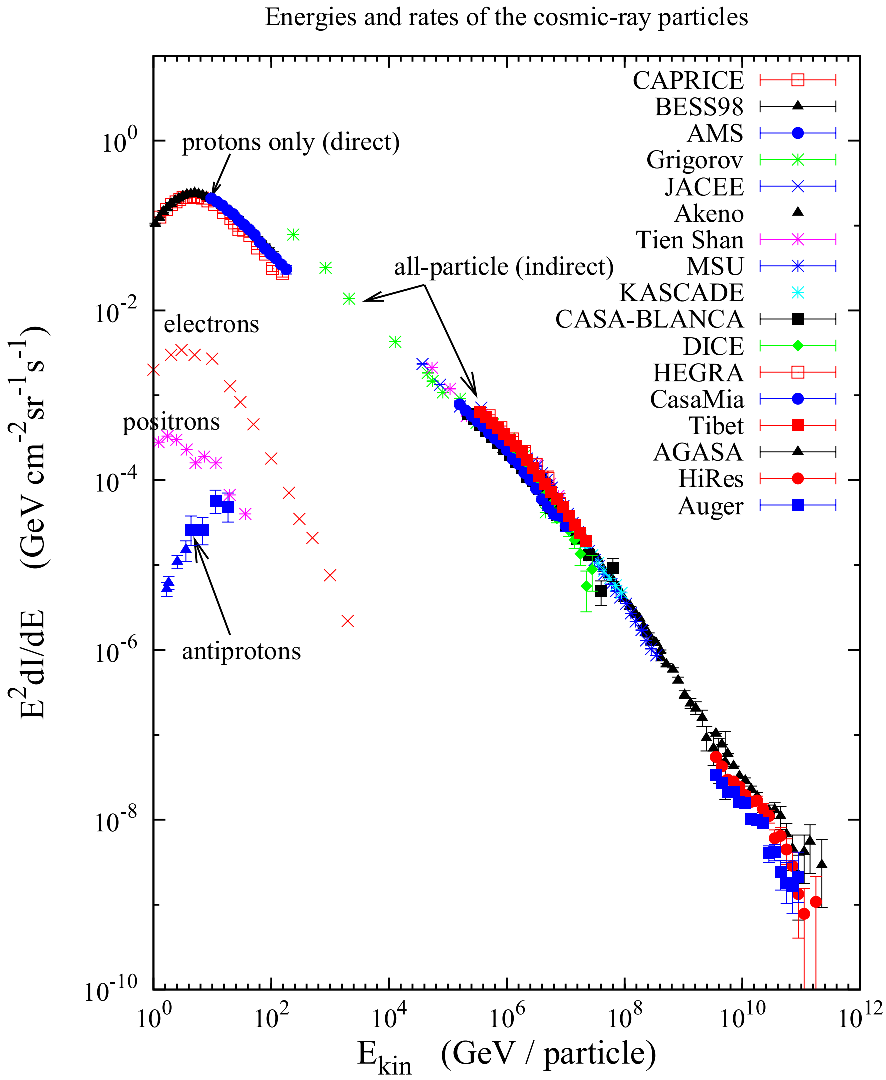

Figure 1.1: Energy spectra of different types of cosmic rays as shown in [2]. The nuclei are dominant above leptonic and antimatter fluxes. In this and most of the following plots, the data points are multiplied by a power of E to emphasise the features of the spectra.

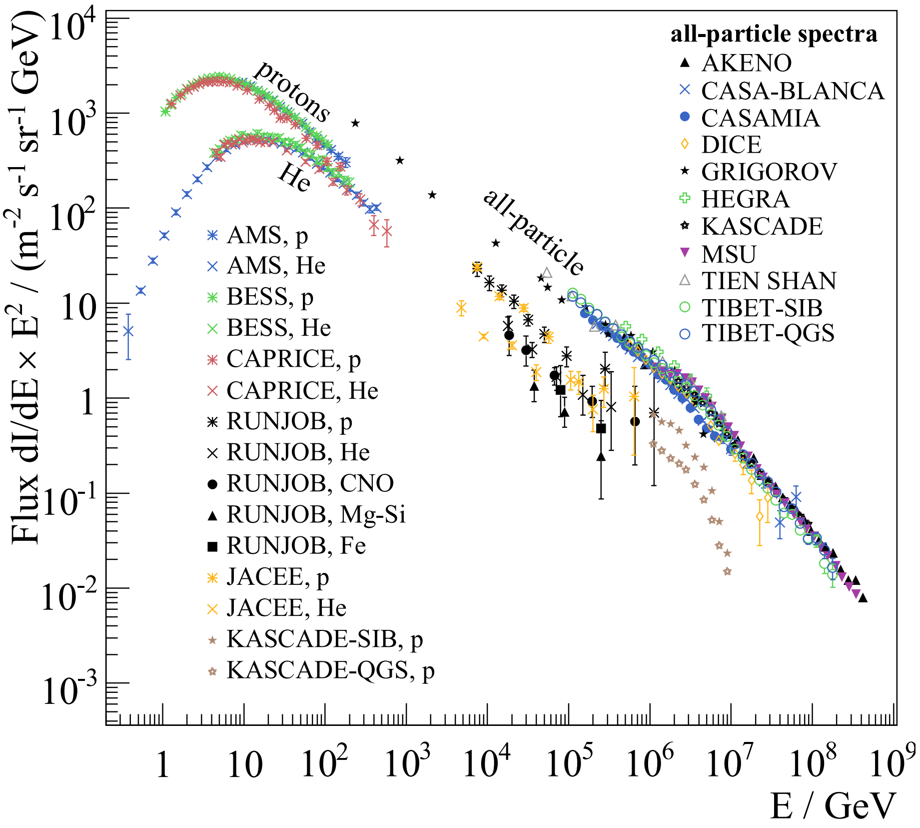

Figure 1.2: Energy spectrum of different nuclei from direct and indirect measurements. Heavier nuclei are less abundant than lighter ones. The plotted data were compiled by [7].

area than is possible to deploy on a satellite or balloon. As will be described in section 1.5, techniques were developed to indirectly detect high energy cosmic rays using the atmosphere as a converter volume and measuring huge particle showers that are induced by the primary particles. In fig. 1.2, the absolute all-particle fluxes measured by air shower experiments and satellites is shown with some additional data for different nuclei both from direct and indirect measurements. The data from indirect measurements still have high uncertainties and indicate an absolute flux that is somewhat above what one would expect if the directly measured data are extrapolated. This discrepancy indicates probable systematic misinterpretations in the energy assignment at high energy.

Figure 1.3 shows a comparison of energy spectra measured in several air shower experiments. All of the measured spectra have a power index change at around 4.5 PeV [6] from -2.7 to about -3.0 (“knee”), and two more at 400 PeV and $\sim$ 4 EeV, moving first to -3.3 (“second knee”) and then back to -2.6 (“ankle”). Very recently, two of the few experiments at EeV energies confirmed one more index change at 30 EeV to -4.1 [8] and -5.1 [9], respectively (“GZK feature”). The reasons of all these kinks are still under discussion and some possible explanations will be introduced in the following sections.

The crucial information needed to verify or rule out theoretical models that try to explain the evolution of the spectrum is the development of the chemical composition of the particles. This, however, is very difficult to measure, and existing publications of spectra for different nuclei are still strongly dependent on the high energy hadronic interaction models that are needed to simulate the interactions of the primary particles in the atmosphere. These simulations at present cannot be experimentally verified because all of the mentioned features of the spectrum are in an energy range not yet accessible to presently operating accelerator experiments (LHC at CERN might soon shed light on this though). Still, the few experiments that tried to do a composition analysis (e.g. [10, 11]) see indications for an increase of the average particle mass between the knee and the second knee. At ultra-high energies, fluorescence telescope measurements of shower maxima distributions suggest a decrease of the average mass up to some EeV, above which it rises anew [12].

1.2 Sources

There are two basic classes of models for the generation of high energy cosmic rays. The first are actual astrophysical sources, which can be subdi-

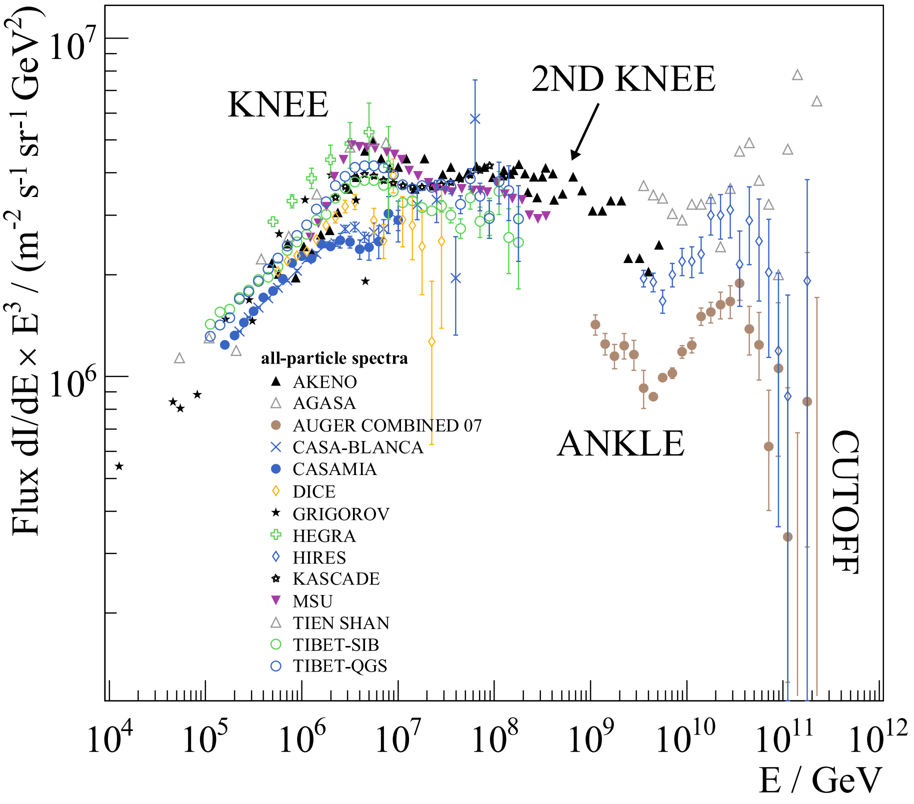

Figure 1.3: Energy spectra at high energies measured by different experiments. The systematic deviations are relatively large, but the basic kink features can be seen in all spectra. The plotted data were compiled by [7].

vided into nearby sources within our own galaxy, and distant extragalactic sources. The other class are so-called top-down models, which explain the creation of cosmic rays for example by the decay of unknown heavy particles or other effects predicted by new physics theories.

1.2.1 Fermi Acceleration

Most of the conventional source models are built on the idea that charged particles can be accelerated by elastic deflections either in turbulent magnetic fields such as in moving plasma clouds or in huge sudden shock fronts in very high-powered processes as for example supernovae.

The basic principle of these acceleration models is that a particle entering one of the mentioned clouds or shock fronts is assumed to be scattered without collision and can escape with a certain probability P_{esc} and a certain energy gain $E_1 = (1+\xi)E_0$ due to the movement of the cloud or shock. If that movement is at a supersonic velocity β, the factors ξ can be shown to be

$$\begin{aligned} \xi_{\text{shock}} &= \frac{4}{3}\beta \\ \xi_{\text{cloud}} &= \frac{4}{3}\beta^2. \end{aligned} \tag{1.2}$$

Depending on the power of β, the acceleration is refered to as 1st order or 2nd order Fermi acceleration. Interacting multiple times can thus lead to high energies, which of course is less probable the higher the amount of encounters gets. Quantitatively, this leads to a power law

$$\frac{dN}{dE} \propto \left(\frac{E}{E_0}\right)^{\frac{\ln(1-P_{\text{esc}})}{\ln(1+\xi)}-1} \tag{1.3}$$

whose index is determined by the escape probability and energy gain per interaction. According to e.g. [13, 14], power indices around $2.2 - 2.5$ can be regarded most realistic, depending on how relativistic the shock is, and other parameters. Also, the interactions of cosmic rays on their way to Earth give reasons for the source spectrum to be harder than the observed spectrum on Earth. From this, also a somewhat smaller number than the measured 2.7 seems realistic (see sec. 1.3).

Supernovae and Supernova Remnants (SNR)

The sources most frequently discussed for galactic cosmic rays with energies up to several hundreds of PeV are supernovae and their remnants. The typical chemical development of a star starts with very light elements like hydrogen or helium, which are abundant in the dust of star-forming areas. Subsequently, the light nuclei are fused, starting in the core of the star, such that spherical shells evolve for different chemical elements up to iron. This enables the large steady energy outflow of stars in terms of light and other radiation and leads to a growing heavy core in the centre of the star. Depending on its mass and other parameters, there are a lot of different classes of supernovae, and models that explain how they eventually emerge from a star that has become old and dense. Good and compact overviews can be found in [15, 16].

In general, when the star is burnt out and if it has sufficient mass, it can collapse and develop a compact, degenerate neutron gas in its centre. The complete collapsing mass outside the core is then bounced back in a huge shock front. This shock expands at sub-relativistic velocities (mostly $< 0.1c$) for typically some hundred years, and can accelerate other particles via the Fermi mechanism described above. The result is a supernova remnant with a size of several parsec and cosmic ray particles accelerated up to $\approx 10^{17}$ eV [17].

Active Galactic Nuclei (AGNs)

To explain energies above $\sim 10^{17}$ eV, extragalactic sources have to be taken into account. One of the most probable candidates are AGNs, which due to present models consist of a supermassive black hole in their centre, an accretion disc around it and two jets that develop perpendicular to the disc (fig. 1.4). The central part of an AGN, from which the jets evolve, is approximately of the size of the solar system, hence its optical appearance is similar to that of a star, except that in addition it produces high energetic photons in the X-ray and gamma ray regime [18].

Depending on the angle between jet and the axis of observation, the mass of the black hole, the amount of accreted mass and other parameters, AGNs are classified into several categories. Some of the most promising candidates of cosmic ray acceleration are Quasars, Radiogalaxies and BL Lacertae objects, which differ mainly in their time variability and the ratio between radiation in the radio and optical band.

There are different models for each type of AGN under discussion, many of which predict particle acceleration up to EeV energies, especially from BL Lac objects (e.g. [19]).

Very recently, the hypothesis of AGNs being the sources of UHECRs found strong support by an analysis of data from the Auger Observatory. A strong indication for a flux anisotropy was found towards the supergalactic

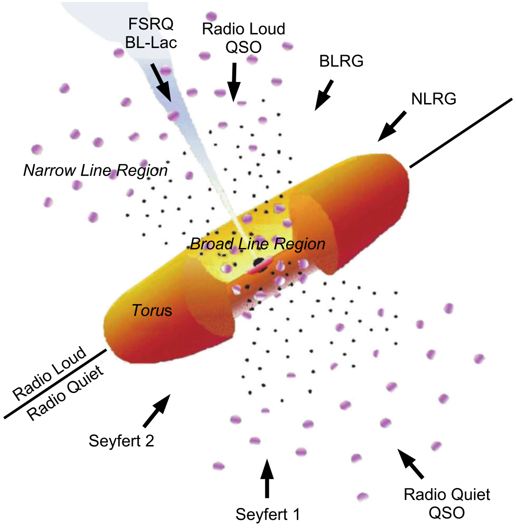

Figure 1.4: Sketch of the classification scheme of AGNs. The jets that are perpendicular to the accretion disc might produce an outflow of ultra-high energetic particles.

plane, where many nearby AGNs are located [20].

Gamma Ray Bursts (GRBs)

Gamma Ray Bursts are extremely energetic and short outbursts of radiation first discovered in 1967 by the Vela satellites in the gamma-ray band [21]. Most of these outbursts last between 10^{-3} s to 10^{3} s, which strongly limits the size of the progenitor objects. By now, they are thus widely believed to be caused by the collapse of the core of a massive star or the subsequent mergers of two remnant compact cores. Their isotropic distribution furthermore suggests an extragalactic origin.

Many models that describe GRBs are in one way or the other based on the occurence of a shock front that, by prompt gamma-ray emmission, produces the spectra observed by gamma ray satellites. This implies the acceleration of electrons, which are expected to have a power law spectrum. If this is the case, one would also expect hadrons to be accelerated by the same mechanism [22]. Some models, described in the same reference, even try to explain the currently observed flux of ultra high energy cosmic rays (UHECR).

A way to prove this theory would be to detect coincidences between gamma ray detections of GRBs and ultra high energy cosmic rays that have sufficient energy not to be deflected substantially by galactic magnetic fields. This is only possible with devices such as the Auger observatory [23], which focus on the EeV energy regime.

Clusters of Galaxies

Clusters of galaxies usually consist of 50-1000 galaxies that can move at high velocities and are probably bound by the gravitational force of dark matter, or the presence of yet another force besides gravity. Besides the galaxies and dark matter, galaxy clusters contain a large amount of hot intergalactic gas that emits X-rays.

When clusters of galaxies, or similar large-scale structures, collide, simulations of structure formation predict huge accretion shock waves at their boundaries. If magnetic fields are present at these shocks, particle acceleration should take place [24], which can be expected to contribute to the flux of UHECR up to some tens of EeV [25]. The recent X-ray and radio observations of galaxy clusters, for example in [26], seem to support this possibility.

1.2.2 Top-Down Models

Besides the acceleration based models, a huge amount of so-called top-down scenarios are discussed in literature, some of which are described and compared in [27, 28]. The basic idea is that high energy cosmic rays are not accelerated (bottom-up), but are created in the decay of certain massive particles, generically called “X particles”. In most theories, these X particles originate from some highly energetic process in the early universe. For example, some Grand Unified Theories and superstring theories predict topological defects such as magnetic monopoles or domain walls [28] that could potentially have sufficient energy to produce the observed particle flux. However, very few indications and no clear evidence of phenomena like that could so far be observed. In [13], it is even claimed that cosmic ray physics seem to become less exciting for the seekers of the exotic and that there was as yet no necessity for new physics at the highest energies.

Besides exclusive top-down and bottom-up creation of cosmic radiation, also hybrid scenarios are discussed, mainly explaining the lower energy regimes by acceleration and the ultra-high energies by top-down production. The apparent presence of the later discussed GZK feature, however, does not support the necessity of such a hybrid model, either.

1.3 Propagation

The observed flux of cosmic ray particles is always a product of a source spectrum and a spectrum that describes the effects of the propagation of the particles. On their way from the source to the detector, the particles might undergo various possible interactions. This can cause different effects, depending on particle type, energy and source location.

For example, if a particle of charge Ze and a momentum p traverses a magnetic field B, it is deflected and goes on curves with the gyromagnetic radius of

$$\rho = \frac{p}{eZB} = \frac{R}{cB}, \tag{1.4}$$

which only depends on the rigidity

$$R = \frac{pc}{Ze}. \tag{1.5}$$

and the magnetic field. Here, c is the speed of light. In the following, the rigidity is therefore a convenient quantity to characterise the escape probabilities and, connected to that, the spectral features of different particles.

1.3.1 Galactic Diffusion

For charged particles up to energies of some tens of PeV, the galactic magnetic fields are assumed to have the main quantitative impact on their propagation and deflection. Modelling this propagation has become a wide field of research, as for example reviewed in [29]. Studies of the issue either approach from the particle point-of-view, including spectral development and interaction, or treat the cosmic rays as a weightless collisionless relativistic gas with pressure and energy, and considering it alongside other components of the interstellar medium.

The propagation equation for a particular particle species can be written as

$$\begin{aligned}\frac{\partial\psi(\vec{r},p,t)}{\partial t} =& \overbrace{q(\vec{r},p,t)}^{\text{sources}} + \nabla\cdot(\overbrace{D_{xx}\nabla\psi}^{\text{diffusion}} - \overbrace{\vec{V}\psi}^{\substack{\text{(galactic wind)}\\ \text{convection}}}) + \overbrace{\frac{\partial}{\partial p}p^2 D_{pp}\frac{\partial}{\partial p}\frac{1}{p^2}\psi}^{\text{diffusive reacceleration}} \\ & - \underbrace{\frac{\partial}{\partial p}\left[\dot{p}\psi - \frac{p}{3}(\nabla\cdot\vec{V})\psi\right]}_{\substack{\text{adiabatic momentum}\\ \text{gain/loss}}} - \underbrace{\frac{1}{\tau_f}\psi}_{\text{spallation}} - \underbrace{\frac{1}{\tau_r}\psi}_{\text{radioactive decay}} .\end{aligned} \tag{1.6}$$

where $\psi(\vec{r},p,t)$ is the cosmic ray density per unit of particle momentum p and position $\vec{r}$, D_{xx} and D_{pp} are the diffusion coefficients in space and momentum space (including also diffuse reacceleration), $\vec{V}$ is the convection velocity, τ_f and τ_r are the time constants of radioactive decay and fragmentation. The meaning of the various terms of this equation, as described in detail in the reference, is indicated with the braces and cannot be discussed in detail here. The reason to yet state it is to give an idea on what the various calculations of CR propagation are based on. Finding the steady-state solution of the time-dependent eq. 1.6 can be done either by setting $\frac{\partial\psi}{\partial t} = 0$ or by numerically simulate the propagation until a steady state is actually reached. Mostly, the latter is pursued, assuming certain boundary conditions or approximations of the different terms in eq. 1.6.

In any case, particles of high rigidity at some point can not be contained in the gas anymore, since they escape the magnetic fields. This, in most models, leads to the occurrence of a rigidity dependent knee [30]. Furthermore, the indices of the primary source spectra can be expected to be softened by $\Delta\gamma \approx 0.6 - 0.7$.

1.3.2 Extragalactic Interactions

An effect on larger propagation scales is that particles can interact with the extragalactic background light (EBL) or with the cosmic microwave background (CMB). The interaction with the EBL is only crucial for gamma ray observations because it surpresses the propagation of gamma rays at and above TeV energies (e.g. [31]). For protons and other charged nuclei, the increasing cross section with CMB photons at EeV energies (fig. 1.5) most probably leads to the strong power index steepening of the energy spectrum

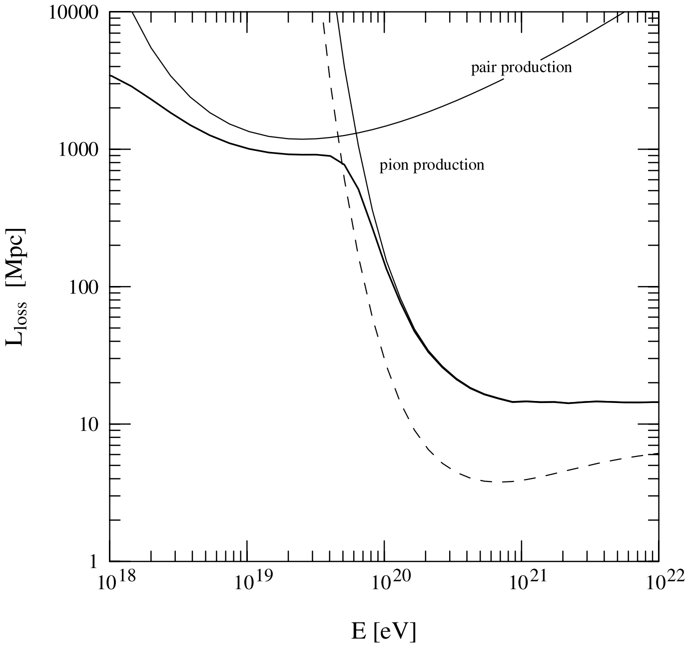

Figure 1.5: Energy loss length of protons in interactions with the CMB [32]. The contribution of pair production $p+\gamma \rightarrow p+e^{+}+e^{-}$ is weaker and at lower energies than the pion production at the delta resonance $p+\gamma \rightarrow \Delta(1230) \rightarrow p+\pi$. The dashed line shows the proton interaction length.

at 30 EeV, often refered to as the GZK feature. Consequently, only the neutral, light neutrinos are able to propagate through large intergalactic distances without being bent or absorbed.

1.4 Knee Models

In general two classes of models for the occurrence of the knee can be found in literature. The first class tries to deduce the knee from different combinations of the above acceleration and propagation effects, the other class seeks explanation in the indirect measurement techniques used to estimate the particle energy.

In the first class, it is either possible to explain the knee by increasing particle escape in the diffusion theories (see sec. 1.3.1), or simply due to the limited acceleration power of SNR [33];

The second class is based on the fact that the energy determination of highly energetic cosmic rays is mostly based on the detection of huge air showers whose simulation includes cross sections at energies far beyond what is known from accelerator experiments. New physics phenomena predict the production of unknown, undetected particles that could for example lead to a misinterpretation of the particle densities and thus the total energy of the shower. Two examples of such “exotic models” are the assumption of energy dissipation by enhanced multi-hadron production at knee energies [34], and the production of undetected gravitons at TeV energies [35]. Both would lead to an apparent attenuation of the detected shower at ground level and hence look like a reduction of flux at high energies.

The way to distinguish between astrophysical or exotic explanations for the knee is to study the composition of the cosmic rays. For most of the new physics motivated knee models, the knee position for different primaries with respect to the main (proton) knee scales with the cross section of the production processes, i.e. the mass number, while for an explanation in terms of diffusion or acceleration, one would expect a dependency on the charge number Z.

1.4.1 Poly-Gonato Parametrisation

The phenomenological “poly-gonato” model, introduced in [6], is an attempt to describe the spectrum by fitting a combination of spectra, one for each nucleus, to the measured all-particle spectrum. Thereto, the spectral indices below the knee are taken from available data of the single components, while for the position and index change at the knees different approaches were tried out. The three models for the energy dependence of the knee position are

- at a constant energy, i.e. independent of Z and A.
- proportional to Z (i.e. constant rigidity).
- proportional to A.

For the spectral change, two assumptions were probed, namely a fixed index γ_c for all spectra above their knees, and a constant index change $\Delta\gamma$ for all individual spectra. If one takes into account the χ^2/d.o.f. of the fits and the compatibility of the resulting energy dependence of the mean logarithmic mass in comparison to experimental results, the rigidity dependent ansatz in combination with a common $\Delta\gamma$ seems to be the most suitable solution. In this fit, the second knee corresponds to the knee of the heaviest nucleus frequently produced in the galaxy. The fact that the slope of the all-particle spectrum above the second knee turns out much steeper in the model than in measured data is explained by an additional extragalactic component of cosmic rays at ultra-high energies which is not covered by the model. Furthermore, an inconsistency of the predicted mean mass development and experimental shower maximum distributions was recognised.

Although in the the poly-gonato model all details and parameters are fitted phenomenologically and do not directly come from theoretical calculations, it can be regarded as a possible composition parametrisation. It was chosen as a mixed composition model in this thesis simply because, to the knowledge of the author, there is no other parameterisation that is carried out quantitatively to such an extent, which is needed if a simulated spectrum is produced.

As an alternative parametrisation, a two-component (proton, iron) fit performed on data from the KASCADE experiment is taken in addition (see sec. 6.1).

1.5 Extensive Air Showers (EAS)

The low fluxes of cosmic rays at and above PeV energies require huge effective detection areas to collect a statistically sufficient number of particles in a reasonable time span. Therefore, most experiments at energies above 100 TeV rely on the atmosphere as a converter volume. High energetic cosmic rays interact at altitudes of $10 - 40$ km with nuclei in the air and produce large cascades of particles that penetrate the atmosphere even to ground level if the energy is high enough. For example, a cosmic proton of 1 PeV energy typically leads to around 3 million secondary particles[1] on the surface of the South Pole Station (2835 m, or $\sim 680\,\mathrm{g/cm^2}$). These particle showers can be reconstructed by surface detector arrays, fluorescence or Cherenkov telescopes and give information about the primary cosmic particle. In general, the direction of the air shower resembles the one of the primary nucleus, the particle number scales with its energy, and the secondary particle composition and position of the shower maximum vary with its nuclear mass.

1.5.1 Phenomenology

In high-energetic hadronic interactions, such as collisions of cosmic PeV nuclei with atmospheric nuclei, a large variety of processes can occur, resulting in secondary hadrons. Besides new, partly excited, nuclei or fragments of such, mesons like pions and kaons are the dominantly produced particles. These secondary particles carry most of the kinetic energy and momentum

---

[1] About 1/6 of them are charged particles, the rest are photons.

of the primary and continue to interact with further air nuclei, so that a hadronic cascade is developed. If the mesons do not interact, they decay quickly. The most abundant decay channels are

$$\begin{aligned} \pi^+/K^+ &\longrightarrow \mu^+ + \nu \\ \pi^-/K^- &\longrightarrow \mu^- + \bar{\nu} \\ \pi^0 &\longrightarrow 2\gamma \\ K_S^0 &\longrightarrow 2\pi^0,\ \pi^+\pi^- \\ K_L^0 &\longrightarrow \pi^\pm e^\pm \nu_e,\ \pi^\pm \mu^\pm \nu_\mu, \ldots \end{aligned} \tag{1.7}$$

Hence charged mesons mainly yield muons, neutral pions yield gamma rays, and neutral Kaons can yield more pions or also leptons. Since the lifetime of charged mesons is comparably long ($2.6 \cdot 10^{-8}\,\mathrm{s}$ for $\pi^\pm$ and $1.24 \cdot 10^{-8}\,\mathrm{s}$ for $K^\pm$ [3]), some of them may interact before they decay and not lead to muon production. The ratio of decaying and interacting charged mesons depends on the air density and thus on the atmospheric conditions, and on the energy of the meson, which dilates its lifetime in the rest frame of the atmosphere. Since showers of nuclei with higher atomic mass evolve higher in the atmosphere and have a higher multiplicity (i.e. less energy per meson), these showers will have more decaying mesons and thus more muons than showers of low atomic masses.

Figure 1.6 shows the flow of energy in air showers. Muons may decay into electrons, but can otherwise be regarded a separate component of the air shower. Gammas, electrons and positrons build up an electromagnetic cascade that is a similar entity, so they are called the electromagnetic component of the shower. The third, hadronic, component continuously feeds the other two and is thus the energetic motor along the axis of shower development.

Concerning the total particle content of PeV showers at ground level, gamma rays are by far the most abundant particle type, followed by electrons and positrons, which are approximately a factor of 10 less frequent. Unlike electrons, the heavier muons are not produced so frequently by pair-production of gamma rays, and besides that need a much higher energy to initiate showers via bremsstrahlung, so their number is yet a factor of 10 less. Hadrons, like protons, neutrons, pions and kaons, can mainly be found at distances of some tens of meters to the shower axis, where they are roughly as abundant as muons. Neutrons are usually the last particles that can be measured occasionally, because they do not ionise the air molecules and can thus survive relatively long even with a small amount of energy.

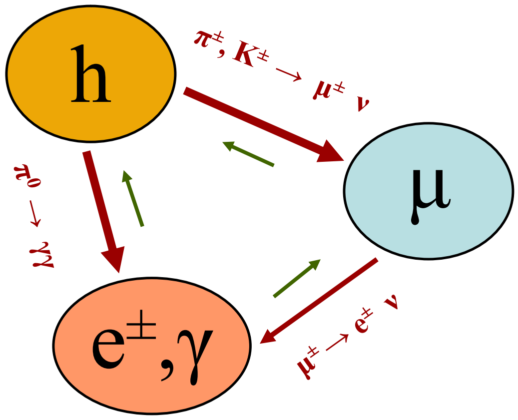

Figure 1.6: Energy flow between the hadronic, muonic and electromagnetic component of an air shower. The formulae shown are the dominant processes for the thick red arrows. The narrow green arrows indicate that in general there are minor reaction channels that also allow the inverse energy flow to a small extent.

Most showers in the PeV range are induced by hadrons because photons in this energy regime are most probably surpressed by the interaction with the extragalactic background light [31] and the cosmic microwave background. The main characteristic of hadronic showers, compared to purely electromagnetic ones, is that their longitudinal and lateral development fluctuates much more. This is because in the strong interaction, which dominates the evolution of the shower, the spread of transverse momenta of produced particles is much larger than in electromagnetic interactions.

In all air shower cascades, the secondary particle production probabilities are connected multiplicatively along the chain of reactions, therefore the particle densities observed at ground level are log-normally distributed. This leads to large variations that carefully have to be taken into account by likelihood based reconstruction algorithms.

The development of air showers and the resulting particle distributions on ground level are a difficult subject to describe in good precision by theory-based cascade equations. In fact, the available modellings can be used to fit measured or simulated distributions, but cannot excactly predict the development of a shower of a given primary energy. A common quantity to parametrise air shower development is the atmospheric depth X, or slant depth, defined as

$$X(z) = \int_{z}^{\infty} \rho(z) dz \tag{1.8}$$

with z being the altitude in meters, and ρ the air density. As an approximation, X can be derived from the pressure at a height z, $p(z)$, by $X(z) = p(z)/g$, where g is the standard gravity [36].

Using this, the longitudinal development of the electron number N_e of a shower can be described by the Gaisser-Hillas profile [37]

$$N_e(X) = N_{e,max} \left(\frac{X - X_1}{X_{\max} - X_1} \right)^{(X_{\max}-X_1)/\lambda} e^{(X_{\max}-X)/\lambda} \tag{1.9}$$

with $X_{\max}$ and $N_{e,\max}$ being the coordinates of the shower maximum, X_1 the depth of the first interaction and λ an additional parameter that is usually fixed to about $70\,\mathrm{g/cm^2}$ [38].

The electron density distribution at ground level in dependence of distance to the shower axis can be fitted by an NKG function [39]:

$$\rho(r) = \frac{N_e}{r_M^2} C \left(\frac{r}{r_M} \right)^{s_{\mathrm{NKG}}-2} \left(1 + \frac{r}{r_M} \right)^{s_{\mathrm{NKG}}-4.5} \tag{1.10}$$

Here, r_M is the Molière radius of the electrons, C is a normalisation constant, and s_{NKG} is called the shower *age*, which characterises the longitudinal development of a shower. It is defined as

$$s_{\mathrm{NKG}} = 3 \left(1 + \frac{2X_{\max}}{X} \right)^{-1} \tag{1.11}$$

with the atmospheric depth X and the depth of the shower maximum $X_{\max}$ [38]. With the development of a shower, the age develops from 0 to 3, being 1 at the shower maximum.

Figure 1.7 illustrates how the position of the detector, relative to the longitudinal shower maximum, changes with several shower and observation parameters. The signal of a shower with primary energy E_0, zenith angle θ_0, and mass A_0, measured at a radius R_{ref} under an atmosphere with total depth X_{atm} is taken as a reference. Varying these parameters changes the age a shower is observed in. For example, a shower that is detected in the shower maximum under inclination θ_0 will appear attenuated when observed under higher inclination. However, if the same comparison is done at a lower energy $E < E_0$, a signal enhancement might be observed instead, etc.

Because of these interdependencies, the above parametrisations do not easily lead to the kinetic properties or mass of the primary particle. Therefore, every ground-based air shower experiment needs shower simulation programs to correctly interpret measured events. This is described in sec. 1.5.3, after some experiments have been introduced that are currently investigating the knee regime of cosmic rays.

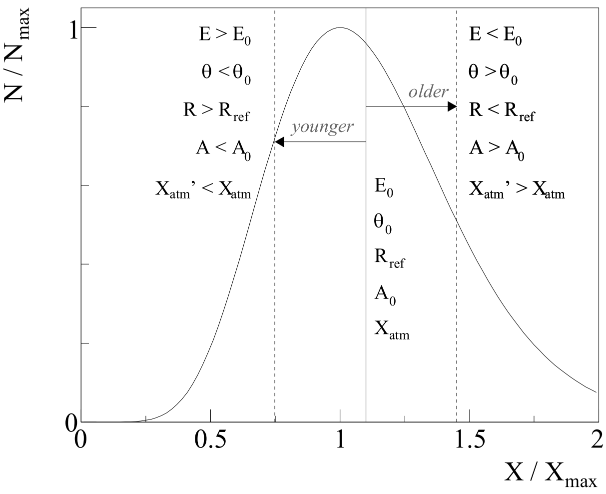

Figure 1.7: Dependencies of the relative detection level of a shower of energy E_0, zenith angle θ_0, and mass A_0, measured at a radius R_{ref} under an atmosphere with total depth X_{atm}. All parameters effectively shift the detector with respect to the shower maximum. The curve is a Gaisser-Hillas profile. It is only for illustration and may not apply for all radii R_{ref}.

1.5.2 Some Recent Experiments

Extensive air showers offer several ways to investigate cosmic radiation. Besides measuring the particle densities or energy deposits at ground level, the showers produce Cherenkov radiation in the atmosphere. Also, fluorescence states of the nitrogen in the air are excited, which can be used by fluorescence telescopes at energies above some EeV. Some experiments measure muons as a side effect, for example at accelerator facilities, and try to conclude on cosmic rays from that. In the following, three of the most advanced and dedicated experiments in the PeV regime are introduced, namely KASCADE-Grande, Tunka-25 and Tibet-III.

KASCADE-Grande

KASCADE-Grande [40] is a multi-component, ground-based air shower array near Karlsruhe, Germany at an altitude of about 115 m above sea level. Its main array covers an area of 0.5 km^2 and consists of 37 scintillation detectors with a dynamic range of 10^5 and an average grid size of 137 m (see fig. 1.8). In addition to that, the smaller KASCADE detector is in operation, which is located at the side of the array and consists of a smaller air shower array, muon detectors, a muon tracking detector, a hadron calorimeter and

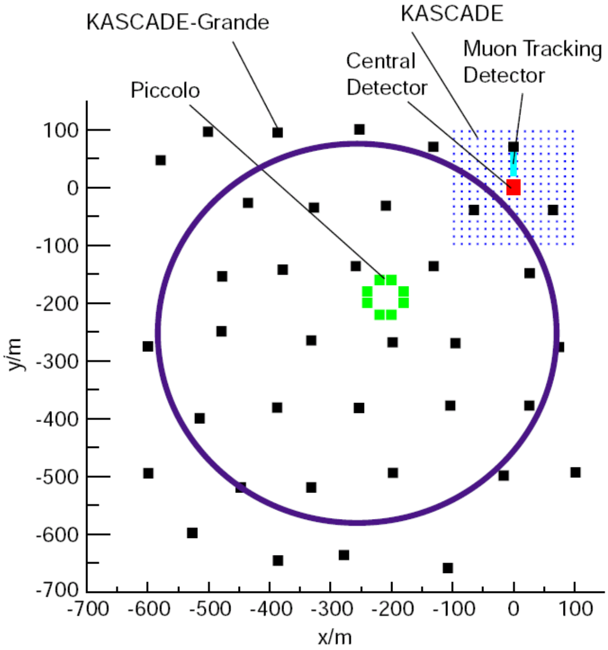

Figure 1.8: The detector components of KASCADE-Grande.

other minor components. Also, a small trigger array “Picolo” is located in the centre of the detector. With the main Grande detector, roughly the same energy range is covered as by IceTop.

The resolutions achieved with the detector are 13 m for the core location, 0.3 ° for arrival direction, and 15 % in the shower size. Besides many air-shower related studies, one of the most advanced studies of cosmic ray composition in the PeV regime was published [10] using KASCADE data and unfolding algorithms to disentangle energy and composition. The data indicate a higher knee energy for heavier nuclei, but also show a strong dependence on the interaction models involved in the simulations.

The main difference to IceTop is the low altitude, the scintillator technique and a different strategy of muon detection.

Tunka-25

Tunka-25 is a Cherenkov light array that measures the Cherenkov radiation produced by the shower particles in the air [41]. It consists of 25 detectors spread over 0.116 km^2 at 675 m above sea level, not far from Lake Baikal, Russia. In addition to these wide-angle integral detectors of Cherenkov light, four light pulse shape detectors are set up within the array.

The Cherenkov light measured follows a lateral distribution perpendicular to the shower plane that is quite different from the distributions measured by particle-based detectors. Still, although it varies close to the shower axis, a shower size estimator Q_{100} can be extracted at the distance of 100 m from that. The resolutions achieved in the reconstruction are 0.5 ° in direction, 7 m in core position, and 10 % in shower size.

A spectrum and mass composition was published in [42], indicating a composition that becomes heavier above the knee.

Presently, an extension Tunka-133 is being constructed to increase sensitivity and statistical quality at higher energies.

Tibet-III

Tibet-III [43] is a scintillator array that is installed at 4300 m altitude at Yangbajing, China. It comprises 789 detectors in total. The inner main part covers 0.0369 km^2 with 7.5 m lattice intervals. Therefore it is already sensitive above some TeV, where its other physical goal is to measure highly energetic gamma rays.

Due to its small grid size, its resolution above 100 TeV is already $< 0.2\,°$ in direction, 5 m in core and $5 - 10\,\%$ in shower size, depending on energy.

In [43], a similar analysis is presented as pursued in this thesis, namely the extraction of an all-particle energy spectrum without measuring the composition. Only a small dependence on interaction models in the simulation is found, so the composition is the main uncertainty (fig. 1.9).

1.5.3 Simulation of EAS with CORSIKA

CORSIKA [44] is a package to simulate extensive air showers particle by particle, starting from the primary cosmic ray and leading to particle type, energy, location, direction and time information for every particle that reaches ground level. All relevant environmental options such as detector altitude, atmospheric layering, magnetic field etc. can be adjusted according to the location of the experiment that a shower is simulated for.

Figure 1.10 gives an overview on the taskflow inside the CORSIKA code. The atmosphere is iterated through layers, and for each layer, interaction and decay probabilities are calculated. If a decay is issued, the resulting particles are added to the simulation chain. In case of an interaction, external program codes are used to determine the secondary particles and their energies. The electromagnetic interactions are treated by EGS4 [45], which simulates all revelant possible processes in high precision. The more problematic part is the simulation of hadronic processes, especially at energies that cannot be accessed by presently available particle accelerator

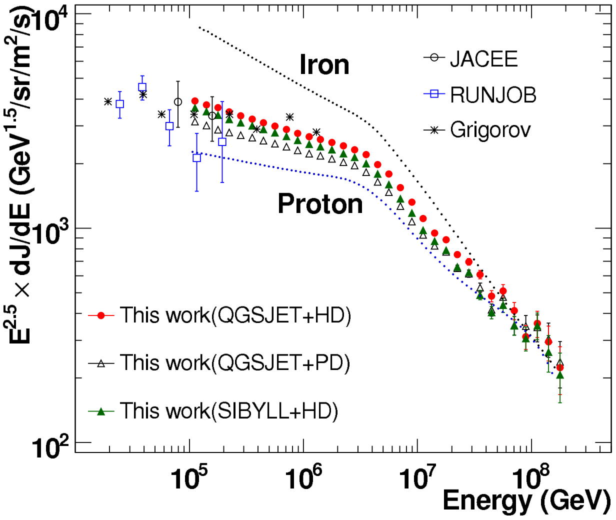

Figure 1.9: All-particle energy spectra measured by Tibet-III under different composition assumptions (only protons, HD, PD and only iron) and two different high energy interaction models (QGSJet and SIBYLL). The details are explained in [43]. The dependency on composition is the dominant uncertainty.

experiments. Here the uncertainties are very high, partly because the most important forward direction is very difficult to measure in experiment, and partly because extrapolations of cross-sections to very high energies are somewhat speculative, especially if new physics phenomena should occur.

Two of the most widely used high energy interaction models are SIBYLL2.1 [46] and QGSJET03.c [47] (or its newer version QGSJET-II). According to [48], where more details and references can be found, they both employ the pomeron formalism to describe non-perturbative ('soft') processes and also a comparable approach for semi-soft processes. The difference between the two mainly seems to lie in the treatment of non-linear parton effects. QGSJET applies a re-summation of pomeron-pomeron interaction diagrams, whereas the approach of SIBYLL is based on the parton saturation approach [49].

Except where indicated differently, the simulations done for this thesis use the hadronic interaction models SIBYLL2.1 for energies above 80 GeV and FLUKA [51] below that. The showers are propagated through CORSIKA atmosphere 14, which is a December atmosphere calculated for the South Pole with the MSIS-90 code [52]. This program can calculate the temperature and pressure profile across several atmospheric boundaries. However, according to the authors, it is not the model of preference for

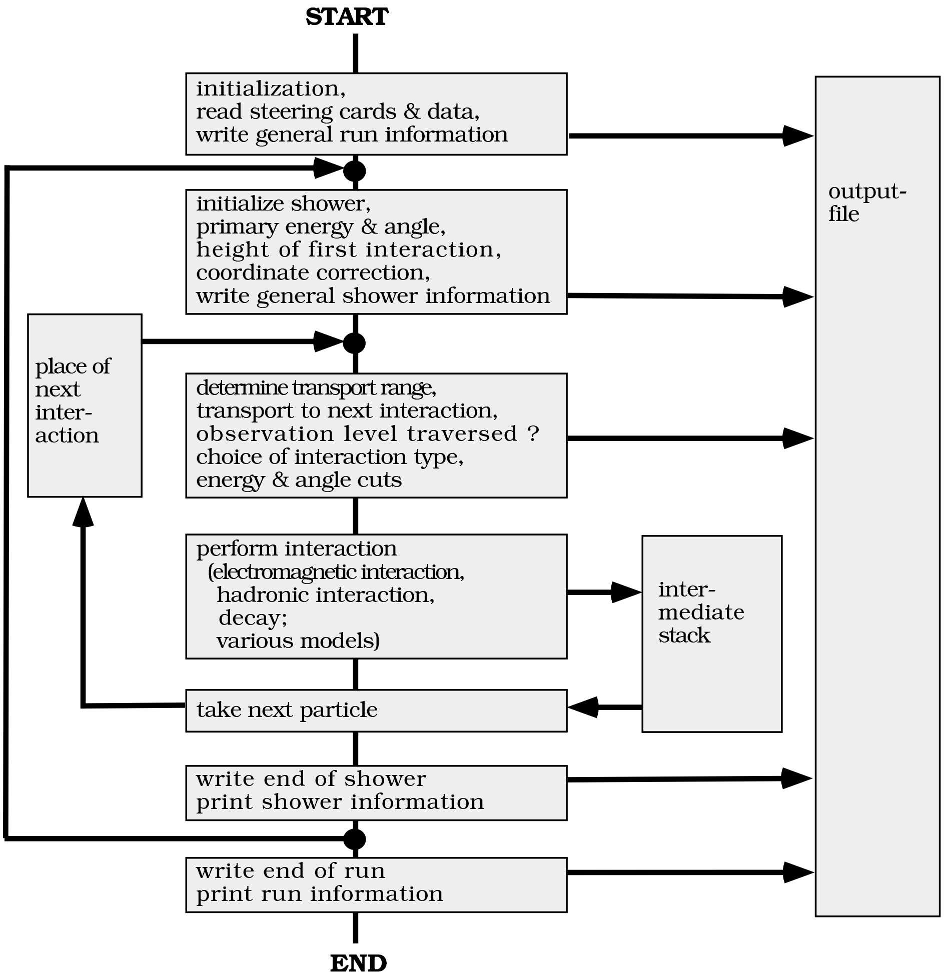

Figure 1.10: Task flow diagram of the CORSIKA shower simulation [50].

specialised tropospheric work, so it should be emphasised here that this is one of the issues that could be improved in future.

Other interaction models or different atmospheres were only tried out to estimate the systematics of the analysis (see sec. 8.2).

For whole-shower studies in which no individual tank areas are taken into account, the *thinning* options of the CORSIKA code could be used. Thinning means that the number of tracked particles is reduced while giving weights to the remaining particles in a way that the particle content and its energy sum are preserved. Technically this is achieved by assigning a certain survival probability to particles, depending on their energy, type or location, and let a random generator decide about the survival. If a particle does survive, the inverse of that probability is assigned as a weight for the particle. Hence the smaller the survival fraction, the bigger the weights. For the whole-shower study presented later, a thinning was chosen that causes a reduction of particles below $10^{-6} \cdot E_0$ and particles closer than 15 m to the shower axis, where E_0 is the primary energy of the shower.

Figure 1.11 shows mean secondary energy spectra at 100 m from the shower axis, and lateral distributions of the different particle types in vertical 1 PeV proton showers simulated with the above configuration. How the IceTop detector perceives these distributions will be discussed in chapter 4, after the descriptions of the IceCube Observatory and the IceTop data acquisition.

Gamma, 1 PeV

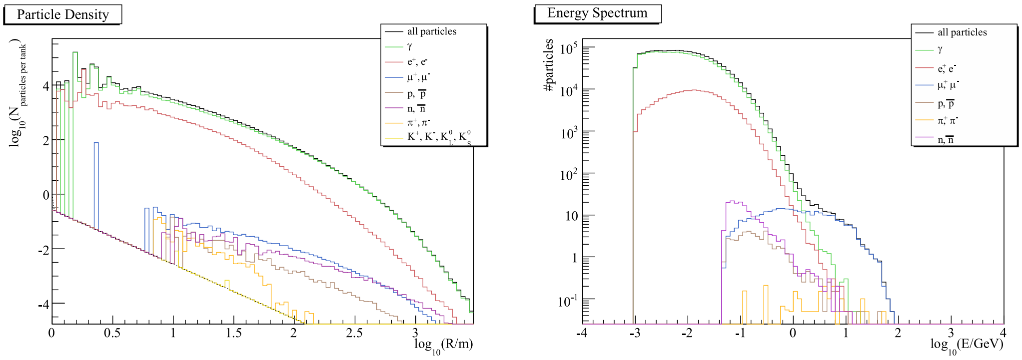

Proton, 1 PeV

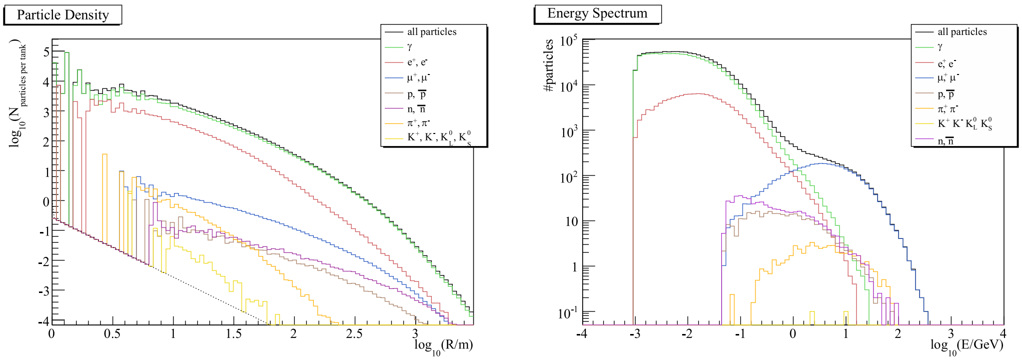

Iron, 1 PeV

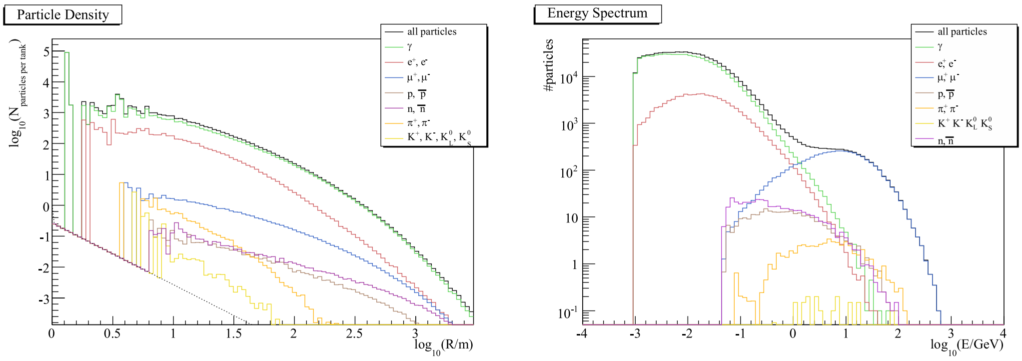

Figure 1.11: Mean characteristic distributions of secondary particles on the detection level of IceTop obtained by simulations of 1 PeV showers configured as described in the text.
LEFT: Lateral distribution of different particle type densities, normalised to the IceTop tank area. The dotted line in the lower left corner indicates the one particle level. The statistical distortions at low radii are caused by the thinning.
RIGHT: Energy spectra of different particle types at 100 m distance from the shower core at detection level. The low energy cut-offs are defined by the simulation and have no physical meaning.

Chapter 2

The IceCube Observatory

The deep ice of the southpolar icecap is a unique site for cosmic ray observations. The antarctic glacier is a big, solid, transparent and dark medium that is not available anywhere else in the world. It offers the possibility of three dimensional detection of highly energetic underground muon tracks or particle cascades. To do so, the Cherenkov light [3] is measured that is produced by charged particles traversing the ice at velocities above the reduced speed of light in the medium. This light can be used for the detection and analysis of very high energetic interactions of cosmic particles. A place where the antarctic ice sheet is accessible is the Amundsen-Scott South Pole Station.

2.1 IceCube

The IceCube Observatory [53] is a detection site that is primarily designed to detect muons produced by interactions of highly energetic cosmic muon neutrinos. Unlike the muons that come from particle air showers as described in sec. 1.5, these muons can come upward from muon neutrinos that penetrated the Earth beforehand. A muon neutrino above some hundred GeV can produce a muon that is minimally ionising and thus has an energy loss that is low enough for it to travel several hundred meters in the ice. As mentioned above, it will continuously produce Cherenkov light that can be measured in terms of time and amplitude. This information is used to reconstruct the direction and energy of that muon, which closely resembles the direction and energy of the neutrino.

The prototype detector AMANDA proved that in this fashion it is possible to detect atmospheric neutrinos that come from air showers on the northern hemisphere (e.g. [54]). The directions of the events could be reconstructed with a precision of about 2° [55], which is good enough to detect the location of astrophysical neutrino sources. These sources would generate a signal above the atmospheric background. With present data, no such source as yet could be established with statistical significance. One of the main goals of IceCube is to collect enough of these events to find an underlying steady or transient distribution of neutrinos from high energetic cosmic sources.

Another very promising detection channel of IceCube is that of electromagnetic cascades induced by electron and tau neutrinos, as described in [56]. In contrast to the long signal track that a muon produces in the detector, a cascade is approximately a point-like source of light and can be well distinguished from the former. One advantage of that channel is that the energy resolution in general is better than that of the muons because the cascades are more or less contained whereas the muons are not [57]. The disadvantage is that the directional reconstruction is extremely poor, so the cascade analysis is mainly seeking a diffuse excess of event rates.

2.1.1 Detector Setup

Figure 2.1 shows an illustration of the IceCube Observatory as it will be set up once its construction is completed. The deep detector volume, in the following refered to as "IceCube", will be a 1 km^3 grid of Digital Optical Modules (DOMs) deployed on 80 vertical strings at a depth between 1.45 and 2.45 km below the ice surface [58]. 22 of these strings were already in place in 2007. The mean distance between the strings is 125 m, which is much more than in the old AMANDA detector, where the equivalent quantity was 60 m. To be still sensitive to low-energy events, AMANDA was integrated in the IceCube DAQ and will be kept in operation. The whole setup is complemented by IceTop, which is a two-dimensional array of detector tanks on the ice surface that will be further described in section 2.2. Besides its own physical goals, IceTop can serve IceCube as a partial veto for background muons from air showers and as a calibration device.

2.1.2 The Digital Optical Module (DOM)

The Digital Optical Modules that IceCube and IceTop are equipped with are sophisticated light detection devices that deserve some more attention in this section since the results presented later are based on their capabilities.

A DOM is a glass sphere that contains a photomultiplier tube (PMT), a high voltage supply, readout electronics and a flasher board as main components (see fig. 2.2). A PMT is a high voltage device which converts photons

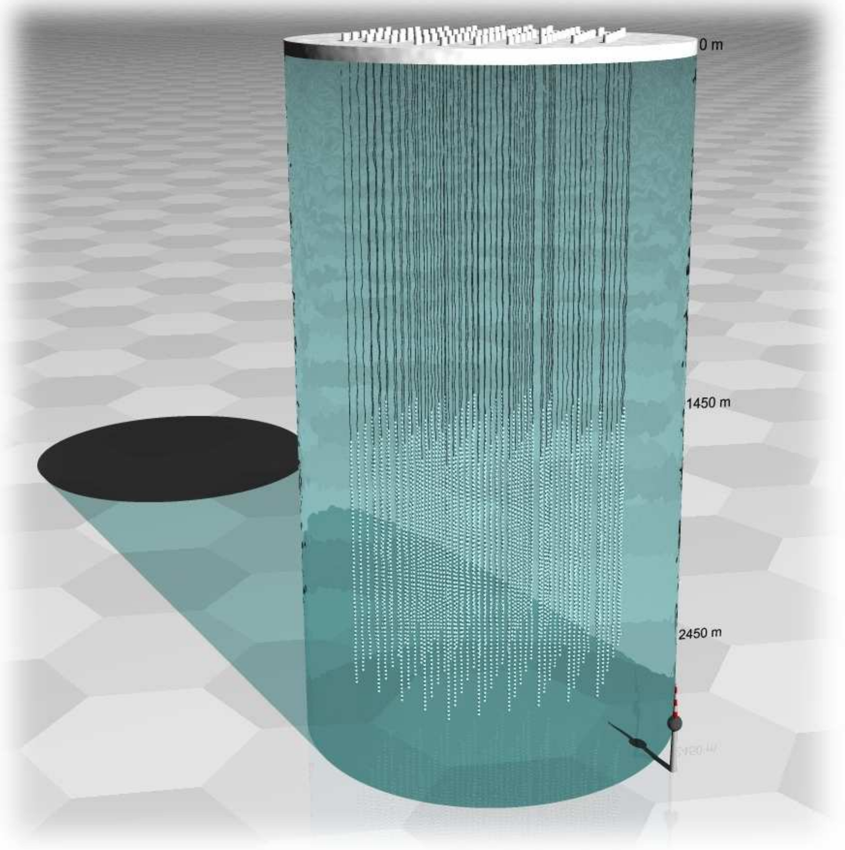

Figure 2.1: A sketch of the IceCube detector as it is planned once its construction is completed. Each displayed surface tank represents one IceTop station. (drawing by A. Lucke)

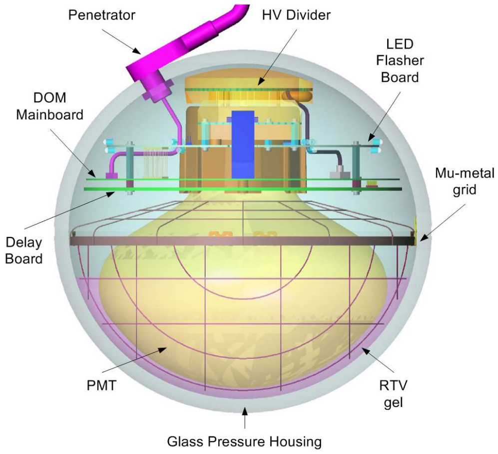

Figure 2.2: IceCube Digital Optical Module (DOM). The PMT fills most of its volume, shielded from Earth's magnetic field by a mu-metal cage. On top, readout electronics, a high voltage generator and an LED flasherboard are installed.

that hit its photocathode to a bunch of electrons. This charge, arriving at the anode located at the opposite side of the tube, can be measured and thus makes the PMT a single photon detector with nanosecond time resolution. Its efficiency at its most sensitive wavelength (mostly in the blue or violet optical) is around 20 % though, so it only allows for a fraction of all photons to be detected. The time structure of the arriving charge roughly follows the time structure of the photons arriving at the photocathode. However, since not every photon produces a charge and the charge per photon also varies, the distribution of charge over time in the end will be a smeared, statistically distorted convolution of the initial photon intensity distribution.

The time structure of the created charge, in the following refered to as waveform, is recorded and digitised by the DOM electronics. This makes it possible not only to analyse the integral charge of recorded signals, but also to trace their time development and the physics that causes it. In addition, the fact that the waveforms are digitised in situ means that there is no signal quality reduction when the data is submitted to the DAQ system via up to 4 km of copper cables.

Digitisation and Recovery of Waveforms

The amplitudes of recorded air shower and muon waveforms in and above the ice cover many orders of magnitude. This requires an elaborate digitisation system in order to avoid saturation or bad resolution. In the DOMs, this is overcome by the usage of three different electronic amplification stages. The analogue signal from the PMT is split into three branches that are amplified by 0.25, 2 and 16 respectively and stored into capacitors of an Analogue Transient Waveform Digitiser (ATWD). Each branch can be digitised by the ATWD, which offers 128 time bins with 10 bit amplitude resolution. The time bins are approximately 3.3 ns wide, so the achieved recording time is $\sim 420\,\text{ns}$. The three gains cover a dynamic range of about 10^5.

What comes along with this sophisticated PMT readout system is that it needs some care to retrieve calibrated information from the raw data. Each bin in each ATWD channel has its own calibration constants, and the waveforms of the ATWD channels may have different baselines. In addition to that, even more light pulses may be recorded by a second ATWD that substitutes the first one while it is in the digitisation process (described in detail in sec. 3.4). In 2006, most of the difficulties that occured in the calibration procedures were satisfactorily eliminated, so that in this thesis, it will not be discussed in further detail. More information on the issue can be found e.g. in [59, 60].

2.1.3 Physical Goals

The principal motivation of the search for cosmic high-energy neutrino sources comes from the fact that there exist many models and ideas on what the sources of highly energetic cosmic rays could be(see sec. 1.2). Some of these models are based on hadronic acceleration and thus predict neutrinos as a side-product of interactions of the hadrons in the surrounding of the source. Some sources, like for example GRBs, are expected to be transient, which can be proved by coincident observation with gamma ray observatories [61]. Detecting a neutrino signal, point-like or diffuse, could rule out some of these models and could particularly well distinguish hadronic from electromagnetic accelerators of cosmic rays.

AMANDA, the prototype detector of IceCube, did not so far find any neutrino signals that could not be explained by the background atmospheric neutrinos [55]. IceCube, in the interesting high energy regime, offers 30 times more area to muon neutrinos and a hundred times more volume to electron neutrino cascades than AMANDA did [58, 62, 56]. Therefore it is not unlikely that, if there is hadronic acceleration, IceCube might see it.

However, independent of that, the neutrino detection is not the only goal that IceCube pursues. The IceTop Surface array makes IceCube a very advanced, three dimensional detector for charged cosmic rays.

2.2 IceTop

IceTop is the 1 km^2 surface component of the IceCube Observatory [63]. On top of each IceCube string there are two cylindrical tanks filled with ice that form an IceTop *station*. Each tank is equipped with 2 DOMs (see sec. 2.1.2) that record the light produced by charged particles of extensive air showers that occur in the atmosphere above the detector (see sec. 1.5). Since the electromagnetic component of the showers is dominant on the surface, while deep in the ice only high-energetic muons persist, IceCube as a whole offers a view into the secondary composition of showers whose axes go through IceCube and IceTop. Besides an advanced direction reconstruction, this gives a handle on what the type of the primary nucleus is. Having a muon detection area as huge as 1 km^2, and in the same time being located at an altitude where PeV showers are in the maximum of their development (2835 m, or $\sim$ 680 g/cm^2), makes IceTop unique among all other air shower experiments.

2.2.1 Hardware

In 2007, 26 detector stations had been equipped with 2 tanks each and 2 DOMs per tank. Figure 2.3 shows the layout of the array. The stations on average are separated by 125 m while the mean tank distance within a station is 10 m. The station spacing defines the air shower detection threshold to be around 300 PeV when a trigger of 3 stations is required. The tank spacing also allows for the detection of smaller showers, which can be used as a veto condition in the neutrino detection of IceCube.

Each IceTop tank is installed just below the ice surface to avoid snow accumulation (see fig. 2.3, left). It contains a cylindric ice block with a radius of 93 cm and a height of 90 cm. The material of the outside walls and the bottom is light-proof and has a reflective coating on the inside. In the first season, a Tyvek material with a reflectivity of about 90 % in the UV was installed. In all following seasons, a layer of zirkonium ($70 - 80$ %) was used instead, which led to a better compromise between enhancing the signal, while not smearing it out too much. The top of the ice block is covered with $20 - 30$ cm of perlite powder, which also reflects the light, but as a drawback causes big uncertainties in the detector simulation since its contact to the ice is quite unpredictable. The perlite also prevents light from entering the ice volume from above.

Two DOMs per tank are mounted on top of the ice, with the photocathode part of the glass sphere looking downwards and being in direct contact with the ice (fig. 2.4). This has the advantage that in principle there should

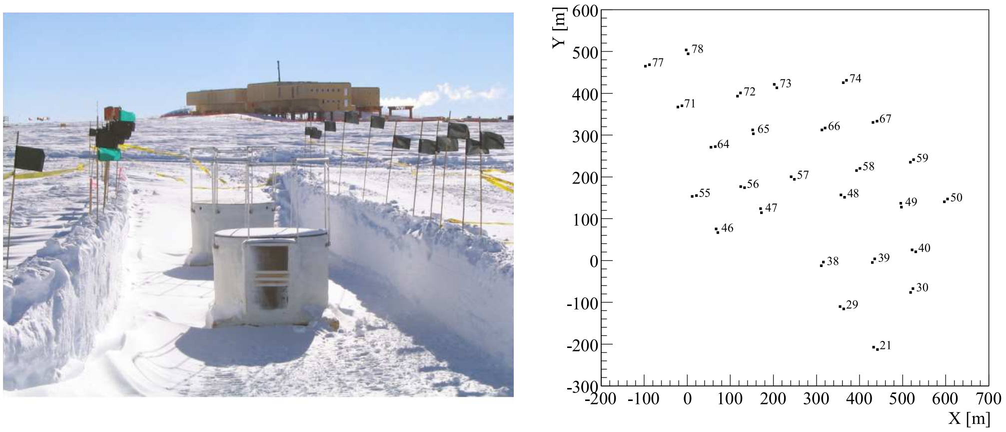

Figure 2.3: Left: Photo of an IceTop station before the trenches are filled with snow. Right: Schematic 2007 configuration of the IceTop detector tanks. The 52 tanks are roughly a third of the complete detector.

be an ice-glass contact with no air gap that leads to further reflections. In reality, however, there are indications from muon calibrations (sec. 3.3) and observations throughout the freezing process that this ice-glass interface is not always smooth and, probably depending on temperature, does have air bubbles and gaps from time to time [60].

It is important to mention here that all uncertainties connected to the ice and perlite behaviour over the season and during freezing are not necessarily of severe impact to the air shower measurement presented later. As will be shown in sec. 3.3, the tanks can be calibrated with muons, which technically makes this thesis independent of a correct and detailed simulation of the tanks. So the flaws mentioned here are only meant to be a pointer for future studies based on PMT waveforms, which actually will need a detailed detector simulation.

The two DOMs inside a tank can be run with equal gain for redundancy or with different gain to enlarge the dynamic range of the tanks. In 2007, one of the DOMs was operated at $5 \cdot 10^6$ (high gain, HG) and the other at $5 \cdot 10^5$ (low gain, LG), leading to effective charge thresholds of about 20 and 200 photo-electron equivalent respectively. This enlarges the dynamic range approximately by a factor of 10.

2.2.2 Physical Goals

Air shower measurements are connected to and dependent on several physical disciplines, and therefore can also provide relevant information about

Figure 2.4: Photo of the inside of an IceTop tank. The glass spheres of the DOMs are mounted in a way that the photocathode of the PMTs are below the ice surface.

them. Astrophysics is the main motivating field for IceTop, but also solar and particle physics can profit from it.

Chemical Composition and Energy Spectra

The main question that IceTop is expected to clarify is how the chemical composition of cosmic rays evolves in the regime between the knee and the ankle, i.e. from some hundreds of TeV to EeV energies. As described above, IceCube, as a two-part air shower detector, offers excellent conditions to do that. The ratio of electromagnetic to muonic shower contents is a handle on the primary type for two reasons. On the one hand, in collisions of cosmic heavy nuclei with atmospheric nuclei the pion multiplicity is higher than in proton collisions [64]. Although neutral and charged pions are produced in equal ratios, this enhances the muon production in the early stage of the shower because the thinner atmosphere at high altitudes enlarges the probability of charged pions to decay to muons rather than to collide with other nuclei. In addition to that effect, in air shower evolution, a shower of a nucleus of mass number A and energy E_0 can be approximated as a superposition of A proton showers of energy E_0/A because the multiplicity of the first interaction is roughly proportional to A. This leads to an equally big, but much shorter cascade, so that compared to a proton shower, a heavy nucleon shower will on average be at a later ("older") stage of development when it reaches ground level. Since the ratio of electromagnetic to muonic component (e/μ) is also changing with the age of a shower, this leads to an extra difference between showers from different primaries (see sec. 1.5). Depending on where the detector is located, relative to the shower maximum, the total signal, and also e/μ, may appear increased or attenuated for heavy showers (see also fig. 1.7).

How to analyse this has been demonstrated with the SPASE-II air shower array that was installed above AMANDA until 2006 [65]. There, the shower size at the surface was parametrised by S_{30}, the signal intensity of a shower at 30 m perpendicular distance to the shower axis. The muon density in the ice was estimated by the light intensity K_{50} at 50 m distance from the reconstructed track of the muon bundle. Figure 2.5 shows the correlations between S_{30} and K_{50} in simulations of proton and iron primaries of different energies in comparison to experimental data. Most showers end up close to a diagonal line which can be regarded as the energy axis. Iron showers on average are shifted perpendicular to that, so that roughly speaking a simple coordinate transformation can give E_0 and the atomic mass number A.

In reality, however, it is much more complicated to disentangle energy and mass number from the smeared-out, overlapping shower data. As can also be seen in the latest data from the KASCADE-Grande experiment [40, 10], even the most advanced composition analyses are still quite unclear and strongly depend on the interaction models that are put into the shower simulations used in the analysis. A discussion of composition analysis strategies with IceTop can be found in [66].

All-Particle Energy Spectrum

An outcome of the composition evolution analysis is that the single component energy spectra can be added up to an all-particle energy spectrum. This can also be done with IceTop once the composition spectra are analysed. However, most experiments try to define a compositon-independent shower size variable to derive an all-particle energy spectrum before doing a composition analysis. Alternatively, an all-particle spectrum can also be derived if a composition assumption is made beforehand. This will be a goal in this thesis.

The motivations to measure an all-particle energy spectrum are the following:

1. The systematic differences between the existing spectra are still large. Any new measurement carried out under different environmental conditions (South Pole), with different detectors (ice Cherenkov tanks) or analysis techniques can reduce the overall uncertainty. This is needed especially in the regime between the knee and ankle of the spectrum, where up to now only few measurements exist.

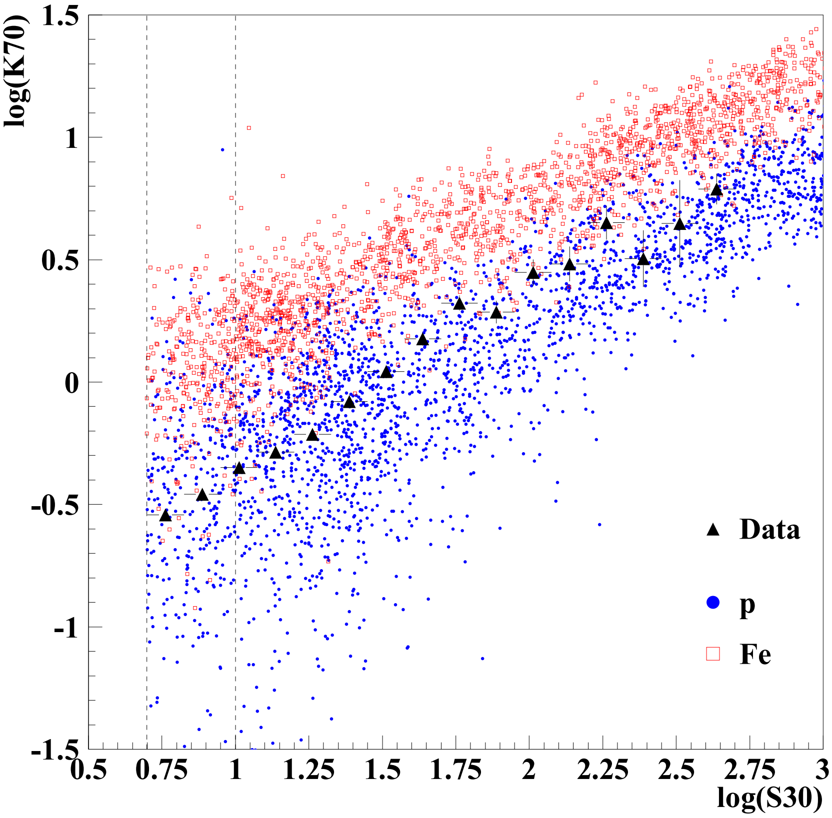

Figure 2.5: Composition determination in SPASE/AMANDA. K_{50} is a quantity related to the muon content of a shower, S_{30} mainly scales with its electromagnetic part.

2. The universality of the general features of the spectra, like existence of the knees, their positions, indices, can be verified or falsified.
3. The ability to measure a reasonable energy spectrum with the above features is a general verification of the detector, its data acquisition and reconstruction algorithms. This is a particularly important point in the early phase that IceTop is still in.

Horizontal Showers

Air showers with an incident zenith angle above 70 ° are usually called horizontal showers. Since the depth of the traversed atmosphere is very large for these showers, their physics is somewhat different than that of vertical showers. There are two possible classes of horizontal showers:

- Showers of hadronic origin that are very old, i.e. they practically consist only of muons because the electromagnetic and hadronic components have already vanished.
- Neutrino initiated showers at any stage of their development. The column depth of traversed atmosphere, or a slice of the Earth (for showers above 90 °), might offer a sufficient amount of target material for the neutrinos to interact.

If it is possible to distinguish the two, one could detect neutrinos with IceTop. However, the Earth's magnetic field, which at the South Pole is perpendicular to horizonal shower axes, tears apart the positive and negative particles in the showers. This leads to a detector signature that will most probably need separate custom reconstruction algorithms.

Solar Physics

The untriggered IceTop discriminator rates are related to the rate of low energy cosmic rays in the upper atmosphere. The flux of these particles is affected by disturbances in the solar wind and hence solar activity. Recently, an effort was presented to include the IceTop tanks into a global solar neutron monitor that helps understanding solar particle fluxes and transient phenomena in the flux of galactic cosmic rays [67].

Particle Physics

Another field of research could be the study of muon multiplicities, in particular those with high transverse momentum. These are produced predominantly in the initial cosmic ray interaction from semileptonic decays of heavy quarks, and from decays of high-p_t pions and kaons produced in jet fragmentation. As presented in [68], these could probably be measured separately from the main air shower muon bundle in IceCube. Unlike the low-p_t muons, whose number and energies can only be predicted by phenomenological models, high-p_t muon production can be approached with actual calculations in perturbative quantum chromodynamics. So on the one hand, this might lead to another composition-sensitive detection channel, and on the other hand it can be used to inspect the hadronic interactions.

Chapter 3

Calibration and Data Acquisition

This chapter will introduce technical details of the production, acquisition and low level treatment of IceTop data. Although it might not be necessary for the general reader of this thesis to follow all of them, it is the basis of what will follow, and the progress that has been achieved in the past three years is worth being documented here.

3.1 Cherenkov Light and Energy Deposit

As mentioned in chapter 2.2, the source of the light measured in an IceTop tank are relativistic charged particles in the ice bulk of the tank. Travelling above the speed of light of the ice, they produce Cherenkov light [3]. The amount of produced photons per track length is practically independent of the particle energy if it is highly relativistic. The energy distribution of the emitted photons is flat if a constant refraction index is assumed. Since the energy of photons scales with λ^{-1}, the distribution of wavelengths thus goes with $1/\lambda^2$ [3]. This leads to a UV dominated light emission in the tanks.

The energy deposit per track length is mainly caused by ionisation, and is described by the Bethe-Bloch formula [3]. The bulk of charged particles is at a minimum ionising energy (some GeV for muons, some MeV for electrons), where the energy deposition shows only little dependence on the particle energy. That means that, like the Cherenkov yield, the energy loss will be proportional to the track length of a particle. Or, adding the two statements, the Cherenkov yield will be proportional to the energy deposit of a particle.

The time structure of the measured photons is a convolution of the shower intrinsic particle distribution and tank intrinsic fluctuations of the photon propagation. An idea of how to use this time evolution, or waveform, is that electromagnetic particles may be distinguishable from muons. The high number of low energetic electromagnetic particles produces a signal that is assumably more spread out and fragmented than that of a muon, which produces its light homogeneously along a single track. Unfortunately, at distances within some hundred meters from the shower axis, the overall particle number is so large that the pulses of electromagnetic origin sum up to a big pulse that is actually not distinguishable from a hadronic or muonic pulse. Still, at higher radii, where the signal expectation is well below 1 VEM, a single muon might be identifiable among the electromagnetic signals.

So at present, only the integrals and starting times of the recorded waveforms are used in the reconstruction and analysis of air shower events. How these quantities are extracted will be outlined in the following.

3.2 Pulse Processing

The light curves are recorded by the DOMs as described in section 2.1.2 and lead to digital, calibrated waveforms of approximately 420 ns length. As a convention, the amplitude of each bin is given as a voltage. To get quantities that are independent of the particular DOM settings and characteristics, four steps of data processing are performed on each waveform. (In brackets are the names of the software modules which take care of the action):

1. **Droop Correction** (`DOMcalibrator`)
   The coupling of the PMT to the DOM mainboard involves an inductance which, for the first set of produced DOMs, causes a signal droop at low temperatures, leading also to voltage undershoots. This is only a problem for DOMs deployed in the first season, i.e. 4 IceTop stations. Although there is a lot of effort being put into creating algorithms that correct for this droop, the methods available at the time of this thesis were regarded not mature enough to be used in this analysis, so the following will neither use droop correction in data nor in simulation. There is no droop simulated in the simulation either. This is no real problem since the muon calibrations practically correct for the lost charge.

2. **Baseline determination and subtraction** (`topwaveprocessor`)
   Several methods were tested to safely determine the baseline of pulses. Pulseshapes and the position of a main pulse in a waveform sample

can vary, especially if a noise pulse triggered the readout shortly before the main pulse. The method decided to be used is taking the average of the last 40 valid bins of the waveform as a baseline. This is not particularly sophisticated, but delivers very stable results that are easy to deal with in simulation.

3. **Charge integration** (`topwaveprocessor`)
   After the baseline is subtracted, the voltages of all bins are summed up and multiplied with the bin size, leading to the integral charge of the waveform in terms of Coulombs. To become independent of individual PMT characteristics and gain settings, this value is divided by the peak value of the single photo electron (PE) charge distribution of that DOM at the given gain setting. This yields a charge in units of PE, which is proportional to the number of measured photons.

4. **Leading edge time extraction** (`topwaveprocessor`)
   A timestamp is extracted by a leading edge algorithm that determines the steepest step before the highest peak of each waveform. The difference between the two bins of that step is extrapolated linearly down to the baseline. The intersect of the two is taken as the timestamp.

These algorithms are very stable, so practically all waveforms can be analysed like this. In case a charge turns out negative or the raw ATWD information is not be available in a non-saturated channel, the waveform is not discarded but marked as being invalid, so that the following algorithms can distinguish between tanks without trigger and tanks with valid pulse.

3.3 Tank Calibration and Pulse Selection

Before charge values of different tanks are really comparable to each other, one has to perform yet another calibration. As shown in [60], each tank, and even each mounted DOM, has its individual light yield, depending on whether and where there are cracks or bubbles in the ice, which material is used for the tank inside walls and how the surface of the ice has become during the freezing process. This can be overcome by the so-called muon calibration runs, as described e.g. in [69] and widely applied also by other experiments. Running without any trigger, the tanks record any charged particle that hits it, which, above some tens of PE, are predominantly muons. These muons mostly are generated in showers with primary energies of some tens of GeV in the upper atmosphere. Since they normally pass the tanks without generating big cascades or decaying, the light yield

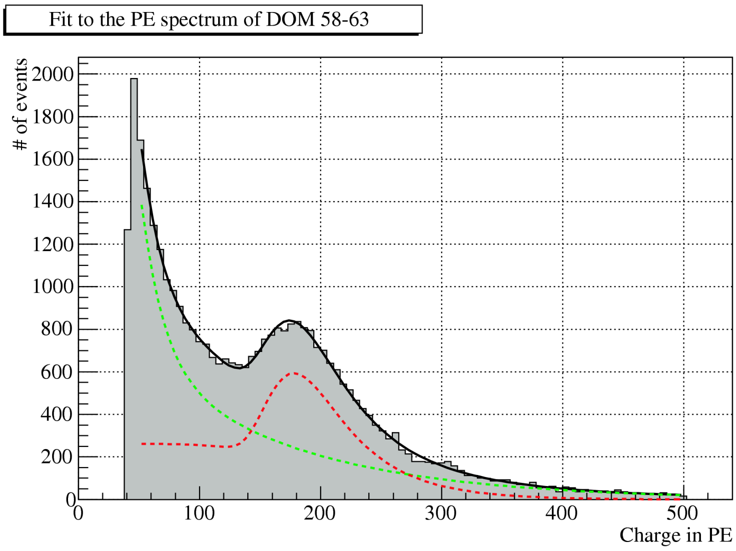

Figure 3.1: Typical muon calibration spectrum as shown in [60]. The black line is a fit function consisting of a muonic part (red) and an electromagnetic part (green).

of these muons simply follows the distribution of their track length, which has a narrow maximum at around one tank height. This causes an accordant feature in the signal charge distribution usually refered to as the *muon peak*. The position of that in terms of PEs only depends on the light yield of the DOM-tank system [70] (see fig. 3.1). The underlying background of electromagnetic background, and the asymmetric shape of the muonic pulse distribution, bias the maximum of the distribution by several percent. Presently, a factor of 0.95 is therefore applied to the found maximum to get the true signal that can typically be expected from a vertical muon.

Dividing the measured (PE-)charge of a certain pulse by that value[1] leads to a quantity that is comparable among tanks. This will from now on be refered to as “signal”, “tank signal” or “charge”, expressed in units of Vertical Equivalent Muons (VEM) and abbreviated with the letter S.

As a final step, the treatment of occasional information redundancy between the two DOMs in a tank has to be organised. The signals of two tanks at a station can be regarded independent to a certain degree, but the signals of two DOMs in a tank are highly correlated because the light they measure is produced by the same particles. Besides that, if two pulses are available in the same tank, one of them will be from the high gain (HG)

---

[1] This happens along with the following pulse selection in a software module called `topeventbuilder`.

DOM and the other one from the low gain (LG) DOM, so one of them will be preferable in data quality. The present treatment is that for each tank there is an individual crossover value of about 30 VEM below which a HG pulse is assumed to have little or no saturation and is chosen as the tank signal, and above which the LG pulse is chosen if available. HG pulses above the crossover value, but without LG partner should not occur, but if they do, they are marked as invalid and are not used for the reconstruction.

After this VEM calibration and pulse selection, each event consists of a number of pulses, one per tank, whereby each pulse has a time, a charge in VEM, and a position in the array. The reconstruction of air showers described later uses only this information.

3.4 Trigger Settings and Event Rate

The amount of recorded events and thus the data rate of the shower array is adjusted by the gain and voltage discriminator settings of the HG DOMs on the one side, and global trigger settings on the other side. The gain and threshold of the single module affect the sensitivity and noise rate of a single DOM, the global trigger system defines which signal coincidences are regarded as potential air shower signals.

An overview on the trigger and data acquisition is given in fig. 3.2. In 2007, the voltage discriminators of the HG DOMs were set up in a way that pulses are recorded with an effective threshold of about 20 PE. If an incoming PMT signal crosses the discriminator level, the capacitors of the first ATWD get filled with the incoming signal and the ATWD starts digitising it. The first level of trigger condition is fulfilled when both HG DOMs of a station have a discriminator launch within ± 125 ns. This is called a *local coincidence* (LC) and confirms the readout process of the ATWD, which keeps them from doing anything else for at least $100\,\mu$s. If no LC occurs, the readout is aborted and the ATWD is immediately ready for new launches.

For the case that a second signal triggers the DOM while the first ATWD is busy with digitisation, there is a second ATWD in the DOM to reduce the deadtime. Thanks to this, and given the typical event rate of some Hz, IceTop has no measurable deadtime.

The LC wires of the LG DOMs are connected to the HG DOM of the neighbour tank, therefore they are only read out if a HG local coincidence has already been established.

The digitised data is sent to the IceCube DAQ facility, where the global trigger conditions are evaluated. If there is an additional trigger in IceCube, or a simple majority trigger (SMT) given in IceTop, the data is stored. The SMT is the relevant trigger for the data used in this analysis and is fulfilled when 6 DOMs or more report a trigger within a time span of $5\,\mu$s. In this case, all DOMs within $\pm 9\,\mu$s (that have fullfilled an LC as well) are stored together as an event. This also includes coincident IceCube DOMs. The minimum requirement of 6 DOMs roughly corresponds to 3 stations, because in most cases only the HG DOM of a tank is triggered, yielding one signal per tank, i.e. two per station.

Physically, most station triggers are unaccompanied and caused by small air showers of some tens of TeV [71] that are below the reconstruction threshold. They are only stored in case of an additional trigger in IceCube and can be used for vetoing and calibration purposes in the neutrino analysis. The SMT catches air showers above $\sim 300\,$TeV [72] that are for instance studied in this thesis. Some more details about the trigger mechanism are given in fig. 3.2.

The event rate of the SMT triggered events in 2007 was around 15 Hz. Due to the limitation of satellite transmitted data, on which the following analysis depends, the rate of actually available shower records is downscaled randomly by a factor of 5. Only for events with ≥ 16 triggered DOMs ("SMT_Large"), this *prescale factor* is 1 to enhance the data sample at high energies. Most of the showers in the regime of full reconstruction efficiency fullfill this condition anyway, so the SMT_Large data deliver the bulk of the finally analysed events.

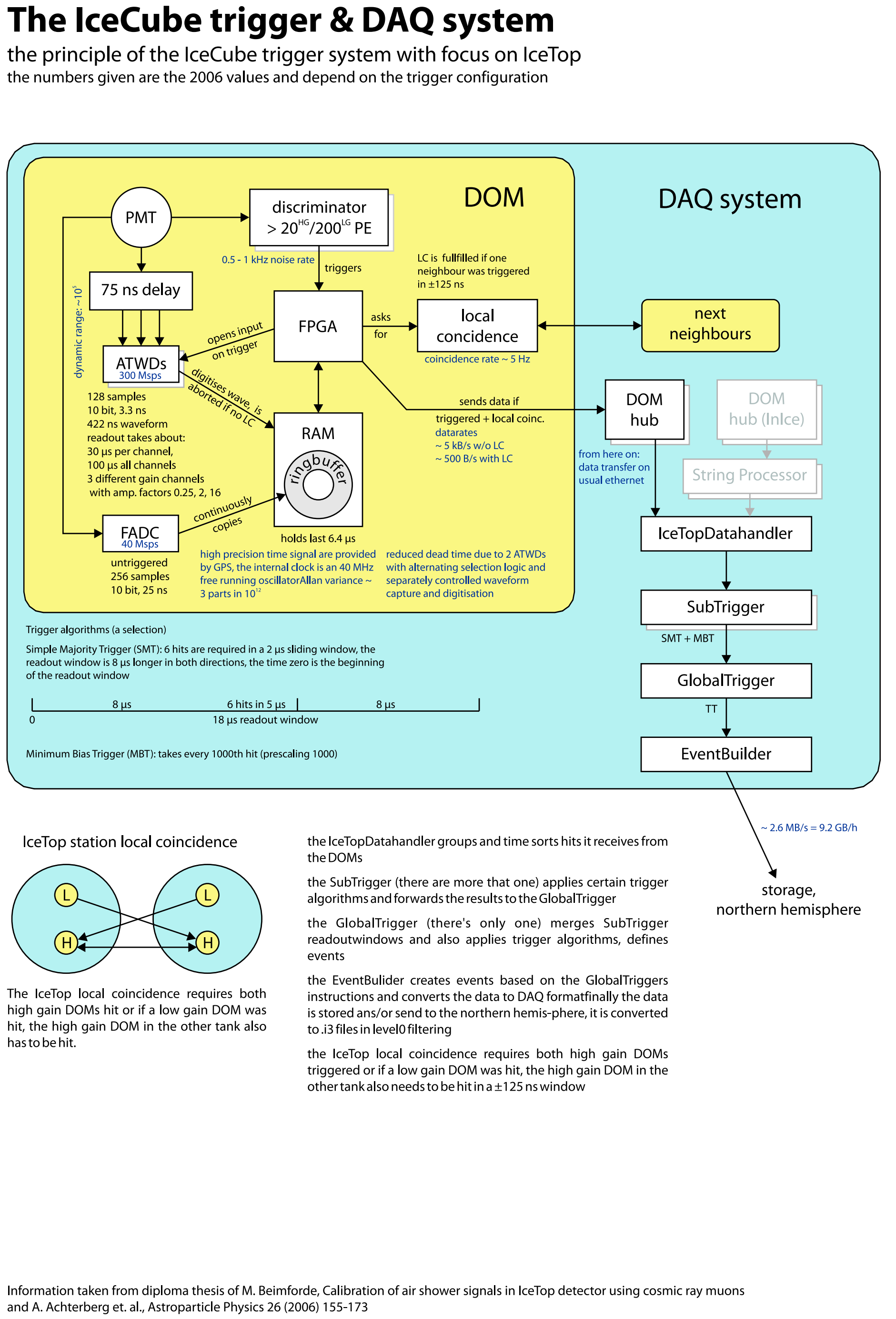

The IceCube trigger & DAQ system

the principle of the IceCube trigger system with focus on IceTop

the numbers given are the 2006 values and depend on the trigger configuration

high precision time signal are provided by GPS, the internal clock is an 40 MHz free running oscillatorAllan variance ~ 3 parts in 10^{12}

reduced dead time due to 2 ATWDs with alternating selection logic and separately controlled waveform capture and digitisation

Trigger algorithms (a selection)

Simple Majority Trigger (SMT): 6 hits are required in a 2 µs sliding window, the readout window is 8 µs longer in both directions, the time zero is the beginning of the readout window

Minimum Bias Trigger (MBT): takes every 1000th hit (prescaling 1000)

The IceTop local coincidence requires both high gain DOMs hit or if a low gain DOM was hit, the high gain DOM in the other tank also has to be hit.

the IceTopDatahandler groups and time sorts hits it receives from the DOMs

the SubTrigger (there are more that one) applies certain trigger algorithms and forwards the results to the GlobalTrigger

the GlobalTrigger (there's only one) merges SubTrigger readoutwindows and also applies trigger algorithms, defines events

the EventBulider creates events based on the GlobalTriggers instructions and converts the data to DAQ formatfinally the data is stored ans/or send to the northern hemis-phere, it is converted to .i3 files in level0 filtering

the IceTop local coincidence requires both high gain DOMs triggered or if a low gain DOM was hit, the high gain DOM in the other tank also needs to be hit in a ±125 ns window

Information taken from diploma thesis of M. Beimforde, Calibration of air shower signals in IceTop detector using cosmic ray muons and A. Achterberg et. al., Astroparticle Physics 26 (2006) 155-173

Figure 3.2: Schematic illustration of the IceTop trigger and DAQ system (figure by A. Lucke).

Chapter 4

Tank Response and its Fluctuations

Before going into details of reconstructions and analysis of air showers, some prerequisite studies will be presented here that the analyses are based on. They include a detector simulation of different particle types penetrating through the IceTop tanks and a parametrisation of these. Furthermore, a summary will be given about studies done on the fluctuations of air shower tank signals that are particularly important for the likelihood functions defined in the following chapter.

4.1 Tank Response Simulations

In addition to the simulation package provided by the official IceCube software framework IceTray, there is a Geant4 [73] based detector simulation project called `tanktop`. Both of them have advantages and disadvantages, but together they can deliver a good understanding of the actual detector.

4.1.1 `tanktop` vs. IceTray Simulation

`tanktop` is built for detailed simulation of particle interactions and tracks inside the tanks. Also, the produced Cherenkov photons are traced one by one and reflection and absorption processes are simulated. Its time consumption limits the application of `tanktop` to dedicated purposes only. In fact, simulating the whole array has for instance already become quite inefficient with the 16 station configuration of 2006.

In the IceTray simulation package, the processes in the tank are simplified and parametrised. In this manner, it is possible to simulate the whole array that is growing every year. Furthermore it has the advantage that it can use all interfaces and data formats built by the many people working on the neutrino analyses of IceCube. That means that actual calibration, detector status and geometry information are always available, and the simulation of the PMT, readout electronics and data acquisition system is much more realistic than the one of `tanktop`. Also, the reconstruction algorithms that are applied to real data can directly be used in the IceTray simulation, which helps avoiding inconsistencies.

One of the main applications of the `tanktop` package in connection with the results of this thesis is the simulation of single particle responses. Particles with vertical incidence were generated in a broad range of energies and randomly distributed over the tank surface. Above the tank, 30 cm of snow were considered. Besides pulse widths and other shape-specific parameters, the total charges S of the gained PMT pulses were extracted. Once the energy dependent response expectation $S_p(E)$ of a particle type p is known, general studies can be made, e.g. with simulated air showers from the CORSIKA code (see sec. 1.5.3).

Since the real response functions can be expected not to show any fine structures, the simulated data points were fitted in sections with functions of type $A + B \cdot C^D$ to smooth out statistical fluctuations and make the results applicable more flexibly (see also [74]). The functions found can be subdivided into three characteristic classes of muonic, electromagnetic or hadronic signatures.

4.1.2 Muons

Muons are the easiest particles to describe, because in most of the cases they do not decay or produce subshowers. That means that for muons above $\sim 300\,\mathrm{MeV}$, the Cherenkov yield will only depend on the track length of the muon in the tank. Below that, the amount of light decreases linearly, approaching zero at low energies. This is shown in figure 4.1(a).

4.1.3 Electromagnetic Particles

Electrons have a much lower radiation threshold than muons so they will not pass through the tank without producing bremsstrahlung photons. The same is true for gamma rays, which produce electron-positron pairs. The column depth of the ice in the tank is $X = \rho h = 82.5\,\mathrm{g/cm^2}$, which is equivalent to about 2.3 radiation lengths [3]. Thus a cascade will evolve if the incident particle has sufficient energy. In this way, photons, being the

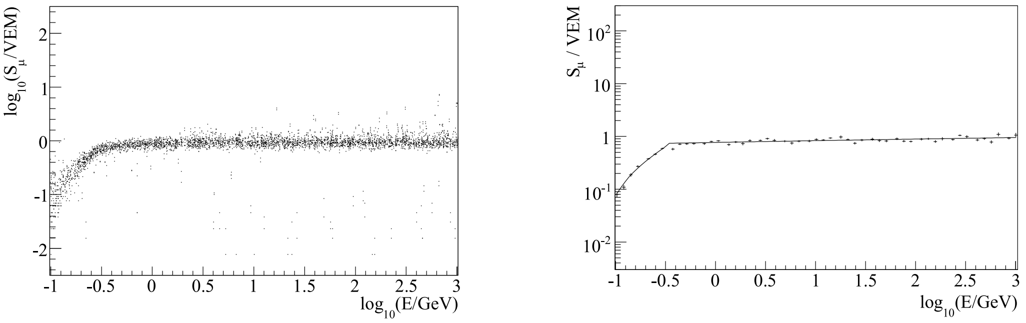
(a) Muons

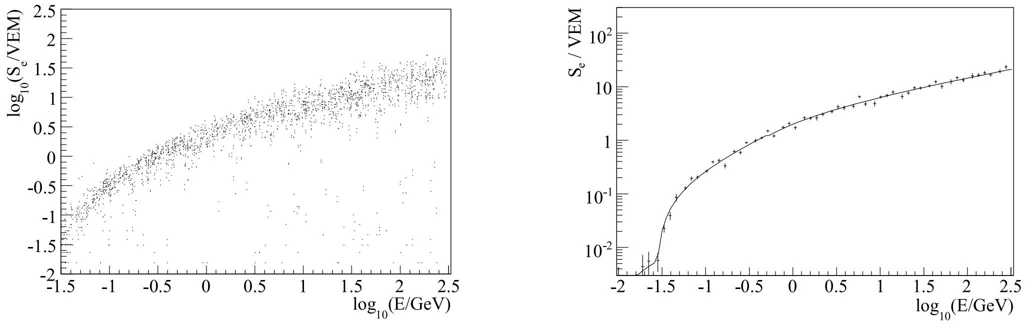
(b) Electrons

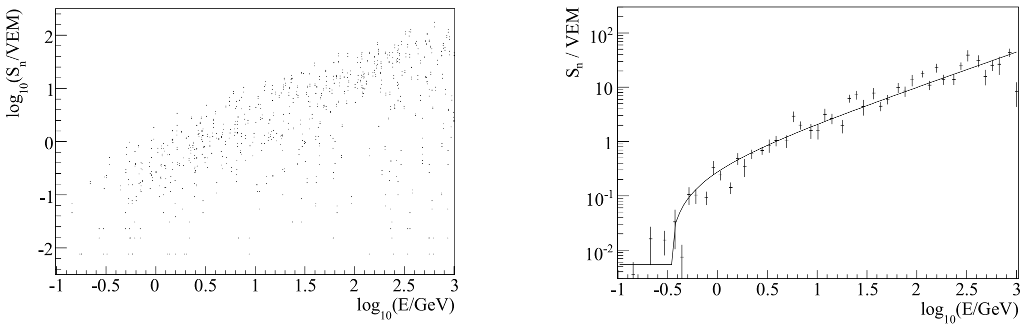
(c) Neutrons

Figure 4.1: Response of IceTop tanks to vertical muons, electrons and neutrons as scatterplots and profiles with fits that were used as parametrisations. These plots represent the typical response expectations of muonic, electromagnetic and hadronic particles.

most abundant particle type in air showers, indirectly become the dominant source of Cherenkov light.

The energy dependence of the tank response of electromagnetic particles is much more pronounced than for muons. As shown in fig. 4.1(b), the light increase coming from both longer track lengths and bigger subshowers is restricted by the geometrical height of the tank, so a slowly decreasing slope can be observed in the logarithmic energy dependence.

4.1.4 Nucleons

The interaction length of high energetic protons or neutrons in ice is $83.6\,\mathrm{g/cm^2}$, which is one tank height [3], and relatively independent of energy. That means that approximately $1/e \approx 63\,\%$ of hadrons in the air shower will interact with the ice and eventually produce a hadronic cascade. The number of secondaries and thus the size of this cascade depends on the particle energy, but the light yield is again restricted by the tank height. Therefore the response expectation function (fig. 4.1(c)) looks qualitatively similar to that of the electromagnetic particles. The fluctuations around that, however, are much bigger due to the hadronic nature of this showering.

The response function of charged hadrons has a minimal pedestal similar to what is observed with muons, coming from particles that do not interact and just produce light as they penetrate the tank.

4.1.5 Other hadronic particles

Besides nucleons, a small amount of pions and kaons can be found in air showers on ground level. These have the additional feature of being able to decay inside the tank or in the snow above it, producing leptons that lead to Cherenkov light, even when the initial meson was below Cherenkov threshold[1]. Besides that, the spectra look similar than the ones for nucleons.

4.2 Fluctuation of Tank Signals

The above response functions only describe the mean tank signal expectation. However, a crucial quantity in a likelihood fit is the distribution of tank signals around that expectation value. Only together they constitute the probability density function of tank signals that is needed to estimate

---

[1] neutrons can also decay to protons, but the energy that is set free from that is very small.

a likelihood for a given shower parameter assumption. These variation distributions are a convolution of fluctuations of the shower, the light propagation in the tank and of the PMT. The variations found are log-normal distributions whose widths can be characterised by the (unitless) standard deviation σ. The dependence of that on the expectated mean signal has been intensively studied with various approaches, using experimental data and different simulation techniques. The outcome of the studies can be found in detail in [75, 76] and will only be outlined here as needed for the understanding of the following analysis.

4.2.1 Tank-to-Tank approach

Having two detector tanks separated by 10 m at each detector station allows the estimation of the total fluctuations experimentally by analysing the signal differences between two such tanks. The response width obtained like this does not depend on any simulation models but has two other drawbacks that cannot be overcome easily. On the one hand, the two tanks are never exactly equidistant to the shower axis, and 10 m separation is enough to eventually lead to slightly different expectation values in the two tanks. That means that in addition to the investigated fluctuation, there is a component that biases the fluctuation to larger values. One could in principle correct for this different expectation by using the reconstructed shower core and the lateral distribution function of the shower signals, but that again leads to model and reconstruction dependencies, which is undesirable and leads to difficult systematic uncertainties, so it was not done. The other disadvantage is that there might be, and surely are, correlations of signals on a scale of 10 m and above. This means that tank-to-tank fluctuations are biased downwards, so it works against the other bias to some extent. Reproducing the measured fluctuations in simulation can verify the latter and thus justify the following circular approach to the problem. As can be seen in fig. 4.2, the general agreement between the two is fairly good, although a small systematic shift remains.

4.2.2 Circular approach

A more unbiased way of simulating fluctuations is to set up an array with a circular tank arrangement, generating vertical showers in their centre. Here, also larger scale fluctuations can be studied, and the expectation value is the same for all tanks. The disadvantage of that, obviously, is that it can only be done in simulation, and thus depends on the shower model and the correctness of the detector simulation.

4.2.3 Results

In fig. 4.2, the dependencies of the fluctuations on the tank signal are summarised as derived from the analyses described above. The features and absolute scale of the two tank-to-tank studies approximately agree, which verifies the quality of simulation. The circular approach leads to slightly lower values that are assumably more realistic though, as discussed above. The line indicates a parametrisation of the points from that, which in full array simulations proved to lead to the best results in core resolution. This one is therefore used in the likelihood function of the reconstruction. Its analytical description is

$$\sigma_S = \begin{cases} 0.283(5) \cdot S^{-0.072(5)} & \text{if } S < 2.13\,\mathrm{VEM} \\ 10^{-0.372-0.661(17)\log_{10} S+0.160(8)(\log_{10} S)^2} & \text{if } 2.13\,\mathrm{VEM} < S < 119\,\mathrm{VEM} \\ 0.0881(18) & \text{if } S > 119\,\mathrm{VEM}. \end{cases} \tag{4.1}$$

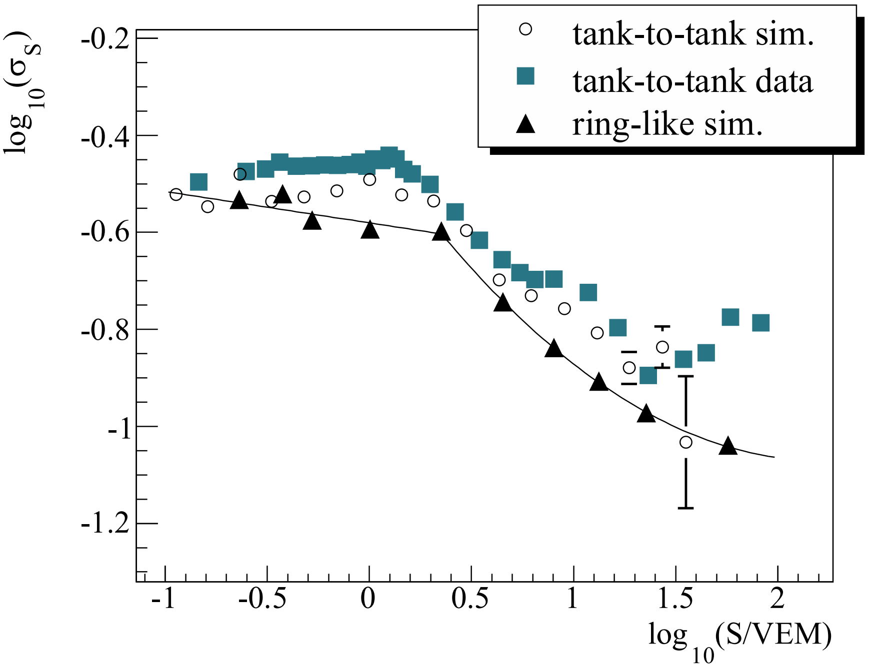

Figure 4.2: Dependence of tank signal flucutations on the absolute signal height. The two tank-to-tank studies yield roughly comparable results, the circular simulation omits the bias of different expectation values and yields a lower result. The line is what is finally used in the likelihood function.

Chapter 5

Reconstruction of Air Showers

In section 3.4, a trigger was introduced that allows for the identification of air showers in the continuous rate of uncorrelated background signals (1.5 to 2 kHz). A coincidence between three stations or more is regarded to be the signature of an air shower detection. Before the statistical analysis of these data, the measured events have to be fitted and basic shower characteristic quantities have to be extracted. These are the location of the shower centre, and the direction, size and the age of the shower (see sec. 1.5.1). From these quantities, an estimation on the energy of the primary particle can be made.

This chapter is dedicated to describe the shower reconstruction algorithms that were developed and applied to the data sample used in this thesis.

5.1 Reconstruction Requirements

The degrees of freedom that a detected shower can hold are the core location (x_c, y_c), direction (θ, ϕ), time (T_0), shower size (S_{ref}) and shower age (s_{NKG}). Although there are cross correlations, one can in general derive the time and direction from the time information of the detected signals, and the core, size and age variables from the distribution of integrated charges. The quantities are determined by a likelihood fit of the data, which requires at least one data point more than degrees of freedom to be fitted. That means it takes four timestamps to reconstruct time and direction and five charges to reconstruct the other quantities. Since the two tanks of an IceTop station cannot be regarded completely independent, and geometrically do not provide a good lever arm, this translates to a minimum reconstruction requirement of five stations. All data presented in the following were required to fulfill this multiplicity threshold.

5.2 First Guess Reconstructions

Before a likelihood fit can be performed, crude estimations of some fitted quantities have to be done to be used as seed values for the iterative likelihood maximisation codes. For each shower, a core position and a direction first guess is calculated analytically from the signal vectors.

5.2.1 Shower COG

For the core position, the centre of gravity (COG) of all measured tank signals S_i can be used as an estimator. However, since the integrated signals decrease rapidly at higher distances from the shower axis, it is a common procedure to use the square root of these signals as a weight instead of the signal itself:

$$\vec{x}_{\mathrm{COG}} = \frac{\sum_i \sqrt{S_i}\,\vec{x}_i}{\sum_i \sqrt{S_i}} \tag{5.1}$$

To the knowledge of the author, this method has no absolute physical justification but was established in numerous previous experiments as being sufficiently good. Since in a small Monte Carlo comparison the convergence of the likelihood turned out not to depend on the weighting, the issue was not further investigated.

5.2.2 Plane Fit

Under the assumption that the front of the shower is a plane, which is a good approximation in vicinity of the shower centre, the χ^2 function of the arrival times of the signals under for a given direction assumption $\vec{n} = (n_x, n_y, -\sqrt{1 - n_x^2 - n_y^2})$, with $|\vec{n}| = 1$, is

$$\chi^2(n_x, n_y, T_0) = \sum_i w_i (t_i^{\mathrm{m}} - t_i^{\mathrm{plane}})^2 = \sum_i \frac{(t_i^{\mathrm{m}} - T_0 + \frac{n_x x_i + n_y y_i}{c})^2}{\sigma_i^2} \tag{5.2}$$

with t_i^{m} being the measured signal times, $w_i = 1/\sigma_i^2$ are their weights and x_i, y_i are the tank coordinates.

If the coordinates of the tanks are transformed to the centre-of-mass system of the pulse data, this function can be minimised analytically and leads to a unique direction if the occurrence of upward-showers (from underneath the detector) is excluded. Since such showers could only be neutrino-induced, and even then would be strongly supressed because of the dense ice, their contribution to the data can be regarded zero.

In eq. 5.2 all tanks are assumed to be at the same height. This wrong assumption is corrected by a second iteration in which the times of all pulses are corrected by $\Delta z/c \cdot \cos\theta$, so their relative height Δz with respect to the mean altitude of the detector is taken into account.

Presently, a constant time uncertainty $\sigma = 5\,\mathrm{ns}$ is assumed in this fit. In real the time resolution depends on the signal height, and on the core position, which is not known at this stage. However, assuming a constant is an approximation good enough to deliver a direction seed that is within about $4\,^\circ$ of the real direction.

5.3 Likelihood Fit

The expected signal height $\langle S(r)\rangle$ as a function of the perpendicular distance to the shower axis r is described by a lateral distribution function (LDF) $S_{\mathrm{ldf}}(r;\vec{p})$ with the shower parameters $\vec{p}$. The radius r_i of a tank i can be calculated from its coordinates $\vec{x}_i$ and these shower parameters, namely the core location $\vec{x}_{\mathrm{core}}$ and direction $\vec{n}$, by

$$r_i = \sqrt{|\vec{x}_{\mathrm{core}} - \vec{x}_i|^2 - (\vec{x}_{\mathrm{core}} - \vec{x}_i)\cdot\vec{n}} \tag{5.3}$$

so that the charge expectation of a tank i can be expressed by $S_{\mathrm{ldf}}(\vec{x}_i;\vec{p})$. The log-normal fluctuations $\sigma(S_{\mathrm{ldf}})$ from that are parametrised by eq. 4.1. Thus the likelihood for a measured signal S_i at a location $\vec{x}_i$ to be caused by a shower with parameters $\vec{p}$ is

$$\mathcal{L}_{\mathrm{hit}}(S_i, \vec{x}_i; \vec{p}) = \frac{1}{\sqrt{2\pi}\sigma}\exp\left(-\frac{(\log_{10} S_i - \log_{10} S_{\mathrm{ldf}}(\vec{x}_i;\vec{p}))^2}{2\sigma(S_{\mathrm{ldf}}(\vec{x}_i;\vec{p}))^2}\right). \tag{5.4}$$

If one of the two tanks at a station has no trigger, the local coincidence condition is not fulfilled and the station is *silent*, i.e. no readout is launched. Assuming the discriminator threshold is S_{thr}, the likelihood for a station at $\vec{x}_i$ to be silent is[1]

$$\begin{aligned}\mathcal{L}_{\mathrm{silent}}(\vec{x}_i;\vec{p}) &= 1 - [P_{\mathrm{tankhit}}(\vec{x}_i;\vec{p})]^{C_t} \\ P_{\mathrm{tankhit}}(\vec{x}_i;\vec{p}) &= 1 - P_{\mathrm{tanksilent}} \\ &= 1 - \int_{-\infty}^{\log_{10} S_{\mathrm{thr}}} \mathcal{L}_{\mathrm{hit}}(S', \vec{x}_i;\vec{p})\, d\log_{10} S'.\end{aligned} \tag{5.5}$$

---

[1] This likelihood is derived from an actual probability instead of a probability density as usual. However, since the difference between the two is usually a constant factor that represents the range in which a measured variable is to be expected, this does not make a difference when multiplying the likelihoods.

Here C_t is a factor that defines how many independent signals a station is regarded to have. If the two tanks are completely correlated it equals 1, and if they are independent it equals 2. Since no study was available showing what it should be or proving that this has a strong impact on the reconstruction, it is presently set to 2. A low correlation hardens the stringency of the upper limit that a silent station represents, so this setting might bias the slope parameters of reconstructed LDFs towards higher (steeper) values. This in deed can be observed and is a point that might require more attention in the future.

The product of all terms in eq. 5.5 and 5.4 defines the overall likelihood, and the logarithm of that is the log-likelihood function of the charge values that is to be maximised to find the shower parameters $\vec{p}$.

Besides the distribution of tank signals (charges), also the actual time distribution of the signals can be included in the likelihood function. Compared to the shower plane assumption in the first guess fit, pulses far from the shower axis are usually delayed as a function of distance (see fig. 5.1). Including this in the likelihood primarily leads to an enhancement of the direction resolution, but also proved to be sensitive to the core position. Presently, this time likelihood is described in χ^2 manner:

$$\mathcal{L}_{\mathrm{time}}(t_i, \vec{x}_i; \vec{p}) = \frac{1}{\sqrt{2\pi}\sigma_t(r_i)} \exp\left(-\frac{(t_i - (t_i^{\mathrm{planefit}} - \Delta t(r_i)))^2}{2\sigma_t(r_i)^2}\right). \tag{5.6}$$

where t_i^{plane} is the estimated time of the plane shower assumption (eq. 5.2), and $\Delta t(r_i)$ the deviation from that. $\sigma_t(r_i)$ is a parametrisation of the time fluctuations. As before, r_i is a function of $\vec{x}_i$ and $\vec{p}$, which is why the likelihood is sensitive to core location and direction.

The parametrisations found in experimental data [77] are

$$\begin{aligned} \Delta t(r_i) &= 19.41\,\mathrm{ns}\;(e^{-\left(\frac{r_i}{118.1\,\mathrm{m}}\right)^2} - 1) - 4.823 \cdot 10^{-4}\,\mathrm{ns}\,\mathrm{m}^{-2}\; r_i^2 \\ \sigma_t(r_i) &= 2.92\,\mathrm{ns} + 3.77 \cdot 10^{-4}\; r_i^2. \end{aligned} \tag{5.7}$$

The additional likelihood can either be added to the charge likelihood function or can be used as an independent fit. As explained below, a compromise between the two turned out to deliver satisfactory performance.

Before that, however, an LDF that is suitable for IceTop shower detections will be introduced.

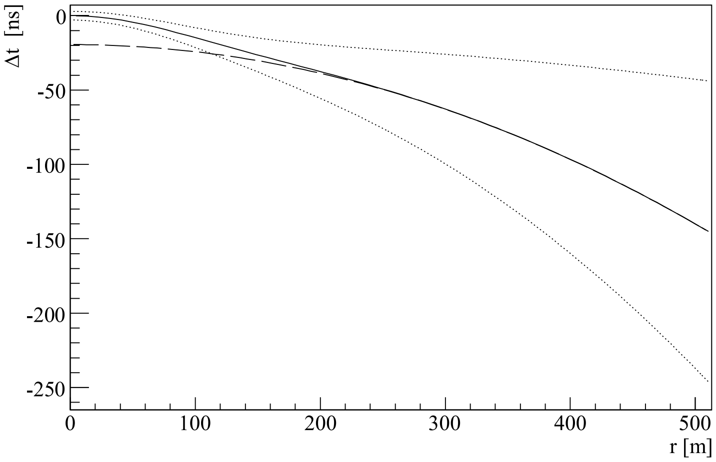

Figure 5.1: Time curvature parametrisation used for the reconstruction (solid line, [77]). It is built out of a parabola (dashed line) with a small gaussian modification at small radii. The dotted lines indicate the 1σ-bands as defined in 5.7.

5.3.1 Lateral Distribution Function

The lateral distribution of tank signals was studied in a combination of CORSIKA air showers and the single particle parametrisation derived in sec. 4.1. Different showers, covering the whole parameter space of energy and zenith angle, were simulated and each single particle was weighted with its expected mean response. In this manner, lateral distributions can be produced to develop an LDF and study the dependence of shower size and age on the primary energy and zenith angle.

Assumptions for this study

Since this is only meant to deliver a fit function and a rough estimator for the energy, some simplifications were undertaken:

- In the detector simulation of section 4.1 only vertical particles were simulated. Hence all particles in this study were effectively treated as if they were vertical. In reality, if they are inclined by a certain angle θ, their potential pathlength is increased by $1/\cos\theta$. This increase of light yield is compensated by the effective area of the tank, which decreases by $\cos\theta$. These effects compensate each other for muons, but probably not exactly for electromagnetic cascades.
- An effect that is neglected along with the previous point is that in-

clined particles, if entering a tank from the side, might undergo an attenuation in the snow before reaching the tank.

- No big efforts were spent to study systematics, since that will be done in a more realistic context in the end of the thesis. For this reason, no different hadronic interaction models or atmosphere parametrisations were tried out. All CORSIKA showers presented here were generated using FLUKA 2006 [51] for low energy interactions ($< 80\,\mathrm{GeV}$), SIBYLL 2.1 [46] for energies above that, and CORSIKA atmosphere number 14 [50], which is a South Pole atmosphere model for December.

Lateral Distributions of Different Showers

Figure 5.2 (left) shows the lateral distribution of electron density in comparison to tank signal (in VEM). At radii up to 400 m, the electron density is well described by an NKG function (eq. 1.10), which has a smooth but clear index change at about the Molière radius. The tank signal lateral distribution is much smoother, it does not have any kinks and is very close to a power law. This is probably because of muons appearing in a relevant abundance at higher radii, since the lateral distribution of muons is generally flatter than that of electromagnetic particles.

A comparison of tank signal distributions of three different showers is shown in fig. 5.2 (right). They only differ in slope and height, but no qualitative shape differences can be seen. The fitted curves are explained below.

The DLP function

The function found to fit these distributions well in a range between 30 and 1000 m is a parabola in the double logarithmic space of $\log(S/\mathrm{VEM})$ and $\log(r/\mathrm{m})$. We therefore call it the "DLP-Function" (**D**ouble **L**ogarithmic **P**arabola) and define it as

$$S(R) = S_{\mathrm{ref}} \left(\frac{r}{R_{\mathrm{ref}}}\right)^{-\beta-\kappa\,\log_{10}\left(\frac{r}{R_{\mathrm{ref}}}\right)} \tag{5.8}$$

The lines through the tank signal distributions in fig. 5.2 are fits with this function. Taking 30 m as the lower fit range makes sure that no thinning effects get into the fitted range (see sec. 1.5.3), which in particular affects the cores of highly inclined showers. The parameters of the function are S_{ref}, β and κ. The *shower size* S_{ref} is the signal height at the reference radius R_{ref} and scales roughly with the primary energy. The β-parameter is

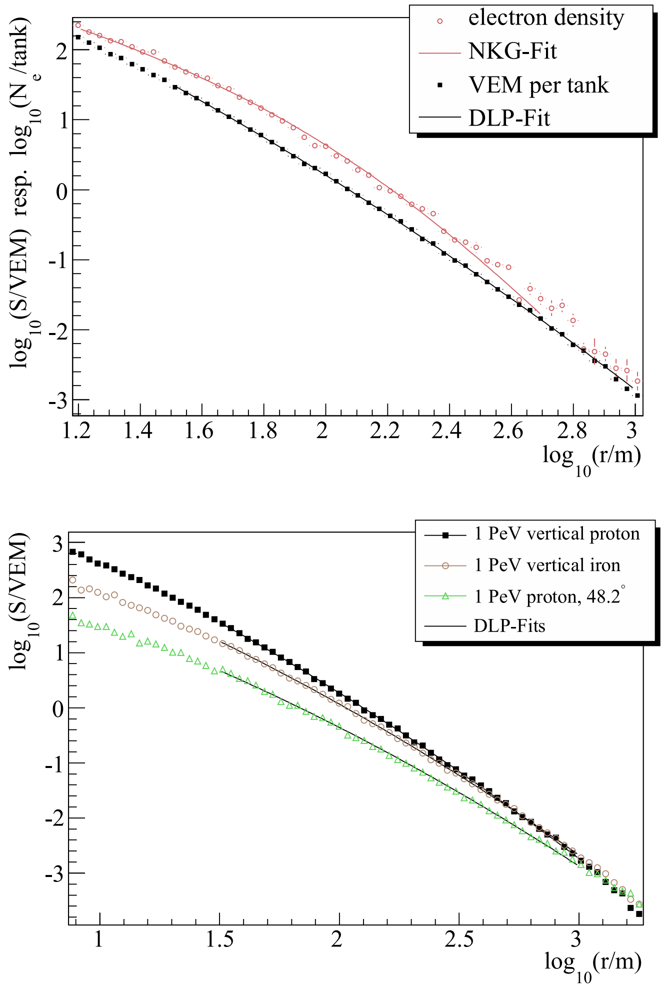

Figure 5.2: Top: Comparison of electron density and tank signal distribution of a 1 PeV proton shower. Bottom: Comparison of tank signal distributions of three different shower types. Both graphs were generated with CORSIKA showers in which each particle was weighted with its expected response.

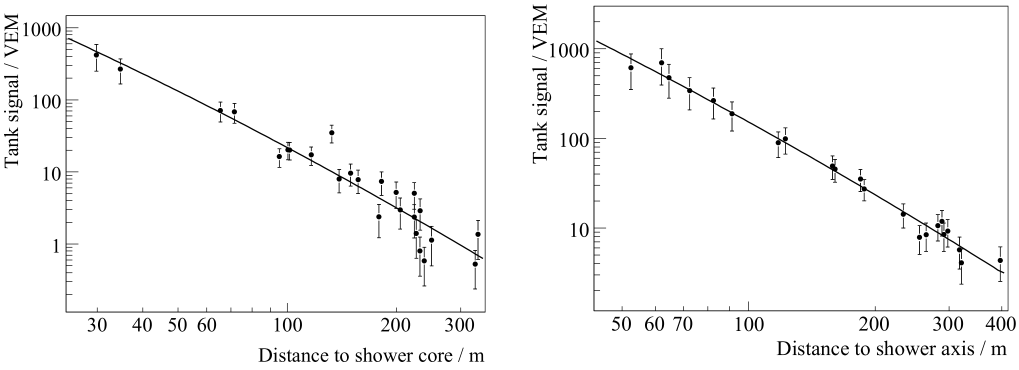

Figure 5.3: Two examples of lateral fits performed on experimental data. The assigned first guess energies of the events are 12.4 PeV and 110 PeV.

equal to the power index, or slope, of the LDF at the reference radius and is connected to the shower age. κ scales with the curvature of the parabola. It is approximately constant $\kappa = 0.303$ for all hadronic showers, while the other two parameters vary event by event.

5.3.2 Fit Procedure and Performance

Figure 5.3 shows two examples of lateral fits performed on experimental data. In general, the fit converges and leads to reasonable results, also if an NKG function or a simple power law is used as LDF. However, independent of which LDF is chosen, the performance of the fit turns out to have some irregularities for a non-negligible part of events. Mainly, these manifest themselves in unphysical values of the age parameter and/or a very distant core location. Also, an effect of too many cores being reconstructed in close vicinity of a station can be observed. The reason for this is difficult to isolate, but is probably a combination of the following flaws:

- The LDFs are almost power laws and as such do not describe the shower well at small distances from the core, where they have a singularity. The real expectation values in the core are very difficult to extract because the phase space is small and the hadronic domination there leads to strong variations.

- At small radii the sizes of the tanks become non-negligible. They can in fact be regarded as a kind of uncertainty in the r coordinate which is not taken into account by the likelihood function.

- Signals extracted from stations that are very close to the shower axis lead to an almost two-point situation in $\log_{10} r$, making the slope parameter strongly depend on the reconstructed core position. This may destabilise the fit, given the above basic problems.

Attempts were undertaken to include the above knowledge in the likelihood function by increasing the uncertainty in the core, and taking the tank size into account. However, this makes the maximisation algorithm push the core even more onto some tank, because that practically dumps at least one signal into a region of high uncertainty and thereby effectively reduces the amount of degrees of freedom by one, which enlarges the likelihood.

Iterative Fit Procedure

To prevent these problems, and following how other experiments handle it, an iterative fit approach was chosen in which pulses that are too close to the core are cut away. This turns out to be very effective for all tested LDFs:

1. A fit is done with restricted slope parameter (β and s_{NKG}, respectively), using all available tank signals.
2. A second fit is done with free slope parameter. If in the first iteration there were signals at $R_i < R^{\mathrm{cut}} = 11\,\mathrm{m}$ from the fitted core, these are cut away in the second iteration. R^{cut} is chosen such that no single tanks, but a whole station is discarded if the core is too close to it. Usually, the iteration ends after this fit.
3. If in the second iteration the core has moved close to some other station, also the pulses of this station are cut away. This is repeated until there are no signals closer than R^{cut} to the core left.

As with all data cuts, the disadvantage of this radial tank signal cut is that some data gets lost, i.e. events with 5 hit stations that get cut end up with only 4 stations, which is below the reconstruction requirement. However, since this is an effect of the fit algorithm only, this can be assumed to be reproduced by the full array simulations presented later.

Verification of Fit Performance

Figure 5.4 shows distributions of several quantities that were chosen to verify the correct performance of the fit and its agreement in experiment and simulation. The variables are

β: The lateral slope parameter.

σ_β: The error of that as derived from the fit.

χ^2: A χ^2 value calculated from all involved charges after the likelihood was maximised. Although this is not the minimised quantity, it can still serve as a quality criterion because it quantifies the distance between fit result and data.

llh: The log-likelihood of measured charges, times and silent stations.

$\mathrm{llh}_{\mathrm{silent}}$: The likelihood of silent stations.

$\sigma_{\log_{10} S_{125}}$: Error of the shower size estimator as derived from the fit.

$\sum_i S_i$: Sum of all charges. Can be regarded as the visible deposited energy of a shower.

$\sigma_x^2 + \sigma_y^2$: Core resolution as derived from the fit.

R_{trans}: Transformation radius (see sec. 5.4.2). It is calculated from the distances of tanks to the shower axis and gives a measure of how extended the shower was seen.

None of the distributions shows any obvious anomalies or unexpected features. The reduced χ^2 distribution of charges in data has a mean of 2.04(4), which indicates the fact that the fit does not minimise this χ^2 but contains likelihood terms for the silent stations and the time information (for one iteration), which both keep the χ^2 at a higher level.

Most of the simulated distributions are in good agreement with experimental data. The differences that are visible can be explained by the discriminator thresholds of simulations being too low; a too low threshold leads to more visible energy, especially at high radii, and a smaller total number of silent stations. This leads to a higher R_{trans} and $\sum_i S_i$, and a lower (absolute) $\mathrm{llh}_{\mathrm{silent}}$ in simulation. Whenever a fix for the threshold problem is available, this can be checked anew.

As a conclusion, the fit behaves quite as expected and the agreement between data and simulation seems to be good enough to use the simulation for response and resolution studies in sec. 5.6.

5.4 Estimation of Energy and Shower Age

From the parameters of the fit, namely S_{ref}, β and the zenith angle θ, physical quantities of the shower and the primary particle can be extracted.

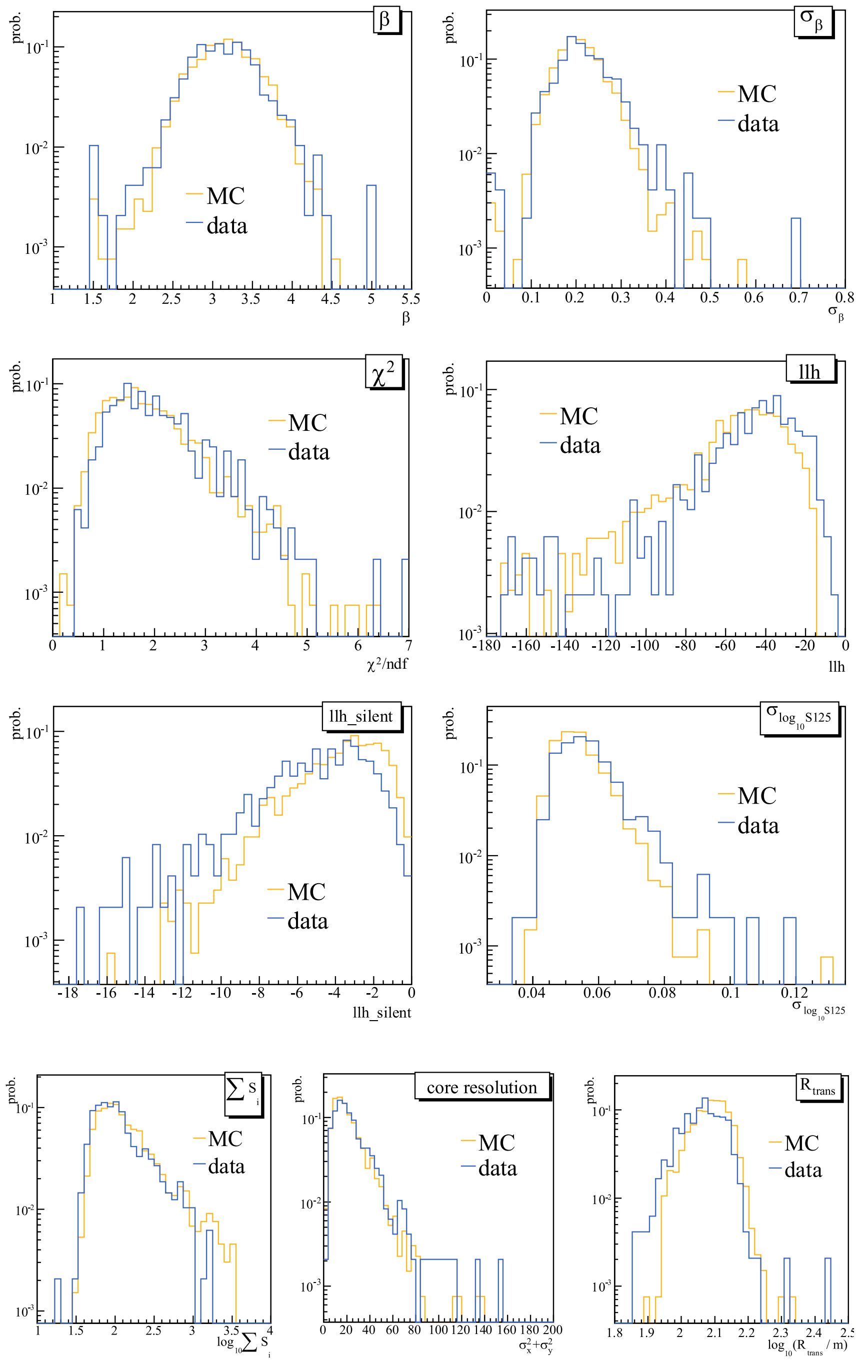

Figure 5.4: Distributions of fit and event quantities in simulation and data.

This was done with the simulations introduced in sec. 5.3.1, which cover the whole relevant zenith and energy range. Since the primary composition is unknown a priori, the goal of this study is to extract proton-equivalent quantities and correct for composition in the analysis of the energy spectrum later.

5.4.1 Shower Size, Zenith Angle and Energy

The shower size at ground level scales with the primary energy, but also depends on the zenith angle. Understanding this dependency allows one to extract an energy estimator for each measured shower size and zenith angle. This estimator is close to reality, but had to be corrected by a second analysis done with full detector simulations. Therefore, it is called *first guess energy* in the following.

CORSIKA showers with response-weighted particles were produced for discrete zenith angles and energies to derive a set of values for $S_{\mathrm{ref}}(E_0, \theta)$ for proton primaries. The result for $R_{\mathrm{ref}} = 100\,\mathrm{m}$ can be seen in fig. 5.5. For higher zenith angles, the amount of traversed atmosphere increases by $\sec\theta$, therefore showers can develop longer. For 1 PeV showers on average this means a decrease of shower size. For higher energetic showers, however, this allows further particle multiplication and they become bigger, before reaching their maximum and decreasing again. This behaviour can be parametrised by parabolas in the $\log(S_{\mathrm{ref}})$-$\sec\theta$-space. To bring all parabolas together in one global fit function, two more assumptions were made, introducing the parameters k_i.

- Each parabola has a maximum at a certain $\sec\theta_{\mathrm{max}}$, i.e. at a certain amount of traversed atmosphere. This approximately scales linearly with the logarithm of the energy:

$$\sec\theta_{\mathrm{max}} = k_1 \log_{10} E_0 + k_2. \tag{5.9}$$

- The logarithm of the height of the shower maximum $S_{\mathrm{ref}}(\theta_{\mathrm{max}}) = S_{\mathrm{ref,max}}$ can also be assumed to be proportional to $\log_{10} E_0$, so that

$$\log_{10} S_{\mathrm{ref,max}} = k_3 \log_{10} E_0 + k_4. \tag{5.10}$$

Combining all of this leads to

$$\log_{10} S_{\mathrm{ref}}(\sec\theta, E_0; k_i) = k_0(\sec\theta - k_1 \log_{10} E_0 - k_2)^2 + k_3 \log_{10} E_0 + k_4. \tag{5.11}$$

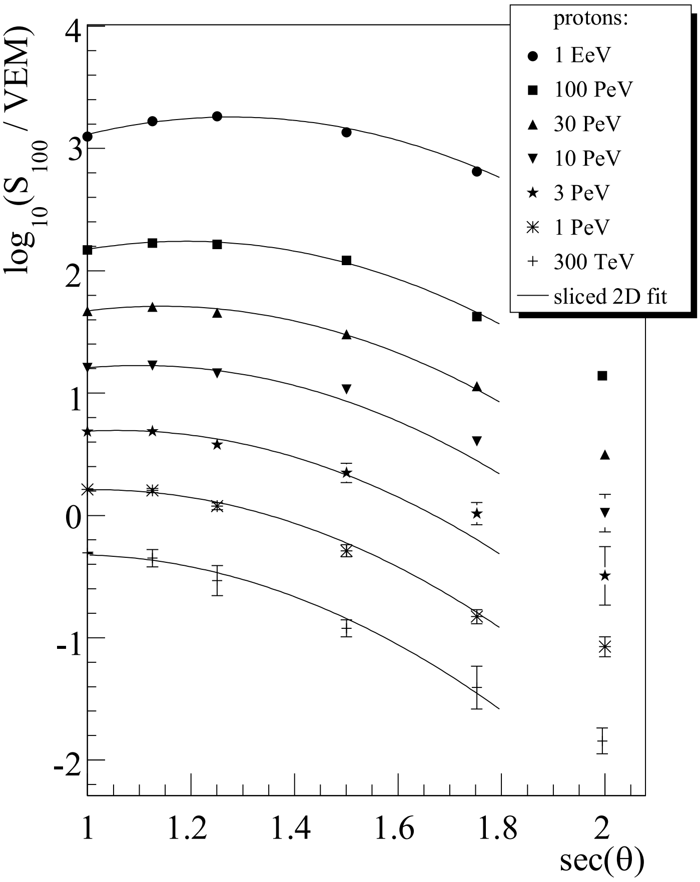

Figure 5.5: Dependence of S_{100} at ground level on the zenith angle and energy. The lines are a two dimensional fit done on all data points, as described in the text. The error bars reflect the amount of events generated for each data point.

A fit of the S_{100} data points in fig. 5.5 can be performed with $\chi^2/\mathrm{ndf} = 41.2/30$ and yields the parameters

$$\begin{aligned} k_0 &= -1.84(6) \\ k_1 &= 0.088(5) \\ k_2 &= 1.013(10) \\ k_3 &= 1.0156(17) \\ k_4 &= 0.210(3) \end{aligned} \tag{5.12}$$

This analytic description of S_{ref} was developed for various reference radii and will be used for energy extraction in sec. 5.4.

Different Primary Particles

As mentioned above, this study aims at an extraction of shower parameters assuming that the primaries were all protons. However, it is good to know in general how strong the described parameterisation might depend on primary particle species, since especially in the energy range observed by IceTop, the composition of cosmic rays is expected to vary considerably. To roughly estimate this uncertainty, small sets of iron showers were simulated at few different energy and zenith bins. Depending on energy and angle of incidence, the mean $\log_{10} S_{100}$ varies by up to 0.1. This is approximately the order of the monoenergetic variations of $\log_{10} S_{100}$, so it is not tremendous, but if for instance the composition would change from complete proton to complete iron in one order of magnitude in energy, this could mean an index uncertainty of 0.1. The issue will thus be quantified more concrete later in this thesis.

5.4.2 Energy Estimation

Equation 5.11 can be inverted and leads to a first guess energy estimator $E^{\mathrm{fg}}(S_{\mathrm{ref}}, \theta)$ that can be determined for each desired R_{ref}:

$$\log_{10} E^{\mathrm{fg}}(\sec\theta, \log_{10} S_{\mathrm{ref}}) = p_0 + p_1 \sec\theta - \sqrt{p_2 + p_3 \sec\theta - p_4 \log_{10} S_{\mathrm{ref}}} \tag{5.13}$$

For example, with $R_{\mathrm{ref}} = 100\,\mathrm{m}$, one gets the parameters

$$
\begin{aligned}
p_0 &= 24.0269\\
p_1 &= 11.3414\\
p_2 &= 459.884\\
p_3 &= 805.717\\
p_4 &= 69.9528
\end{aligned}
\tag{5.14}
$$

To become independent of the radius at which the signal is used to extract the energy, these values were determined for several R_ref so the parameters $p_i(R)$ can be interpolated for any radius R. Figure 5.6 shows graphs of all p_i as a function of the reference radius. The interpolation is done linearly in double-logarithmic scale, so the plots are also drawn like this.

R_ref and R_trans

At this point, to avoid confusion, it is important to distinguish between the reference radius R_ref of the fit function and the energy *transformation radius* R_trans. While R_ref will later be a fixed value which ensures a smooth fit performance, R_trans will be the radius whose $S(R_\text{trans}) = S_\text{trans}$ is the ideal quantity to extract the energy from. It is important to note that the two do not need to be equal, and in general neither of the two has to be a fixed value for all showers.

To find out which is the best value to use as R_ref, a subarray analysis was performed, dividing the array into two arrays with only one tank per station in each subarray. This study can give an estimate on how stable a reconstruction method is with respect to tank fluctuations. Besides other interesting results described in [78], it indicated that

$$R_\text{ref} = 125\,\text{m} \tag{5.15}$$

is a good quantity to chose as fit parameter. Since the fit parameter is most stable where most data points are available, it is not surprising that this equals the mean station distance of the array. There is, however, a dependence on the shower size — big showers have more signals at large radii, so in principle a bigger reference radius could be chosen. In this thesis, a constant value of 125 m was used.

One motivation to define at which R_trans the energy is extracted is to go to a position where the shower signal S_trans is as insensitive as possible to the primary mass. In fig. 1.7, this means chosing the radius at which the longitudinal signal development (for a primary with mean mass) is close to in maximum and thus only little dependent on varying mass. Obviously,

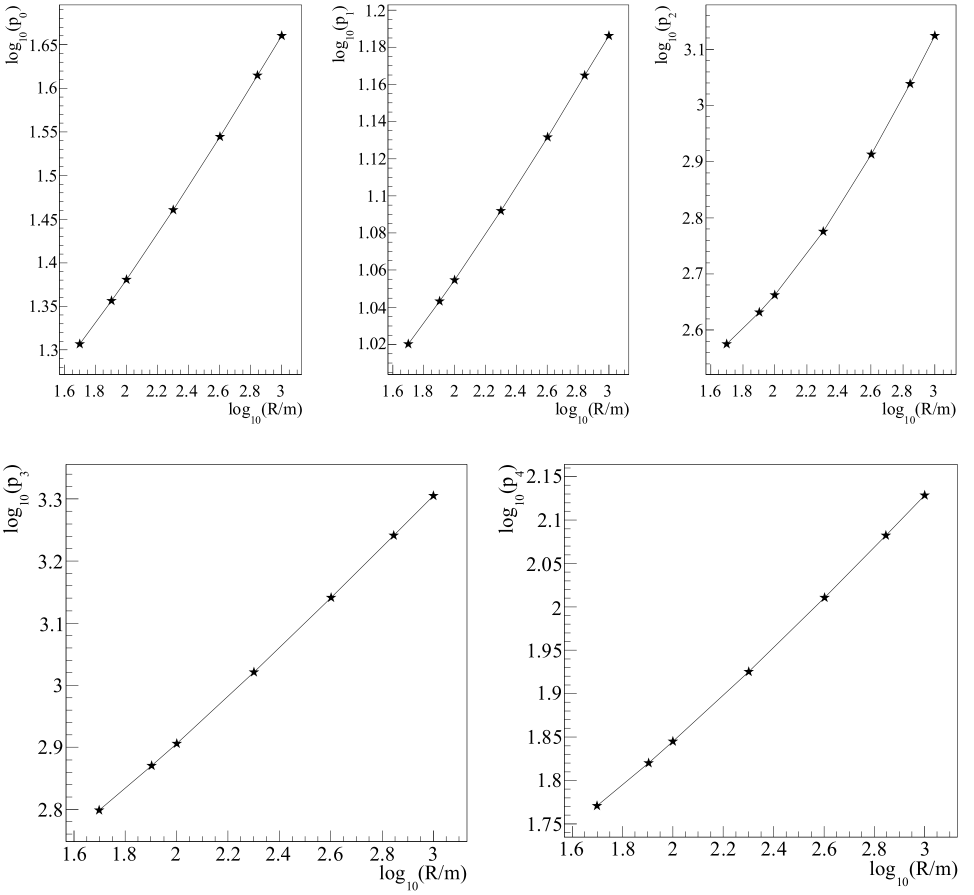

Figure 5.6: Interpolation of parameters p_i of the first guess energy extraction determined for various reference radii.

this radius depends on all other quantities shown in that plot, but mainly on energy and zenith angle. Furthermore, the radius chosen in that way can be too big or too small for the detector spacing, which means that unacceptably big uncertainties would go along with this approach.

A different way of defining R_{trans} is to chose the radius that minimises the correlations between the fit parameters, namely the shower size S_{trans} and the power index β. In a power law fit like that of the LDF, this can be approximated as the centre of gravity of all logarithms of radii:

$$\log_{10} R_{\text{trans}} = \frac{1}{N} \sum_i \log_{10} R_i \tag{5.16}$$

Having the variables uncorrelated has the advantage that the high uncertainty in β has the minimal influence on S_{trans} and thus the energy estimation. This leads to a narrower and more homogeneous energy resolution function. In fig. 5.7 this effect is shown using 500 m and 125 m as fixed R_{trans}, and the flexible approach in comparison. Especially with a radius that is far from the station distance, the resolution becomes much worse and strongly energy dependent.

In fact, it turned out not to be safe yet to rely on the β parameter as long as the number of stations per event is only required to be five and the threshold behaviour is not entirely understood. Simulations show that a higher R_{trans} leads to a slight underestimation, and lower R_{trans} to an overestimation of the energy, which indicates that β might still have a bias towards higher values, i.e. steeper LDFs. If at some point a different definition of R_{trans} will be desired, one should keep in mind to monitor this effect carefully.

To be mathematically precise, an attempt was tried to add the weights of the radii (from the likelihood function) to eq. 5.16. Since for some reason that led to a worse core and energy resolution, this was not done in the following reconstructions.

In all following studies, the first guess energy was determined using S_{trans} at R_{trans} as defined in eq. 5.16.

Second Order Correction

As mentioned, the above formulae to estimate the primary energy were determined from simplified CORSIKA shower studies. In real shower analysis, however, only few measured samples of the shower are available and the likelihood function is based on studies that bear uncertainties, e.g. in the trigger behaviour. Therefore, small deviations between assigned and true energy are found. Figure 5.8 shows the energy misreconstruction of proton

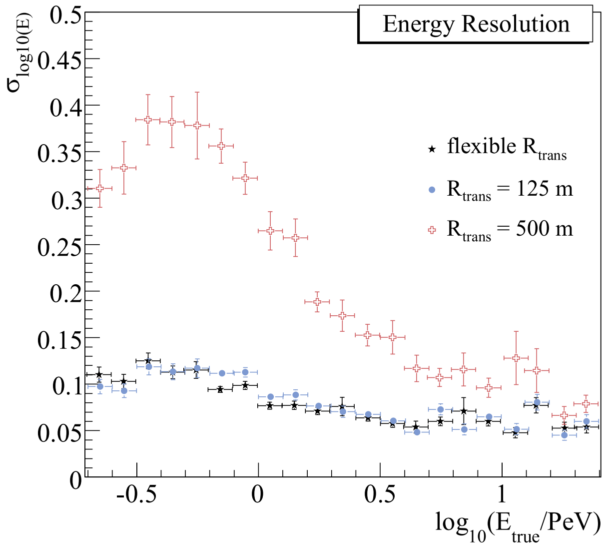

Figure 5.7: Energy Resolution for different definitions of R_{trans}. Choosing a radius outside the range of available signals (here: 500 m) leads to bad resolution and strong energy dependence of it. $R_{\text{trans}} = R_{\text{ref}} = 125\,\text{m}$ yields much better results, but even a bit better is the flexible approach described in the text.

showers as derived with full array simulations as a function of the zenith angle at PeV energies. The deviation from eq. 5.13 can be parametrised by a polynomial

$$\begin{aligned} C(\theta) &= \log_{10}(E^{\text{fg}}/E^{\text{true}}) \\ &= 0.698(11) - 0.299(12)\sec\theta - 0.536(9)\sec^2\theta \\ &\quad + 0.396(7)\sec^3\theta - 0.238(5)\sec^4\theta + 0.103(2). \end{aligned} \tag{5.17}$$

With this and the above E^{fg}, the final estimated energy of a shower, assuming it is proton-induced, is

$$E_0 = E^{\text{fg}} \cdot 10^{-C(\theta)} \tag{5.18}$$

It has to be noted that this correction in log scale is in the order of about 0.1 whereas the attenuation of inclined showers, as already corrected by eq. 5.13, was of order 0.5, which roughly correspond to absolute correction factors of 1.25 and 3, respectively, so the term “second order correction” is justified. This zenith dependent correction, however, was only developed with showers of about 1 PeV, so it does not necessarily correct all deviations

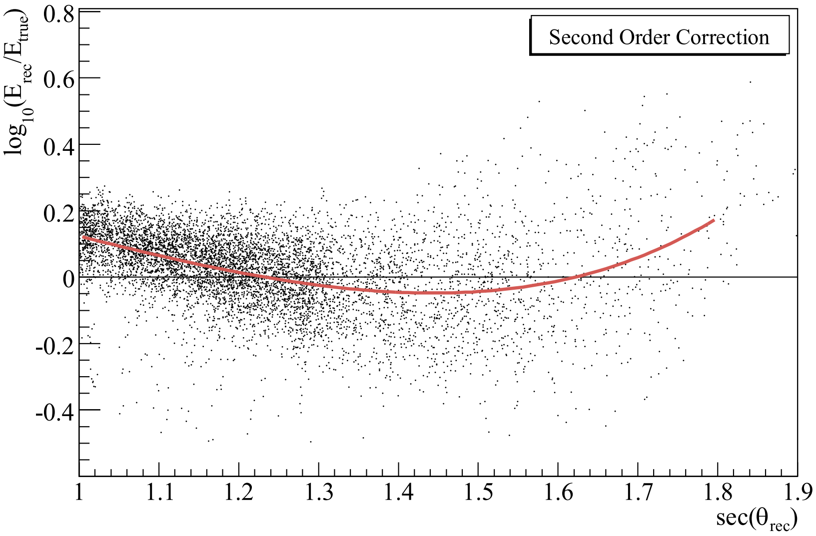

Figure 5.8: Second order correction of the energy determination as gained by full detector simulations.

in the full energy range. It has to be pointed out though that for the results shown later a small standard deviation of the energy response function is much more important than the correctness of its mean value, since the unfolding procedure will take care of shifts anyway.

The main benefit of this adjustment lies mainly in a correct-as-possible energy assignment of single events, assuming they are protons. The distribution of these energies, however, cannot deliver a correct energy spectrum, because migrations and composition are not taken into account in the assignment of energies.

5.4.3 Shower Age and the β Parameter

The NKG shower age, introduced in equation 1.10, can be determined by fitting the lateral electron density distribution of each shower. As can be seen in fig. 5.9, it is roughly linearly connected to the β-parameter of the DLP-function. This is not surprising since the NKG age is also just a slope parameter of the lateral distribution. The formula to convert the two was determined for $R_{\mathrm{ref}} = 100\,\mathrm{m}$ and is

$$s_{\mathrm{NKG}} = -0.94\,\beta_{100} + 3.4 = -0.94\left[\beta + \kappa\,\log_{10}\left(\frac{100\,\mathrm{m}}{R_{\mathrm{ref}}}\right)\right] + 3.4. \quad (5.19)$$

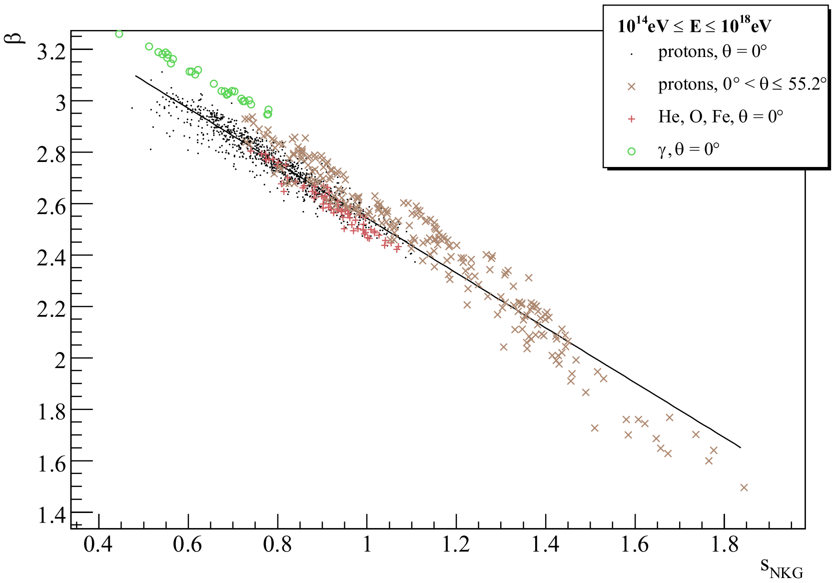

Figure 5.9: The dependence of β on the shower age as determined from an NKG fit. The linear connection holds true for all sorts of hadronic primaries, energies and angles of incidence.

So if a different R_{ref} is used, the fitted β can be converted to β_{100}, which gives the NKG age correctly with the above formula.

5.5 Data Cuts

The resolution and effective area calculations presented in the next section will depend on what cuts are applied on the data, i.e. which quality and geometrical requirements are set on the reconstructed shower events. The cuts described in the following are also applied on the events in the final data sample of the energy spectra presented in chapter 8.

Since the event structure in IceTop is relatively straight-forward (low noise, no background, only one detector component), the contamination of the data by unreconstructable events can be expected to be very low. Also, the acceptance function of air shower arrays at high energies usually approaches a constant. Hence, the general philosophy of event selection in this first physics analysis with IceTop is to leave the cuts as loose and the data as unbiased as possible. A moderate resolution can be corrected with an unfolding algorithm, but a complex bias of a complicated cut variable will cause trouble if it is not perfectly reproduced in simulation. Later analyses might investigate further how the data quality can be optimised with more sophisticated cuts. For example, it might be useful to define clustering pattern requirements once the array is bigger.

5.5.1 Basic Quality Cuts

The goal of the following cuts is to sort out severely misreconstructed events and events with an insufficient amount of signals:

- $N_{\text{station}} \geq 5$: The four lateral fit parameters should go along with at least five independent data points, i.e. stations.
- The likelihood maximisation program (`Minuit`) has to return a "converged" flag, and the value of the likelihood should not equal infinity or be undefined. This also makes sure that none of the time or charge value does.
- $\chi^2_{\text{plane}}/\text{ndf} < 1000$: This avoids that a severely bad direction first guess estimation spoils the lateral fit.

5.5.2 Containment

An important quality filter for any air shower array is to require the events to be inside the array. Shower cores that are outside the array, or only just inside the outer row of tanks, are very difficult to reconstruct, in particular if no high multiplicity is required. This leads to a high uncertainty in the core localisation that directly reflects on the shower size estimatior because the available pulses of the lateral distribution are all on one side of the shower plane. The containment border used in most IceTop studies is defined as a polygon that is 50 m inside the outer array border, which is about half the distance between two tank rows. With the 2007 configuration, this border is a bit arbitrary to define though. The white dashed line in fig. 5.13 shows the borders that were chosen for the presented analysis. It contains an area of $0.12242\,\text{km}^2$.

A completely different issue than defining a geometrical containment criterion is to actually identify a shower as being contained or not. Obviously, the reconstructed shower core should be inside the contained area, but as shown in fig. 5.10, this is not enough. Many showers that are outside the array are reconstructed as being inside, which usually leads to a strong underestimation of primary energy. One way to identify such misreconstructed showers is via their β parameter. A shower that is far outside the array has a relatively flat lateral distribution inside the array. Therefore, if it is reconstructed inside the array, it will be assigned a flatter distribution than other showers that are actually contained. To avoid this from happening in the fit, the β parameter even in the last step of iteration is limited to $1.5 < \beta < 5.0$. Events whose β approaches the boundaries are accepted to avoid this from being an energy and zenith dependent cut that biases the event selection.

Furthermore, if a shower is really contained, one would expect the COG and the station with the highest signal to be also inside the containment borders. This can be used as an additional containment criterion. In a simulation of 1 PeV showers this additional requirement reduced the amount of misreconstructed events from outside the borders by 90 % while discarding only 9 % of the showers that in real are inside the array, so it was decided to use it as a quality cut in the final analysis. As it turns out later, these additional containment criteria effectively reduce the geometrical acceptance area by about 10 %, which is consistent with the above numbers.

Another cut to prevent bad core reconstruction is a cut on the core resolution $\sqrt{\sigma_x^2 + \sigma_y^2}$ as determined by the minimisation program. So the summarised cuts to ensure contained events are:

- $\vec{x}_{\mathrm{core}}^{\mathrm{lateralfit}}$ contained.
- $\vec{x}_{\mathrm{core}}^{\mathrm{COG}}$ contained.
- $\vec{x}_{\mathrm{loudeststation}}$ contained.
- $\sqrt{\sigma_x^2 + \sigma_y^2} < 20\,\mathrm{m}$.

5.5.3 Overall Reconstruction Efficiency

In addition to the tests shown in sec. 5.3.2 it has to be ensured that there is a rough agreement between data and simulation in the event numbers before and after the quality cuts. Since the real cosmic ray spectra are not known a priori, and are not even possible to simulate over the whole energy range (and for all available primaries and zenith angles etc.), one cannot expect a total agreement though.

To make sure that the quality cut survival fractions are not sensitive to threshold effects, which would make them hard to compare, an initial 100 % sample of events was defined as all events that survive the first guess direction and COG estimations, that fulfill the 5 station requirement, and have

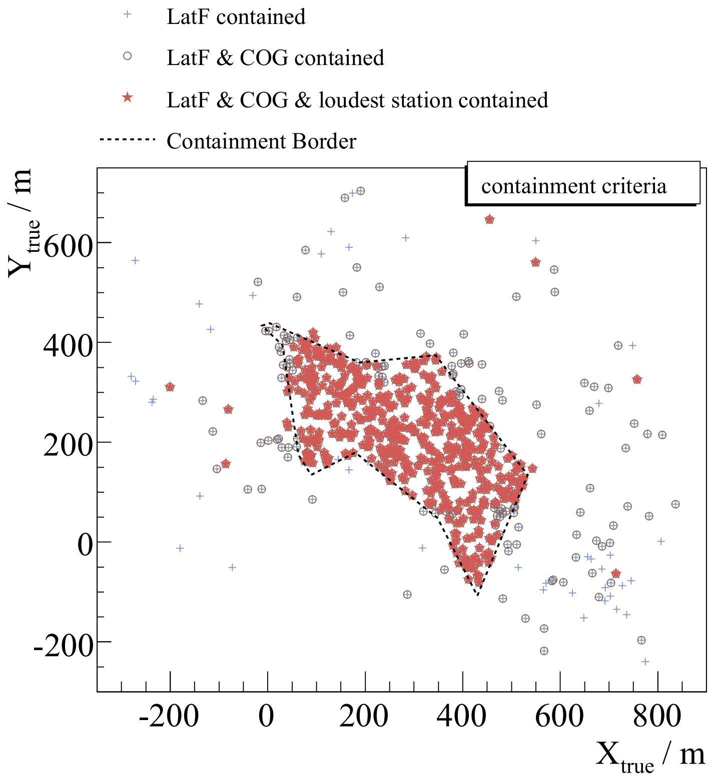

Figure 5.10: Distribution of true cores of 1 PeV showers with a reconstructed lateral fit core (LatF), additional COG, and yet additional loudest station being contained inside the containment borders, indicated with a dashed line. Approximately 20 % of the events are actually not contained. Applying harder containment criteria, only 3 % are left, relative to the remaining number of cores.

Table 5.1: Surviving events due to quality cuts applied to a total of 176595 (10524) experimental (simulated) events with successful first guess reconstruction and contained lateral fit core.

cut	data (%)	simulation (%)
loudest station & COG	89.1	87.2
Minuit converged	84.4	83.7
β and σ_d	84.2	83.6

a shower core from the lateral fit that fulfills the 50 m containment requirement. Also, this study is restricted to showers that have a reconstructed zenith angle below 30 °. There is no obvious reason why showers with higher inclination should differ from that in a way that is not described in simulation. The absolute reconstruction efficiency values for higher zenith angles are calculated in a more precise study in sec. 5.6.4.

Starting from that 100 % sample, the quality cuts are applied in three steps. Table 5.1 shows the amount of data surviving each step for experimental data and all available simulations (up to 10 PeV).

It can be seen that the additional containment cuts are the dominant cuts, while fit convergence and quality only rejects few events.

The numbers of data and simulation differ by $< 1\,\%$, which gives a measure of probable biases due to the quality cuts that are not reproduced in simulation. This can later be used in the estimation of systematic uncertainties.

5.6 Resolution and Effective Area

The detector resolution was studied with a full array simulation using the IceTray software framework. As mentioned in sec. 4.1, this official software does not trace every particle or photon interaction inside the tanks, and thus has the advantage that it is fast enough to allow for the simulation of large amounts of realistic full array data. Therefore it is used here to estimate the resolution functions of the 2007 IceTop array with proton and iron showers in a primary energy range between 100 TeV and 30 PeV. The showers were generated in bins of 0.1 in $\log_{10}(E_0/\,\mathrm{PeV})$ and three zenith bins $[0\,°, 30\,°]$, $[30\,°, 40\,°]$ and $[40\,°, 46\,°]$. The zenith bands are equidistant in $\sec\theta$ and were simulated with additional $\pm 10\,°$ to take bin migration effects into account when each bin is analysed separately in the end[2]. For the following results, all entries of all analysed histograms were weighted with the primary flux spectrum that will be introduced in sec. 6.1. The exact numbers of generated showers are listed in appendix A.

5.6.1 Direction

The shower direction misreconstruction is defined as the opening angle beween true and reconstructed shower direction. The resolution is the angle below which 68 % of the simulated events can be found. The energy and zenith dependence of this resolution with the curved shower front fit is shown in fig. 5.11. Apparently, the resolution is relatively independent of both, so a uniform detector resolution of about 1.5(2) ° can be stated.

5.6.2 Core Position

The core resolution is more interesting, not only because the analysis depends on the core position, but because it gives a measure on how well the lateral fit works at different energies. It can be seen in fig. 5.12 that the precision of the core determination does profit from a stronger signal. The maximum resolution is reached at around 3 PeV, where it approaches 8.8(5) m. For higher inclination it is slightly worse, but also ends up in the same range at high energies.

Another feature of the core reconstruction can be found in comparison of the distributions of true and reconstructed cores shown in fig. 5.13. A region where particularly many true cores fall close to a tank is marked with a dashed ellipse. It can be seen that in the reconstructed distribution, this excess (and other similar ones) is gone. This can also be seen in the data plot, where a much larger statistical sample of showers can be displayed. Actually there is a lack of showers around almost each station. This effect is probably due to the inhomogenity of the core resolution function — a shower core can be determined with higher precision if it is between several station than if it falls very close to a station. This leads to more core migration from stations to the surrounding area than in the opposite direction. Investigating the two-dimensional core resolution function would help confirming this hypothesis, but was not done within this thesis.

---

[2] This oversampling is not necessary for the energy bins because they are always used together. In this way, the migrations are generated automatically from adjacent bins.

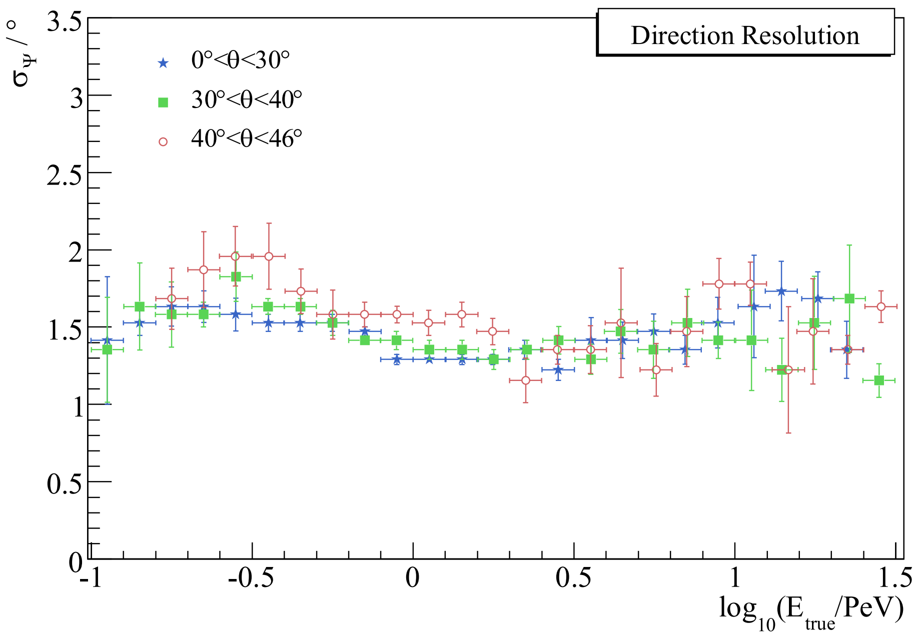

Figure 5.11: Energy dependence of the direction resolution for three zenith bins, studied in full-array simulations of proton showers. (In this and all following figures, some points with high statistical uncertainties were omitted for better illustration. Also, it shall be noted that the error bars do not reflect the possible effects due to oversampling of some showers, so the real errors might be slightly bigger, especially at high energies where the relative oversampling is higher).

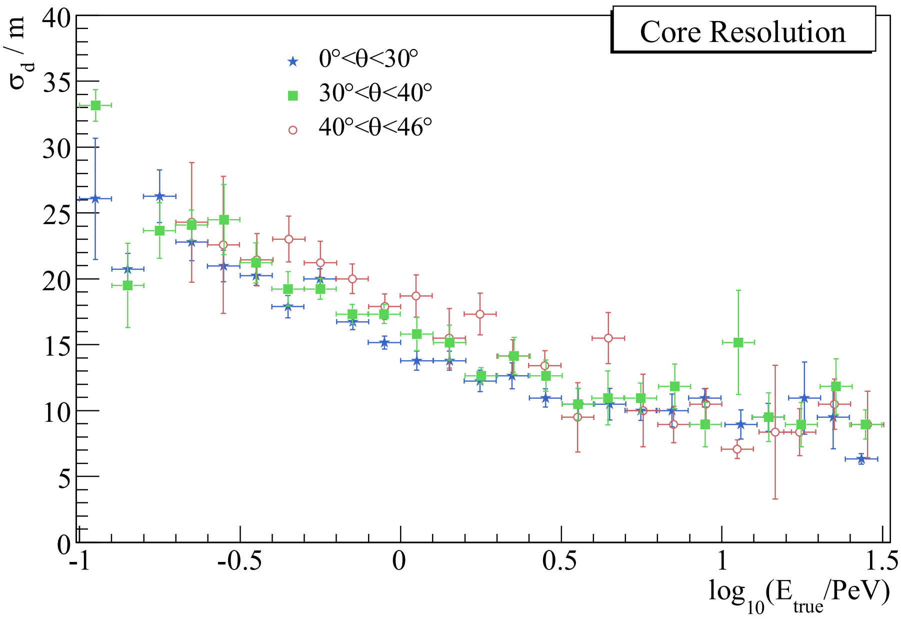

Figure 5.12: Energy dependence of the core resolution for three zenith bins, studied in full-array simulations of proton showers. A strong dependence, ending in a saturation, can be observed. (See also comment below fig. 5.11.)

5.6.3 Energy

The crucial point of this thesis of course is the energy reconstruction. The energy response distributions, as the signal fluctuations, are approximately Gaussian distributions on log-scale (fig. 5.14). That means that the energy response can be described by an energy dependent *energy resolution* $\sigma_{\log 10 E}$, *energy misreconstruction* $\Delta \log_{10} E = \overline{\log_{10} E^{\text{rec}}} - \overline{\log_{10} E^{\text{true}}}$ and *reconstruction efficiency* $\varepsilon = A^{\text{eff}}/A^{\text{cut}}$. The latter will get more attention in the next paragraph. The evolution of resolution and misreconstruction is illustrated in fig. 5.15. The resolution improves from 0.12 at lower energies to about 0.05 at higher energies, which translates to a resolution of 12 % in absolute scale. Unlike in the core or direction resolution, the dependence on the inclination is visible more strongly, which is most probably connected to the fact that inclined showers have more possibility to diverge in their longitudinal development.

The energy misreconstruction is strongly positive at small energies and approaches zero at PeV energies, depending on zenith angle. The deviations are a natural consequence of a steep acceptance slope — showers that fluctuate upwards have a higher probability of being detected than downwards fluctuating ones. Once the efficiency approaches a constant, the misrecon-

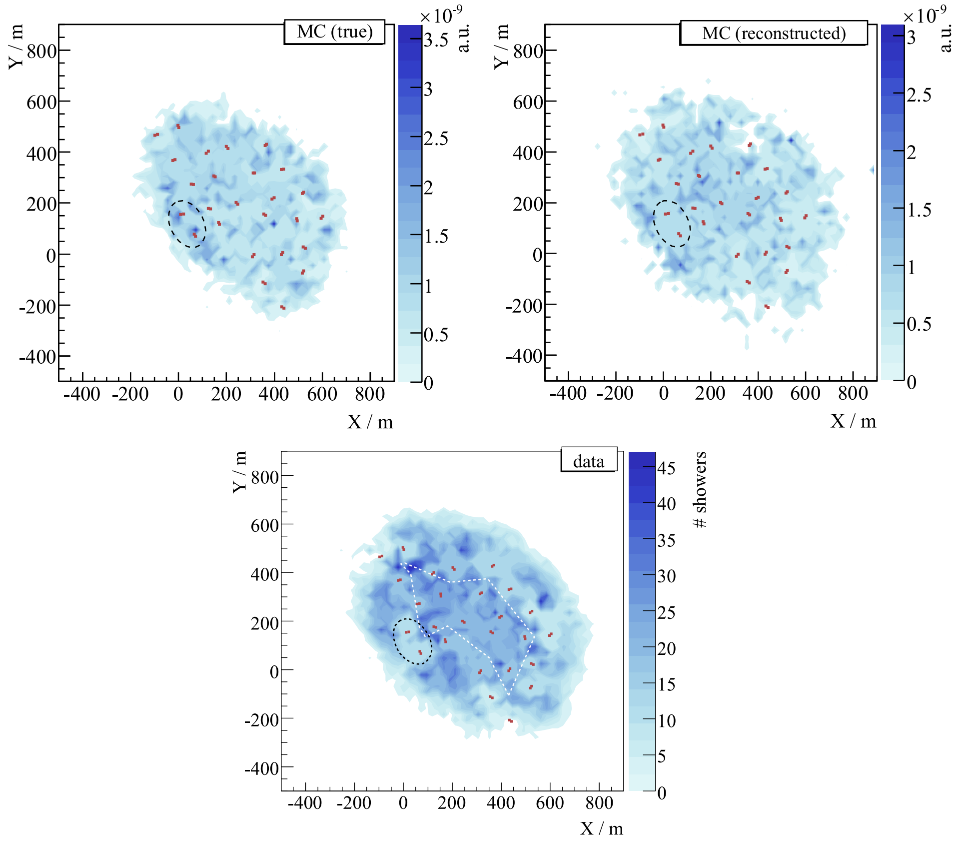

Figure 5.13: Shower core distribution of 3527 simulated showers (true and reconstructed) and 18719 real showers. All showers (also for the “true” plot) were required to have a reconstructed energy above 3 PeV and a reconstructed zenith angle below 30 °. The data plot also shows the area inside which an event is regarded contained (white dashed line), and the tank positions in 2007 (squares). The dashed ellipse is explained in the text.

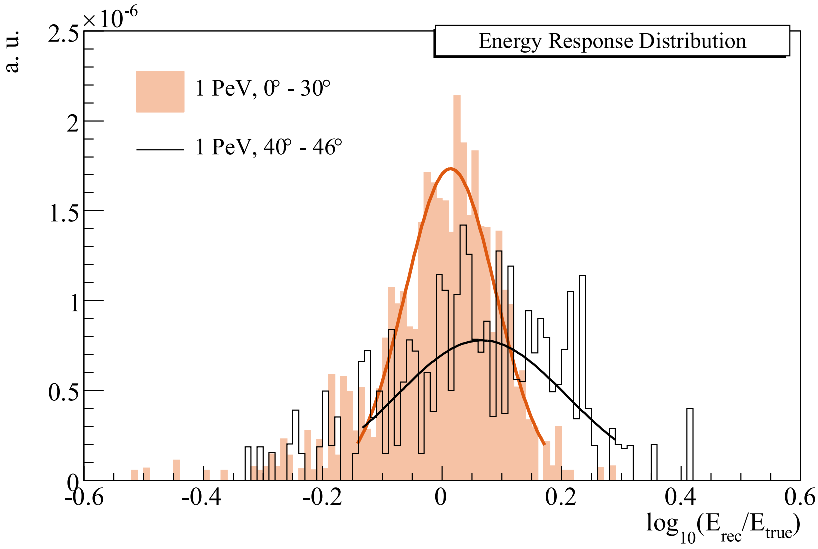

Figure 5.14: Energy response distributions of PeV showers at two different inclinations. The lines are gaussian fits used for parametrisation. The fit range is always determined from the histogram mean and RMS as Mean $\pm$ $1.5 \cdot$ RMS. The χ^2/ndf of the shown distributions are 1.2 and 1.1.

struction is in the order of ± 0.05. This could in principle be corrected by a third-order correction term. However, since it does not matter after the unfolding, and is dependent on the cuts and thus different for every analysis, it was decided to accept it like this. The additional deviations that occur when different primaries are considered will be discussed in chapter 6.2.2.

The resolutions found (1.5 °, 8.8 m, 12 %) depend on the cuts, but in general are very competitive with the resolutions achieved by KASCADE-Grande (0.3 °, 13 m, 15 %, see sec. 1.5.2).

5.6.4 Effective Area

The effective area is a basic characteristic of each detector, quantifying its possibilities of capturing a certain exposure in a reasonable time scale. For each of the three zenith bands, it can be calculated as

$$A^{\text{eff}} = \frac{N^{\text{rec}}}{N_\theta^{\text{gen}}} A^{\text{gen}} \tag{5.20}$$

where N^{rec} is the number of events reconstructed as being inside the zenith bin, N_θ^{gen} is the number of events generated inside the zenith range (excluding the events in the additional $\pm 10\,°$), and $A^{\text{gen}} = A_{\text{d}}^{\text{gen}} \cdot (\cos\theta_0 + \cos\theta_1)/2$

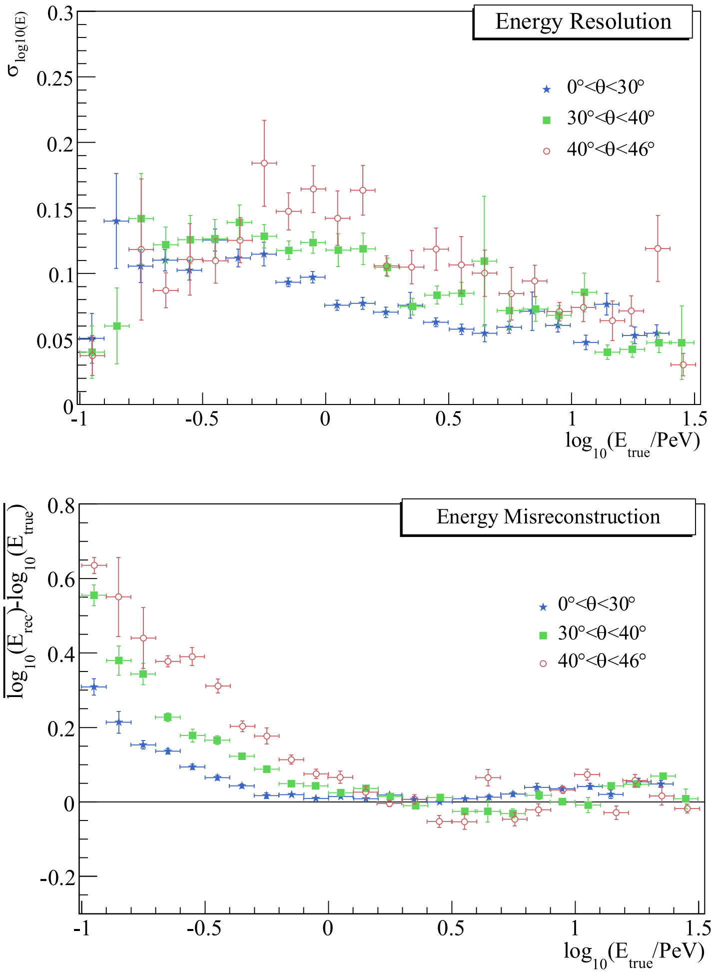

Figure 5.15: Energy dependence of energy resolution and misreconstruction for three zenith bins, studied in full-array simulations of proton showers. (See also comment below fig. 5.11.)

is the mean perpendicular generation area for that zenith bin. $A_{\mathrm{d}}^{\mathrm{gen}}$ is the generation area in the detector plane, as provided to CORSIKA. In that context, the efficiency can be defined as

$$\varepsilon = \frac{A^{\mathrm{eff}}}{A^{\mathrm{cut}}} = \frac{N^{\mathrm{rec}}}{N_{\theta}^{\mathrm{gen}}} \frac{A^{\mathrm{gen}}}{A^{\mathrm{cut}}} \tag{5.21}$$

where as above A^{cut} is the effective cut area perpendicular to the shower incidence.

Figure 5.16 shows the energy dependence of the effective areas of the three zenith bands. For comparison, $A_{\mathrm{d}}^{\mathrm{cut}}$, the cut area in the detector plane, is drawn as a dashed line. All three curves approach a maximum which can be regarded as the (constant) effective area above threshold. The dotted curves are fits of fermi functions that turned out to be useful to determine these effective areas. For the investigated zenith bins, the results are

$$\begin{aligned} A^{\mathrm{eff}}_{0^\circ-30^\circ} &= 0.0936(16)\,\mathrm{km}^2 \\ A^{\mathrm{eff}}_{30^\circ-40^\circ} &= 0.0850(21)\,\mathrm{km}^2 \\ A^{\mathrm{eff}}_{40^\circ-46^\circ} &= 0.0792(27)\,\mathrm{km}^2. \end{aligned} \tag{5.22}$$

In terms of efficiency, this translates to

$$\begin{aligned} \varepsilon_{0^\circ-30^\circ} &= 0.818(14) \\ \varepsilon_{30^\circ-40^\circ} &= 0.845(21) \\ \varepsilon_{40^\circ-46^\circ} &= 0.88(3). \end{aligned} \tag{5.23}$$

These values may be regarded compatible with each other, so an overall efficiency of 0.840(15) can be given. This is in good agreement with the values in tab. 5.1. It is important to note that this efficiency is below 100 % mainly because the containment cuts reduce the acceptance area, and not because the algorithms failed to reconstruct showers.

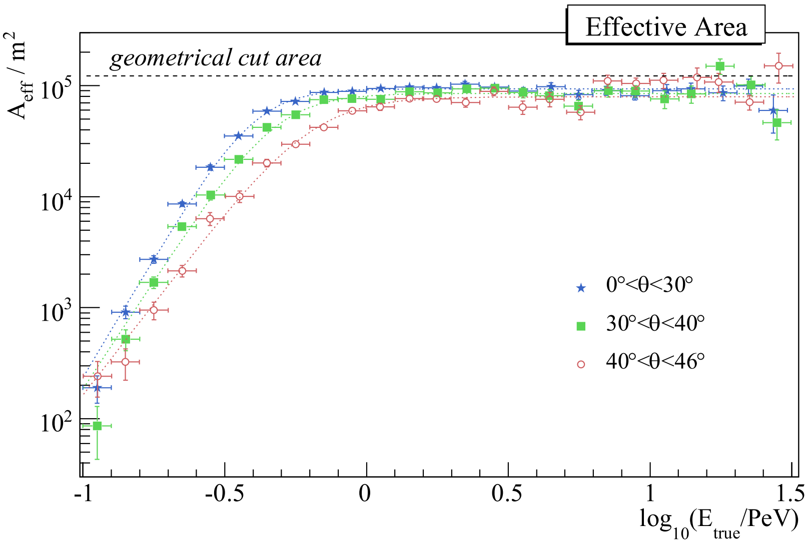

Figure 5.16: Reconstruction threshold function in terms of effective area for three zenith bins, studied in full-array simulations of proton showers. The dotted lines are the fits used to determine the limits approached by the curves. (See also comment below fig. 5.11.)

Chapter 6

IceTop Energy Response and Raw Spectrum

It was shown in the previous chapter that the energy reconstruction of a primary cosmic ray is randomly smeared out by a distribution that is Gaussian on a logarithmic scale. The mean, width and height of this distribution is energy dependent, which means that a measured distribution of energies can vary from the real flux in absolute scale, energy and in the power index. The connection between real and measured spectrum is the response matrix of the energy reconstruction.

This chapter will first introduce four possible composition assumptions and calculate response matrices for each of them. The corresponding measured energy distributions to be expected are shown, assuming a given all-particle spectrum. The results are discussed and power law fits are performed.

6.1 Composition and Flux Models

To show the band of possible variations due to the unknown composition of nuclei, four composition assumptions are used in the following:

- only protons
- "poly-gonato composition", motivated by [6]
- "two-components composition", motivated by [79]
- only iron

Here, "motivated by" means that small modifications had been done to make the parameterisations easier to handle and compare. On the one hand, the two-components spectrum was brought to the form suggested in the publication of the poly-gonato composition:

$$\frac{dI}{d\log_{10} E} = I_{\mathrm{PeV,lg}} \cdot \left(\frac{E}{1\,\mathrm{PeV}}\right)^{\gamma_1+1} \cdot \left(1 + \left(\frac{E}{E_{\mathrm{knee}}}\right)^{\varepsilon}\right)^{(\gamma_2-\gamma_1)/\varepsilon} . \tag{6.1}$$

Here $I_{\mathrm{PeV,lg}}$ is the flux at 1 PeV per $\log_{10}(E/1\,\mathrm{PeV})$ in units of $\mathrm{m}^{-2}\,\mathrm{s}^{-1}\,\mathrm{sr}^{-1}$, $\gamma_{1,2}$ are the power indices before and after the knee, and ε is a parameter for the smoothness of the knee. The latter could not be definitely clarified from the paper of the two-components model, so the same value as in the poly-gonato approach was used ($\varepsilon = 2.1$).

In the poly-gonato parametrisation, not every single component was considered, but five groups of nuclei were defined instead. The indices and atomic numbers were calculated as weighted averages over the nuclei involved in each group. Finally, a factor of 1.08 was applied to compensate for the missing minor nuclei in between the atomic groups. This does not affect the relative composition, but just makes sure that adding the single components up leads to a good agreement with the all-particle spectrum of the original poly-gonato publication.

The constants used are listed in tab. 6.1. Figure 6.1 shows the relative compositions of the two mixed composition models. In the following folded energy spectra, the all-particle spectrum of the poly-gonato approach was used for all four models, and the relative abundances were applied instead of keeping the different absolute normalisations of the models. This makes it easier to see the actual influence of the composition. In fact, the absolute scales of the two models involved do not influence the energy spectrum deconvolution at all.

6.2 Features of the Energy Reconstruction

The energy resolution $\sigma_{\log 10(E)}$, misreconstruction $\Delta \log_{10} E$ and efficiency ε of the reconstruction, as presented in sec. 5.6, define the energy response of the present array and reconstruction under the cuts described in section 5.5. They can thus be used to build up a response matrix.

6.2.1 Response Matrix

Following the nomenclature of [80], the true energy spectrum can be regarded as a distibution of *causes* $\vec{C}$, where each C_j corresponds to a num-

Table 6.1: Constants of the input spectrum assumptions. $I_{\mathrm{PeV,lg}}$ is given in terms of $10^{-6}\,\mathrm{m}^{-2}\,\mathrm{s}^{-1}\,\mathrm{sr}^{-1}$, E_{knee} in PeV.

model		A	Z	$I_{\mathrm{PeV,lg}}$	$-\gamma_1$	$-\gamma_2$	E_{knee}
only protons	H	1.0	1.0	5.47	2.66	3.08	3.08
poly-gonato	H	1.0	1.0	1.61	2.71	$-\gamma_1 + 2.1$	4.49
	He	4.0	2.0	1.71	2.64	$-\gamma_1 + 2.1$	$Z \cdot E_{\mathrm{knee,H}}$
	CNO	14.2	7.1	0.673	2.67	$-\gamma_1 + 2.1$	$Z \cdot E_{\mathrm{knee,H}}$
	Mg-S	27.2	13.5	0.514	2.64	$-\gamma_1 + 2.1$	$Z \cdot E_{\mathrm{knee,H}}$
	Mn-Fe	55.7	25.9	0.997	2.57	$-\gamma_1 + 2.1$	$Z \cdot E_{\mathrm{knee,H}}$
two-comp.	H	1.0	1.0	3.89	2.67	3.39	4.1
	Fe	1.0	1.0	1.95	2.66	–	–
only iron	Fe	56.0	26.0	5.47	2.66	3.08	3.08

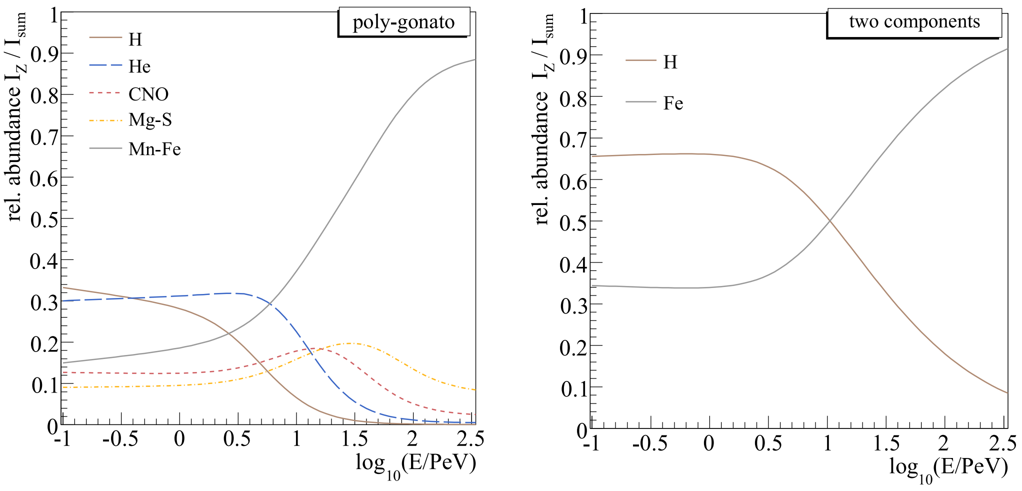

Figure 6.1: Relative composition evolution in the two composite models that were taken into account in the analysis.

ber of events in the true energy bin E_j^{true}. The measured distribution of reconstructed energies is a histogram of *effects* $\vec{F}$ in the detector, where again each F_i is the number of events belonging to energy bin E_i^{rec}. The probability of a true event in j to be reconstructed into bin i is given by the response matrix R_{ij}. The connection between a measured and a true distribution is given by

$$\vec{F} = \mathbf{R}\vec{C} \tag{6.2}$$

The sums over the column and row vectors of the response matrix are

$$\begin{aligned} \sum_i R_{ij} &\equiv \varepsilon(E_j^{\text{true}}) \\ \sum_j R_{ij} &\equiv 1. \end{aligned} \tag{6.3}$$

The first line is the detection efficiency of true events in j, the second line guarantees that every measured effect in bin i is generated by exactly one cause.

The values R_{ij} can be derived from simulated response distributions as for instance shown in fig. 5.14. The fits performed on these distributions correspond to weighted probability density functions (p.d.f.) $p_w(E^{\text{rec}}; E_{\text{c}}^{\text{true}})$ of measured effects for a given cause energy $E_{\text{c}}^{\text{true}}$, which in this context is the centre of the simulated energy bin. The events in the distribution have to be weighted by the expected flux to take into account the fact that causes are distributed unevenly within the bins.

Each $p_w(E^{\text{rec}}; E_{\text{c}}^{\text{true}})$ has parameters that can be interpolated between the investigated $E_{\text{c}}^{\text{true}}$ to get a continuous function $p_w(E^{\text{rec}}; E^{\text{true}})$. From this, the elements of the response matrix can be calculated by

$$\begin{aligned} R_{ij} &= \frac{\int_i \int_j p_w(E^{\text{rec}}; E^{\text{true}})\, dE^{\text{true}} dE^{\text{rec}}}{\int_j dE^{\text{true}}} \\ &= \frac{(\overline{p_w})_{ij}\, \Delta E^{\text{true}}\, \Delta E^{\text{rec}}}{\Delta E^{\text{true}}} \\ &= (\overline{p_w})_{ij}\, \Delta E^{\text{rec}} \end{aligned} \tag{6.4}$$

Here, $(\overline{p_w})_{ij}$ is the average value of p_w in the the cell $\Delta E^{\text{true}} \Delta E^{\text{rec}}$ enclosed by the bins E_i^{true} and E_i^{rec}.

To do the interpolation of the response parameters, appropriate fit functions were developed. The interpolation is necessary to avoid the statistical uncertainties of the air shower simulations to be transfered to the data sample (which has better statistical quality) in the unfolding procedure. Also, a fitted function with a phenomenological justification offers a natural way of extrapolating the parameters to higher energies not covered by the simulation.

The functions found to fit the energy dependence of the energy resolution and misreconstruction were formulated in a way that one parameter – p_0 – gives the absolute parameter value at 1 PeV while the other parameters define the shape of the curve relative to that. In this way, the error of p_0 can give an estimate of the overall normalisation uncertainty of the curve:

$$\Delta \log_{10} E = p_0 + \ln\left(\frac{e^{p_1 \log_{10} E^{\text{true}}} + e^{p_2 \log_{10} E^{\text{true}} + p_3}}{1 + e^{p_3}}\right) \tag{6.5}$$

$$\sigma_{\log 10(E)} = \frac{p_0(1 + e^{p_3 p_4}) + e^{-p_1}(e^{-p_2 \log_{10} E^{\text{true}}} - 1)}{1 + e^{-p_3(\log_{10} E^{\text{true}} - p_4)}} \tag{6.6}$$

Equation 6.5 is essentially the logarithm of the sum of two exponential functions that describe the decrease in the acceptance regime and the slight increase that in some cases occurs in the regime of full efficiency (see fig. 6.2). The high misreconstruction and low response width at low energies is a result of event truncation in the acceptance regime — a shower of some hundred TeV only has good probability of being triggered and reconstructed if its shower size fluctuates upwards. Therefore, the mean reconstructed energies of those events appears too big while the spread of energies appears smaller.

Equation 6.6 assumes that for high energies the resolution approaches a constant, while towards low energies it first increases because of less available signals, but finally becomes smaller again because of the mentioned truncation effects.

The efficiency can be fitted by

$$\varepsilon = \begin{cases} \dfrac{p_0}{1 + e^{-p_1(\log_{10} E^{\text{true}} - p_2)}} & \text{if } \log_{10} E^{\text{true}} > p_4 \\ \dfrac{p_0}{1 + e^{-p_1(\log_{10} E^{\text{true}} - p_2) + p_3(\log_{10} E^{\text{true}} - p_4)^2}} & \text{if } \log_{10} E^{\text{true}} < p_4 \end{cases} \tag{6.7}$$

Here, p_0 is the maximum efficiency that is approached at higher energies. Towards lower energies, this threshold function approaches a parabola in $\log(\varepsilon)$. A different approach that was tried out was to assume that the efficiency approaches a straight line instead of a constant. The slopes of these lines, however, were always compatible with 0, so to avoid problems when extrapolating, a constant was prefered.

6.2.2 Proton, Iron and Other Primaries

Showers of heavier nuclei develop faster and thus reach their maximum earlier than proton showers (see also fig. 1.7). This leads to a misinterpretation of their energy, because they reach the ground at a different stage than expected if they were protons. For example, given the location of IceTop, the energies of iron showers below 30 ° inclination are underestmated below 15 PeV, and overestimated above. This value depends on the shower size parameter, and thus the radius that the energy is extracted at (eq. 5.16). So defining R_{trans} at a different radius from the shower axis will also change this transition energy.

In any case, this behaviour leads to a tilt of the iron response matrix with respect to the proton response. Figure 6.3 shows a graphical comparison of the two matrices. At energies around 1 PeV, the misplacement of iron energies is around -0.15 in log-scale, which is bigger than the resolution. It should be noted that a redefinition of the energy estimator, taking into account some composition assumption, would not eliminate the uncertainty but only would only tilt both matrices.

Besides that, the fact that in the figure both matrices are monotone and lined up close to the diagonal verifies that the increase of misreconstruction at low energies merely comes from the truncation mentioned above.

Response Matrices of Other Primaries

In principle, a matrix $\mathbf{R_Z}$ should be calculated for every abundant primary nucleus Z. In this thesis, however, an alternative approach was pursued. Since the energy misassignment for nuclei between proton and iron cannot be bigger than the one observed for iron, an approximation can be evaluated assuming that the response of these intermediate nuclei can be described as a superposition of the proton and iron responses:

$$\mathbf{R_Z} = \frac{A_{\text{fe}} - A_z}{A_{\text{fe}} - A_{\text{p}}}\,\mathbf{R_p} + \frac{A_z - A_{\text{p}}}{A_{\text{fe}} - A_{\text{p}}}\,\mathbf{R_{fe}} \tag{6.8}$$

It shall be noted that this will not entirely resemble reality, since the point where a response diagonal of a lighter nucleus crosses the one of protons can be expected at lower energy than for iron, whereas eq. 6.8 technically only varies the tilting angle. Still it should be a good starting point that might be optimised sometime.

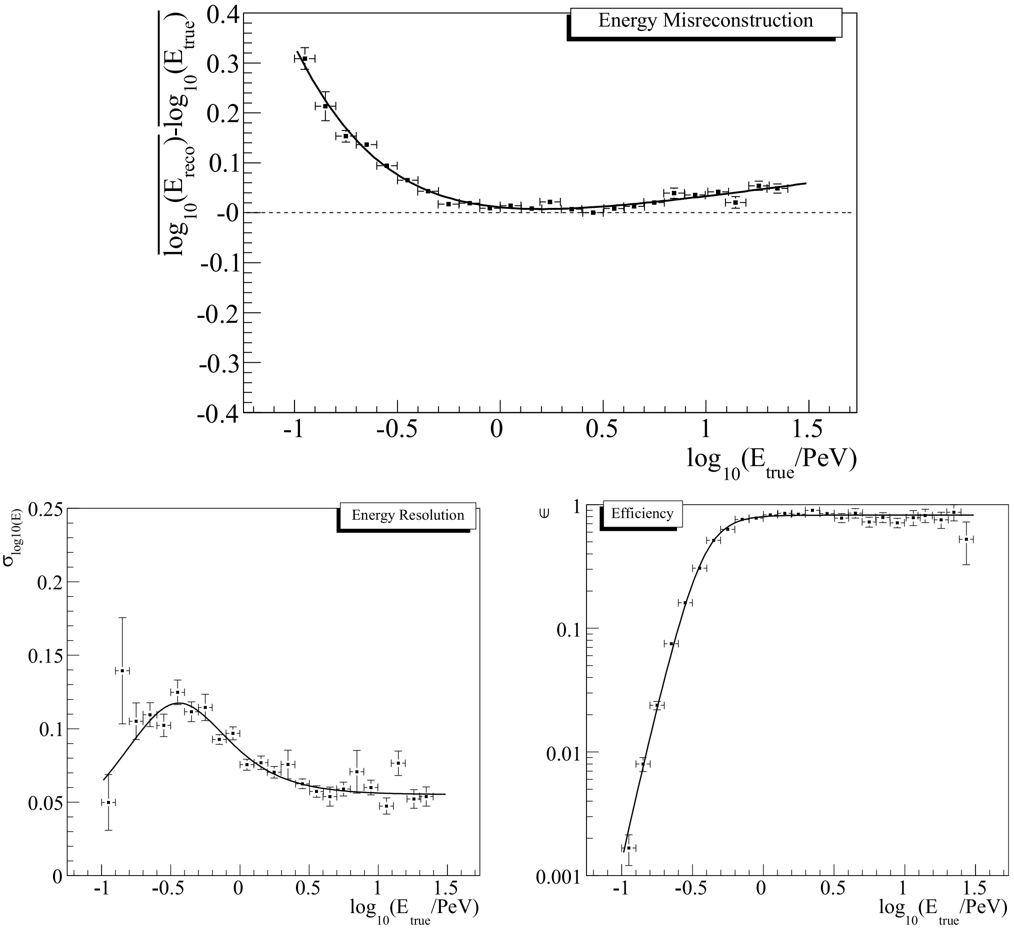

Figure 6.2: Energy dependence of the misreconstruction, resolution and efficiency for protons in the zenith range between 0 ° and 30 °. The functions shown are the parametrisations described in the text.

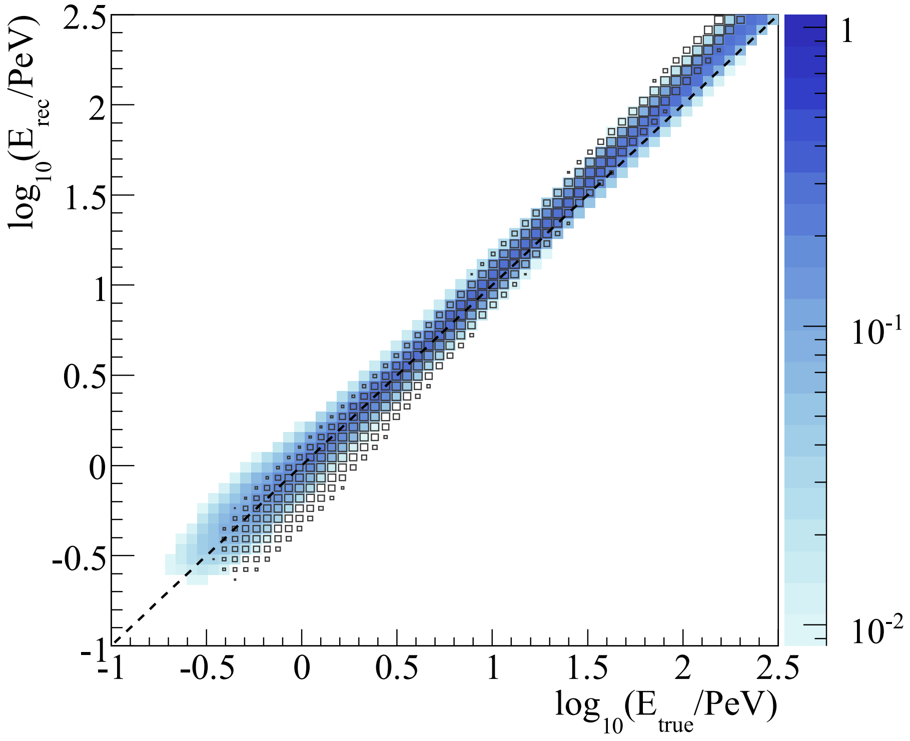

Figure 6.3: Graphical illustration of the response matrices of proton (blue) and iron showers (boxes). The colors and box sizes scale logarithmically to make the width of the response clearer.

6.3 Raw Energy Spectrum in Full Simulation, Toy Simulation and Data

The distribution of reconstructed energies after all cuts, but without acceptance correction or unfolding applied, will from now on be refered to as the *raw energy spectrum* $dI/d\log_{10}E^{\mathrm{rec}}$. In simulations, unfolding the raw spectrum should lead back to the true spectrum that was assumed in the first place. It can thus be used to verify the unfolding procedure. Besides that, if the raw spectra of data and simulation qualitatively agree, it demonstrates the understanding both of data and simulation to a certain extent and thus verifies the analysis.

In the case of IceTop, where composition, index and flux of the true spectrum can only be approximated since existing measurements have high systematic uncertainties, a comparison of simulated and measured raw spectrum cannot entirely verify either data or simulation. Even if they do agree, they could still be caused by different true fluxes. Nevertheless, the comparison of raw spectra gives an idea whether an unfolding is justifiable, and how big the dependency on the composition is. This will be shown in this section, after discussing how a true spectrum is actually applied on the simulation by weighting.

6.3.1 Definition of Raw Spectrum

The raw energy spectrum can be calculated bin by bin for intervals $(\Delta\log_{10}E)_i$ as the number of events in that bin per area A, time τ and solid angle Ω:

$$\left(\frac{dI}{d\log_{10}E^{\mathrm{rec}}}\right)_i = \frac{N_i^{\mathrm{rec}}}{(\Delta\log_{10}E)^{\mathrm{rec}}\,A^{\mathrm{cut}}\,\Omega^{\mathrm{cut}}\,\tau} \tag{6.9}$$

The mean cut area A^{cut} perpendicular to the direction of incidence for an observed zenith range $[\theta_1^{\mathrm{cut}}, \theta_2^{\mathrm{cut}}]$ can be calculated from the (horizontal) cut area in the detector plane $A_{\mathrm{d}}^{\mathrm{cut}}$ as $A^{\mathrm{cut}} = A_{\mathrm{d}}^{\mathrm{cut}} \cdot (\cos\theta_1^{\mathrm{cut}} + \cos\theta_2^{\mathrm{cut}})/2$. The solid angle for that zenith range is $\Omega^{\mathrm{cut}} = 2\pi\,(\cos^{\mathrm{cut}}\theta_1 - \cos^{\mathrm{cut}}\theta_2)$. The fact that the effective area might be smaller than the cut area, or in other words, that the efficiency is probably less than one, is not taken into account for the raw spectra since it is an issue that will be corrected in the unfolding.

6.3.2 Reweighting the Full Simulation

The events in CORSIKA are distributed over an area $A_{\mathrm{d}}^{\mathrm{gen}}$ in the detector plane and over zenith angles θ, azimuth angles ϕ and primary energies E

with a differential distribution

$$\left(\frac{d^6N}{dE\,dA_\mathrm{d}\,d\phi\,d\theta\,dt}\right)^\mathrm{gen} \sim \sin\theta\cos\theta\,E^{-1}. \tag{6.10}$$

The times of the events t are not assigned by CORSIKA, they are arbitrary at this point. Replacing A_d with the area perpendicular to the direction of incidence, $dA_\mathrm{d} = dA/\cos\theta$, and introducing the solid angle $d\Omega = \sin\theta\,d\theta\,d\phi$ and logarithmic energy scale $dE \sim E\,d\log_{10}E$, this becomes a flat, isotropic distribution:

$$\left(\frac{d^6N}{d\log_{10}E\,dA\,d\Omega\,dt}\right)^\mathrm{gen} \sim 1. \tag{6.11}$$

Consequently, to achieve the flux given by a certain model, this distribution has to be given a weight that only depends on the energy:

$$\left(\frac{d^6N}{d\log_{10}E\,dA\,d\Omega\,dt}\right)^\mathrm{mod} \equiv \frac{dI^\mathrm{mod}}{d\log_{10}E} = w(E)\cdot\left(\frac{d^6N}{d\log_{10}E\,dA\,d\Omega\,dt}\right)^\mathrm{gen} \tag{6.12}$$

For a simulation of N^gen events that are homogeneously distributed over an energy range $(\Delta\log_{10}E)^\mathrm{gen}$, a zenith range $[\theta_1^\mathrm{gen},\theta_2^\mathrm{gen}]$, a perpendicular area $A^\mathrm{gen} = A_\mathrm{d}^\mathrm{gen}\cdot(\cos\theta_1^\mathrm{gen}+\cos\theta_2^\mathrm{gen})/2$ and a solid angle $\Omega^\mathrm{gen} = 2\pi\,(\cos\theta_1^\mathrm{gen} - \cos\theta_2^\mathrm{gen})$, this weight is

$$w(E) = \frac{dI^\mathrm{mod}}{d\log_{10}E}\,\frac{(\Delta\log_{10}E)^\mathrm{gen}\,A^\mathrm{gen}\,\Omega^\mathrm{gen}\,\tau}{N^\mathrm{gen}}. \tag{6.13}$$

Here, everything but the first term is a constant scaling factor for that energy bin. If the constant factor in eq. 6.9, which leads to the raw spectrum, is regarded as an additional weight applied to the events, the total weight turns to

$$w_\mathrm{tot} = \frac{1}{N^\mathrm{gen}}\,\frac{(\Delta\log_{10}E)^\mathrm{gen}\,A^\mathrm{gen}\,\Omega^\mathrm{gen}}{(\Delta\log_{10}E)^\mathrm{rec}\,A^\mathrm{cut}\,\Omega^\mathrm{cut}}\,\frac{dI^\mathrm{mod}}{d\log_{10}E} \tag{6.14}$$

where the lifetime τ cancels out and the basic effect of the weighting is nicely recognisable — the events are normalised to one in the first term, and scaled up in the middle term to account for oversampled events that are outside the detection area, zenith or energy range. The final term defines the energy distribution.

6.3.3 Comparison of Raw Energy Spectra

Three types of raw energy spectra can be compared:

- **Full MC spectra**, produced with IceTray simulations (see sec. 4.1.1), reweighted with eq. 6.14. This has the worst statistics and is only available up to 30 PeV.
- **Folded spectra**, using the a spectrum assumption and multiplying a response matrix to it, without actually simulating single events. To make the distribution more realistic, a poissonian randomisation can be applied. This should be very similar to the MC spectra, but does not have the disadvantage of energy limitation and bad statistics, so it allows calculations in higher precision and can serve as a toy simulation of the spectrum.
- **Real spectra** from experimental data. These do not have to agree quantitatively with one of the above, but can still be compared to get a first impression where the data will be, relative to the models.

Figure 6.4 shows several raw spectra for the zenith bin $[0\,°, 30\,°]$, multiplied by by $E^{1.7}$. This should reveal the actual threshold functions because the expected flux below the knee has a power index of about 1.7 in logarithmic scale. The raw spectrum derived for the two-components model is very close to the poly-gonato spectrum and is omitted for visual clarity.

Comparing the spectra one can draw the following conclusions:

- Involving heavier nuclei leads to deviations, especially at energies below 3 PeV.
- The agreement between the full MC approach and the spectrum derived by folding is good. Only at low energies small differences can be seen. Differences can e.g. occur if some distributions do not entirely fullfill the gaussian assumption.
- The measured flux is at a lower absolute scale than all simulated distributions. Its slope roughly matches the one derived by a proton-only or poly-gonato assumption.
- The overall threshold seems to be lower in simulation than in data.

The last point is very important to notice since it limits the range that an unfolding (or other threshold corrections) can be trusted in.

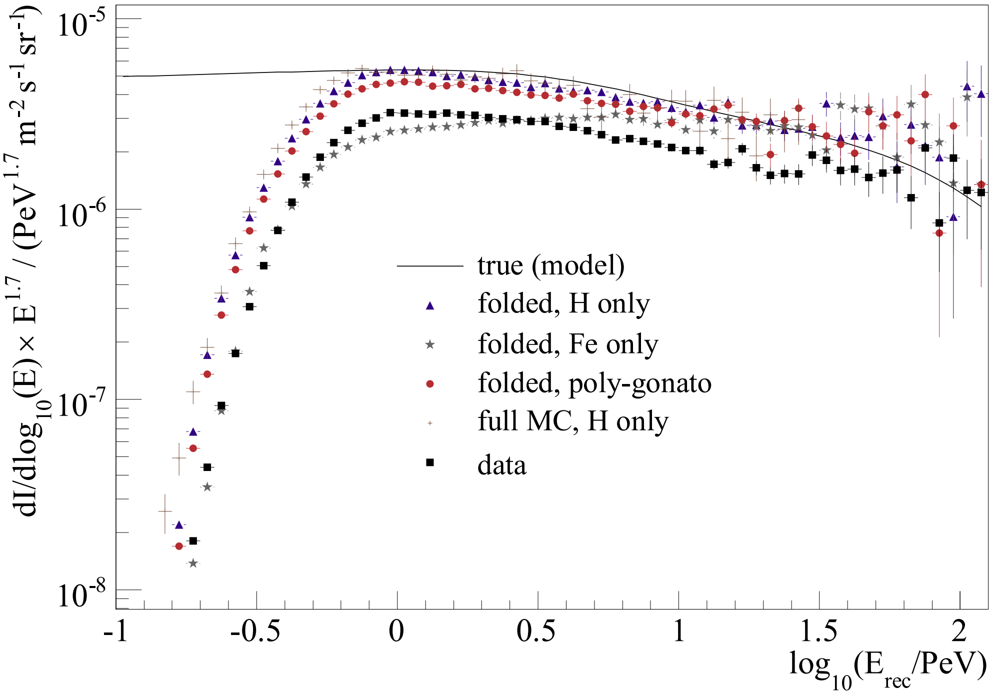

Figure 6.4: Raw spectra of showers $< 30^\circ$ derived with different composition assumptions in comparison with the true spectrum. The data is reconstructed under proton assumption. The impact of the composition is strongest in the PeV regime and becomes smaller for high energies.

6.3.4 Threshold in Simulation and Data

The trigger threshold, and thus also the reconstruction threshold, depends on several factors. The lateral spread of shower particles, and the fluctuations from that, define the number of stations that are potentially triggered by an event. The snow that piles up on top of the tanks attenuates or enhances the subcascades of the shower, and the optical processes in the tank influence the amount and concentration of light that reaches a PMT. The pulse forming in the PMT is comparably straight-forward, but yet after that, the voltage discriminator on the DOM board is a sensitive part to understand. This is because it is in principle sensitive to volage, but may still require a certain minimum charge even if the voltage threshold is reached.

If all these factors are treated well and realistically enough in a simulation, one can expect the threshold function to be in agreement with the one observed in experimental data, which makes it possible to correct the spectrum below the regime of full acceptance.

In IceTop simulation, as in other air shower experiments, neither the shower spread nor the snow, tank or electronics simulation can be regarded completely realistic and without possible uncertainties. Therefore it is not surprising to find a deviation in the threshold functions of simulation and data. In all zenith bins, and both proton and iron simulations, the threshold function goes to lower energies.

Some investigations have been undertaken to find the reason for this behaviour, yielding the insight that also the distribution of available pulses is different in simulation: The pulse threshold in data is steeper and at a higher value (fig. 6.5). This indicates that the source of the problem is not the shower or tank, but most probably the PMT or discriminator simulation.

Definition of full acceptance thresholds

For this thesis, the problem of simulation discrepancies in the threshold regime could not be solved, so a definition of the energy range to be trusted was to be established. The full (proton-only) simulated, and the polygonato folded raw spectrum, were compared to the measured spectrum in more detail. For this purpose, the data was renormalised to match the flux of the simulation in the range of full acceptance. As above, the bins were multiplied by $E^{1.7}$ to make it easier to identify the point where full acceptance is reached.

Figure 6.6 shows the definitions that were finally made for the raw spectra, based on where all three graphs approximately agree within statistical uncertainty.

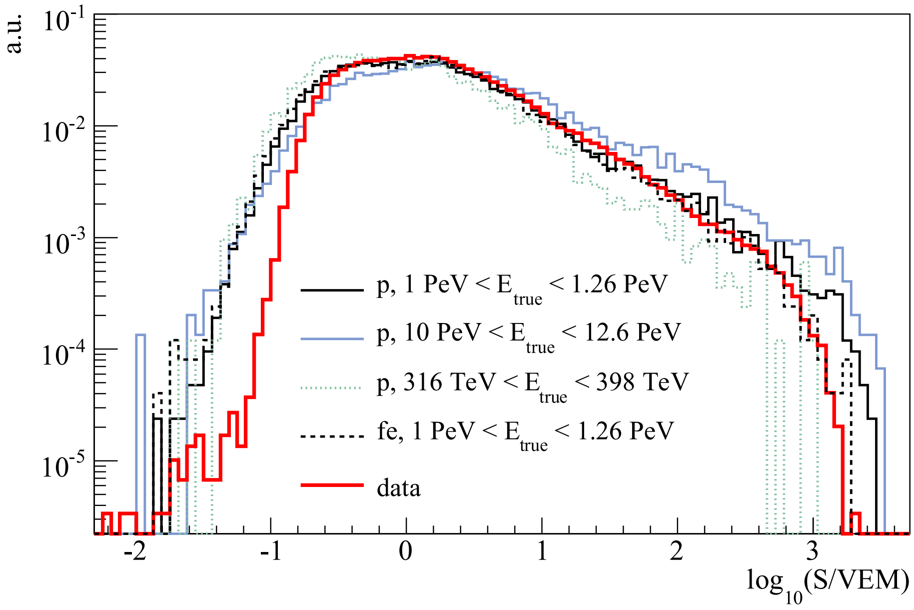

Figure 6.5: Pulse distribution in data and several simulated event groups. The threshold is too low in simulation, independent of the primary type or energy.

These values, however, cannot be applied directly on unfolded spectra since every bin in the raw spectrum has an impact on unfolded bins at slightly higher and lower energies, depending on the width of the response distribution. Defining the impact range as being 2σ of the response distribution at the threshold energy, the threshold definitions in tab. 6.2 could be gained.

Table 6.2: Threshold definitions for raw and unfolded energy spectra, derived as described in the text. All values are in $\log_{10}(E/1\,\mathrm{PeV})$.

zenith range	raw	unfolded
$0^\circ - 30^\circ$	-0.05	0.10
$30^\circ - 40^\circ$	0.30	0.50
$40^\circ - 46^\circ$	0.55	0.75

ZENITH BIN 0: $0^\circ < \theta < 30^\circ$

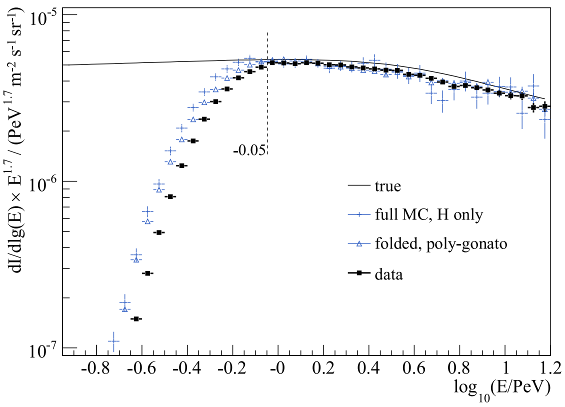

ZENITH BIN 1: $30^\circ < \theta < 40^\circ$

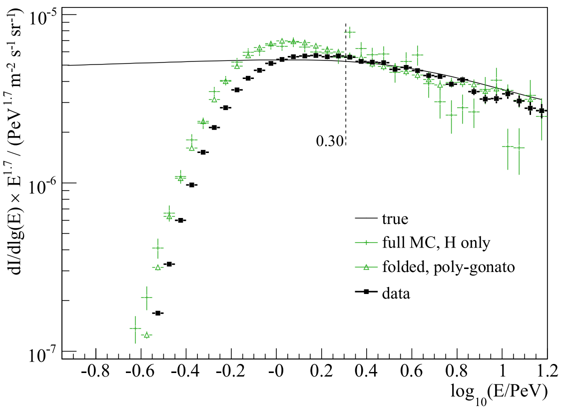

ZENITH BIN 2: $40^\circ < \theta < 46^\circ$

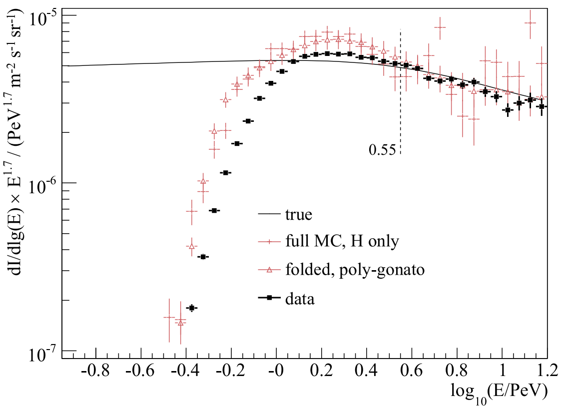

Figure 6.6: Definition of full acceptance ranges for all three investigated zenith bins. The data were renormalised so they match the flux of the simulation above threshold.

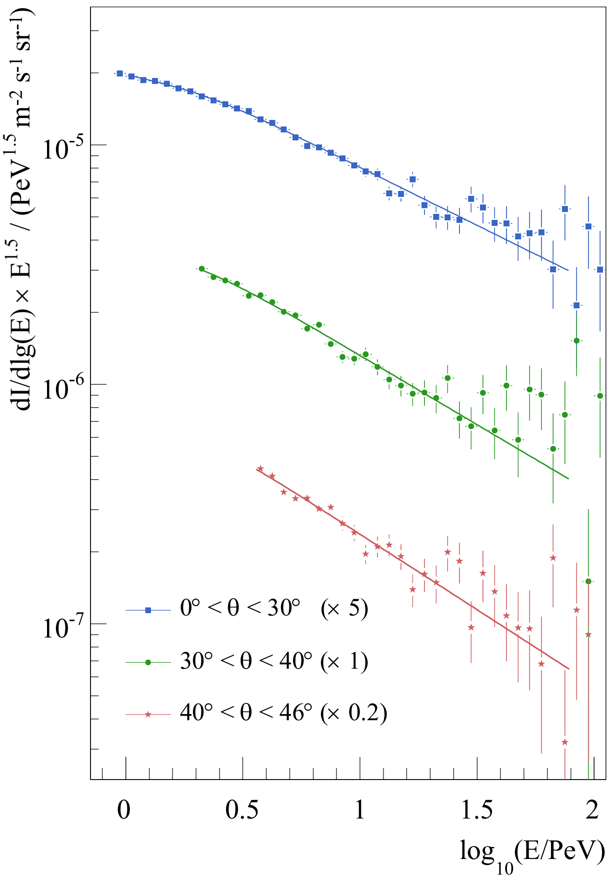

Figure 6.7: Raw energy spectra for three zenith bins in their range of full acceptance. The lines are the fits that were performed to estimate the power indices. The absolute fluxes are corrected for the efficiency (eq. 5.23).

6.3.5 Fits on the Raw Energy Spectrum

For discussion and comparison, the three raw spectra derived for the zenith bins were fitted with eq. 6.1 in the range of full acceptance. The knee position, along with the index below the knee and the ε parameter, were only fitted for the first zenith bin since the thresholds of the other bins are too high to be sensitive to these parameters. Figure 6.7 shows the results. Two spectra were multiplied by a factor of 5 and 0.2, respectively, to enhance visibility. For this investigation, the spectra were divided by the efficiency of the range of full acceptance (eq. 5.23). Table 6.3 summarises the found parameters. The spectra, and all involved event numbers per bin, are listed in detail in tab. A.2 in Appendix C.

The flux constants are statistically compatible within one standard de-

Table 6.3: Parameters of the raw spectra (see eq. 6.1). $I_{\mathrm{PeV,lg}}$ is given in terms of $10^{-6}\,\mathrm{m}^{-2}\,\mathrm{s}^{-1}\,\mathrm{sr}^{-1}$, E_{knee} in PeV. The flux constants are corrected for the efficiency (eq. 5.23).

zenith range	$I_{\mathrm{PeV,lg}}$	$-\gamma_1$	$-\gamma_2$	E_{knee}	ε	χ^2/ndf
$0° - 30°$	3.96(9)	2.68(9)	2.98(2)	2.0(5)	3.2(1.5)	30.1/34
$30° - 40°$	3.77(8)	–	3.079(14)	–	–	40.9/30
$40° - 46°$	3.68(8)	–	3.13(3)	–	–	27.3/25

viation, but the indices γ_2 are not. This indicates impact of the composition change — At high inclination, (old) showers of heavy nuclei appear smaller than proton showers, therefore the energy is underestimated and the slope of the spectrum is too steep.

Chapter 7

Unfolding

> *"Just 'cause you feel it doesn't mean it's there."*
>
> Radiohead,
> *There There*

After the response matrices are set up and verified, an unfolding of the data can be attempted. In general, unfolding is the inversion of eq. 6.2, which is well-defined mathematical task. However, the poissonian statistics of the measured spectrum $\vec{F}$ distorts the distribution. Strictly speaking, eq. 6.2 rather gives an expectation value of the effects F_i, and the actual measurement deviates randomly from that. This is a major problem, because an inverted response matrix per definition tries to find a cause for any measured event, and does not know which of the spectral features might be random and which are real. In practice, this leads to a resonating behavior in the unfolded spectrum that leads to usually much stronger features than the physical characteristics of the spectrum itsself.

It is for that reason that unfolding has become a very complex mathematical discipline, and many algorithms and regularisation methods have been developed for different applications, depending on the number of dimensions of a problem, and whether a problem is over- or underdefined. The problem of unfolding the energy spectrum is one dimensional, and can be made over-defined (less amounts of unfolded than raw bins), so it is comparably simple. Therefore, two relatively common algorithms were chosen that are both easy to implement and transparent in their performance.

7.1 Algorithms

Both algorithms used for this analysis follow an iterative approach. This means they do not try to really invert the response matrix, but provide rules to calculate a cause spectrum $\vec{C}^{k+1}$ that is closer to the real spectrum than a previously assumed spectrum $\vec{C}^k$. In this way, starting at a certain seed spectrum $\vec{C}^0$, the true spectrum is approached step by step. If the iteration is applied too often, though, the spectrum develops the same resonances one would get with matrix inversion, so for both algorithms it is important not to iterate too long.

7.1.1 Bayesian Unfolding

The bayesian unfolding used here is described in detail in [80]. Essentially, taking the efficiency

$$\varepsilon_j = \sum_i R_{ij} \tag{7.1}$$

and the *backfolded* spectrum of effects

$$\tilde{\vec{F}}^k = \mathbf{R}\,\vec{C}^k \tag{7.2}$$

of an assumed spectrum $\vec{C}^k$, the iteration rule can be expressed as

$$C_j^{k+1} = C_j^k \, \frac{\sum\limits_i \frac{F_i}{\tilde{F}_i} R_{ij}}{\varepsilon_j}. \tag{7.3}$$

The errors of the measured spectrum do not enter the calculation. The reference gives some advice on how to calculate the errors of the unfolded spectrum from the errors of the measured data, but it turned out to be numerically impossible to put into practice. Since, however, we have a relatively simple and almost diagonal matrix, methods will be discussed later to determine valid errors.

7.1.2 Gold Unfolding

The Gold algorithm used here is taken from [11], but was originally published in [81]. The basic iteration rule

$$C_j^{k+1} = C_j^k \frac{F_j}{\tilde{F}_j} \tag{7.4}$$

is even simpler than the above, and only works with square response matrices. However, there is a possibility to modify it for use with other matrices and to make use of the measurement errors $\vec{\sigma}$. With the following definitions

$$\begin{aligned} S_{ij} &= \delta_{ij}/\sigma_i, \\ \tilde{\mathbf{R}} &= \mathbf{S}\,\mathbf{R}, \\ \mathbf{R}_{\mathrm{mod}} &= \tilde{\mathbf{R}}^T\tilde{\mathbf{R}}, \\ \vec{F}_{\mathrm{mod}} &= \tilde{\mathbf{R}}^T\mathbf{S}\vec{F}, \end{aligned} \tag{7.5}$$

equation 6.2 turns to

$$\vec{F}_{\mathrm{mod}} = \mathbf{R_{mod}}\,\vec{C}. \tag{7.6}$$

This modified (square) response matrix and measurement vector can now be used to do the iteration. In principle, this modification should also be possible in the bayesian unfolding. Since this might violate its (bayesian) philosophy, and besides that it is of use to keep the two algorithms separate to see systematic differences, it was only applied with the Gold algorithm.

The error treatment for this algorithm is not documented in the reference, and will also be discussed in the following paragraph.

7.2 Uncertainties and Error Treatment

The determination of systematic and statistical errors of a spectrum after unfolding is not a trivial task. This is because the value of an unfolded bin is in principal derived from all other bins through a varying amount of iteration steps which can hardly be traced back with a regular error propagation. Also, the iterative methods chosen do not yield an approximate inverse matrix in the end, so the issue cannot be reduced to a single, linear error propagation step.

Several approximations of the statistical error propagation were tried out, for example by propagating the errors only through the last iteration step, or by deriving the error from the amount of events that an unfolded bin is equivalent to, making use of the constant efficiency at high energies. In addition to that, a bootstrap method [82] was tried out of randomly varying the data points within their error bands, performing an unfolding with each modified spectrum. Repeating this numerous times leads to a number of unfolded spectra whose spread gives an error for each unfolded bin as well.

A way to check these error estimation methods, and the unfolding algorithm itself, is to perform a toy simulation again. An assumed spectrum is multiplied (folded) by the detector response and a poissonian randomisation is applied on each bin. The derived spectrum is equivalent to a measured raw spectrum and can be unfolded, including the error estimation. If this is done N times with different random seeds, the following quantities can be calculated for each bin i:

1. Mean flux of the unfolded spectra $\bar{I}_i = \sum_{k=1}^{N} I_i^k / N$.
2. Ratio between mean unfolded and true (model) spectrum $\bar{I}_i / I_i^{\text{true}}$. This indicates the systematic uncertainty due to unfolding.
3. Standard deviation of unfolded spectra $\sigma_i = \sqrt{\sum_{k=1}^{N} (I_i^k - \bar{I}_i)^2 / (N-1)}$.
4. Mean error assigned to the bin by the chosen error estimation method $\overline{\sigma_i^{\text{ass}}} = \sqrt{\sum_{k=1}^{N} (\sigma_i^{\text{ass},k})^2 / N}$. This should be equal to σ_i if the error assignment is correct.

Of all methods that were tried out the bootstrap method was the only that led to $\overline{\sigma_i^{\text{ass}}} \approx \sigma$ within less than 5 % and independent of energy. Figure 7.1 shows an example study done with the bayesian algorithm, $N = 50$, the bootstrap error estimation and assuming an exposure similar to that in the analysed spectra. It shows that the bias on the errors is about 4 ± 2 %, which is acceptable. The only visible systematic shift is located in the lowest four bins, where the steep acceptance function and the cropped true spectrum might cause inconsistencies. Since these bins anyway are not regarded trustable in the final spectrum (see sec. 6.3.4), they can be neglected here. Then, the mean systematic shift of the unfolded flux bins is compatible with zero, but in any case less than ±0.6 %. Also, no energy dependent bias can be seen.

The same study was performed with the Gold algorithm and the response matrix of the zenith range [40 °, 46 °], leading to similarly consistent error assignment and a slightly higher upper limit of ±1.3 % for the systematic shift.

7.3 Iteration Depth

As mentioned above, iterative unfolding always approaches the real spectrum for several iteration steps, but in the long term diverges from that because the algorithm seeks to connect fluctuations of the data to events in the real spectrum. To investigate the iteration behaviour of an algorithm, two quantities are used to describe (a) the iteration depth and (b) the quality of the result.

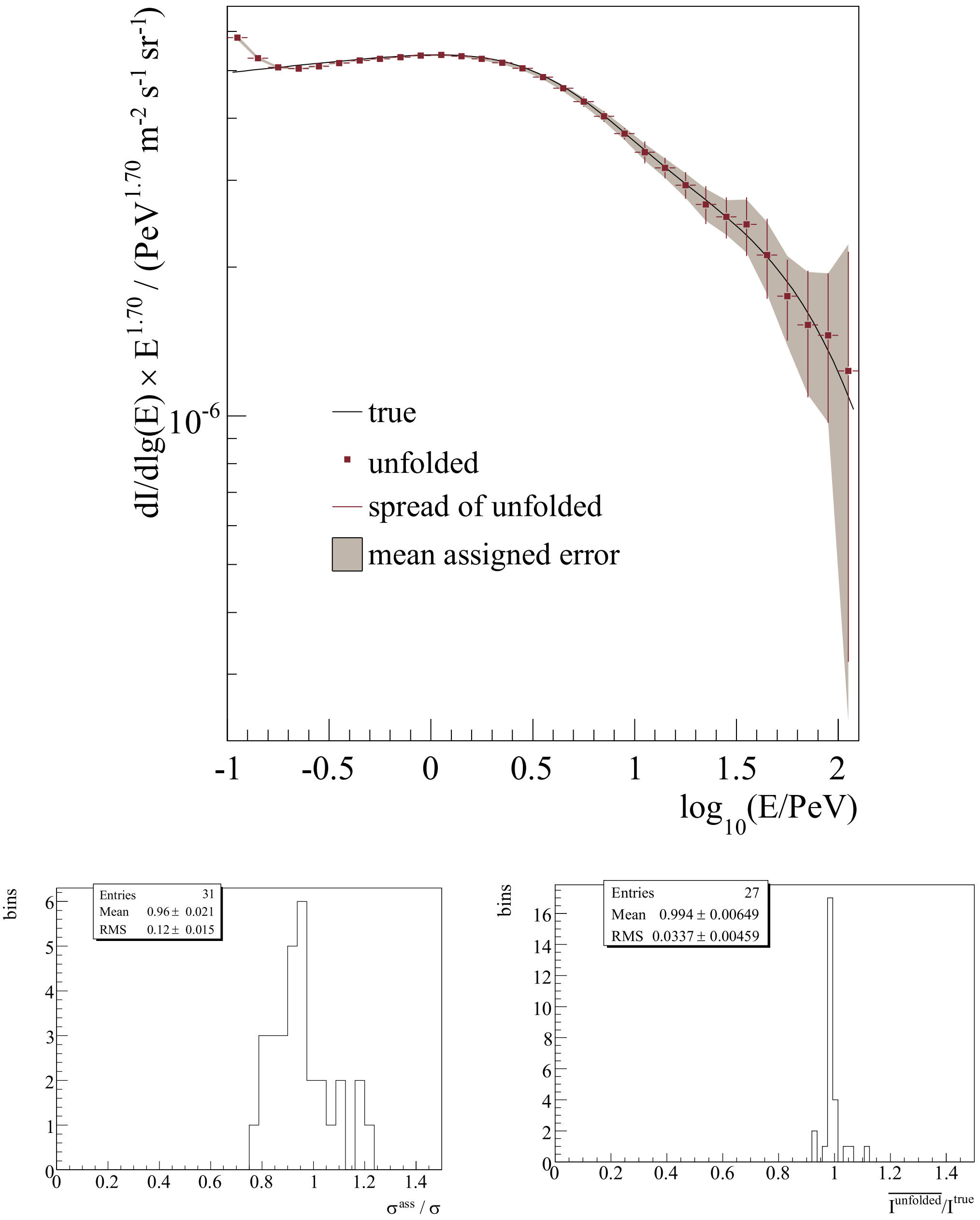

Figure 7.1: Quantitative characterisation of the bayesian unfolding algorithm, using the error assignment described in the text. 50 spectra were generated and unfolded, leading to good consistency between actual variation (shaded band) and mean assigned errors (error bars). The histograms at the bottom show distributions of error and absolute flux ratios of the bins in the upper plot. The error misassignment is about $4 \pm 2\,\%$, the systematic flux shift is $< 0.6\,\%$.

A value that gets minimised as the algorithm iterates is the difference between measured and backfolded spectrum (eq. 7.2), which can be quantified by a χ^2-like comparison:

$$\chi_k^2 = \chi^2(\vec{F}, \tilde{\vec{F}}^k) = \sum_j \frac{(F_i - \tilde{F}_i^k)^2}{\sigma_i^2} \tag{7.7}$$

However, which value it approaches is unknown, so a better value to describe the progress of unfolding is the relative decrease of that, $\Delta\chi^2_{k:k-1} = (\chi^2_{k-1} - \chi^2_k)/\chi^2_k$. This should always approach zero, so a fixed $\Delta\chi^2_{k:k-1}$ defines the depth of iteration independent of how close the backfolded spectrum gets to the measured data.

The quality of unfolding can be estimated by a comparison of the unfolded to the true spectrum, which is known in simulation:

$$\chi^2_{\mathrm{real},k} = \chi^2(\vec{C}, \vec{C}^k) \tag{7.8}$$

To optimise the iteration depth for a particular analysis, $\chi^2_{\mathrm{real},k}$ should only be calculated for the bins of interest. Consequently, only bins $0.0 < \log_{10} E^{\mathrm{true}} < 2.0$ are taken into account in the following.

Using $\chi^2_{\mathrm{real},k}$ and $\Delta\chi^2_{k:k-1}$, the iteration behaviour of the algorithms can be nicely quantified, as can be seen in fig. 7.2, where it is applied on toy-simulated raw spectra. All unfoldings converged with the expected behaviour of improvement followed by increasing deviation. Depending on which matrix is used, and what exposure is assumed, the minima of the curves for both algorithms are between 0.4 and 4. The average in log-scale, 1.3, is in the following taken as the optimal depth, and the extrema 0.4 and 4 are used for systematic error determination.

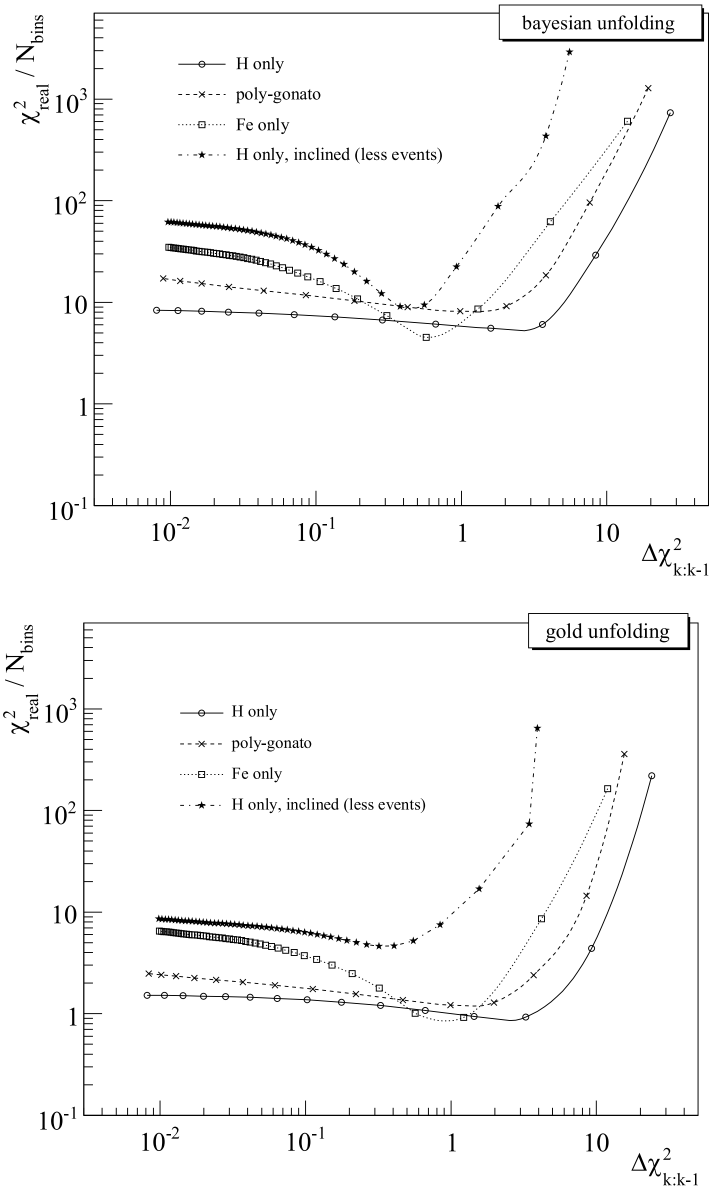

Figure 7.2: Iteration behaviour of the Gold and the bayesian algorithm with different matrices and a low exposure assumption for one of them. The horizontal axis quantifies the iteration depth, the vertical axis the χ^2 to the real spectrum. All deconvolutions show a minimum which corresponds to the ideal iteration depth. The errors used in the χ^2_{real} calculation are approximations calculated between the iterations, thus the absolute values of χ^2_{real} do not have a strict statistical interpretation.

Chapter 8

Energy Spectrum

> *"When one admits that nothing is certain one must, I think, also admit that some things are much more nearly certain than others."*
>
> Bertrand Russel,
> *Am I An Atheist Or An Agnostic?*

In this final analysis chapter the used data samples are documented and their exposures and effective thresholds are calculated. Then all systematic uncertainties are discussed and the final unfolding is applied. The results are interpreted and compared to spectra from other experiments.

8.1 Data Samples

The data used is all data from August 2007 that was made available from South Pole via satellite transfer. The data are subdivided into the three zenith ranges introduced in sec. 5.6. Since each of them defines a certain solid angle range above the detector, they will from now on be refered to as $\Omega_0 = [0\,°, 30\,°]$, $\Omega_1 = [30\,°, 40\,°]$ and $\Omega_2 = [40\,°, 46\,°]$. As mentioned in sec. 3.4, the satellite transmitted data comprises events that were triggered by the SMT (≥ 6 DOMs ≈ 3 stations), prescaled by a factor of 5, and events that fulfilled the SMT_Large condition (≥ 16 DOMs ≈ 8 stations) and were not prescaled. The SMT_Large sample has better statistical quality, but a higher trigger threshold. A comparison of measured distributions showed that, in terms of $\log_{10} E$, the SMT_Large sample can be used for bins above

0.1 for $\Omega_{0,1}$ and above 0.25 for Ω_2. Given the full acceptance thresholds defined in tab. 6.2, this means that data taken with the regular SMT is only relevant in Ω_0 between -0.05 and 0.1. This is because 5 stations are required for reconstruction, which discards a big part of SMT data and reduce the difference between the SMT and SMT_Large data samples.

Life Time, Exposure and Effective Thresholds

The lifetime of the detector in August 2007 was $2.30 \cdot 10^6\,\mathrm{s}$. For the SMT data, this time effectively has to be divided by the prescale factor 5. With the full effective areas presented in eq. 5.22 and the solid angles Ω_i, the exposure of the data sets can be calculated:

$$\xi_i = \tau\,\Omega_i\,A_i^{\mathrm{eff}} \tag{8.1}$$

Using an approximated energy spectrum as it is known from other experiments, and the number of detected showers N_i in Ω_i, an effective reconstruction threshold $E_{\mathrm{thr}}^{\mathrm{eff}}$ can be estimated. It is defined as the value above which the number of measured events could be expected if the acceptance function followed a step function:

$$N_i = \xi_i \int_{E_{\mathrm{thr}}^{\mathrm{eff}}}^{\infty} \left(\frac{dI}{dE}\right) dE \tag{8.2}$$

With a simplified spectrum consisting of two power laws with indices $\gamma_1 = -2.71$ and $\gamma_2 = -3.11$, a sharp knee at $E_{\mathrm{k}} = 3.1\,\mathrm{PeV}$ and the flux of $I_{\mathrm{PeV,lg}} = 4.05 \cdot 10^{-6}\,\mathrm{m}^{-2}\,\mathrm{s}^{-1}\,\mathrm{sr}^{-1}$, as will be determined and discussed later, the effective threshold can be calculated by

$$\begin{aligned} E_{\mathrm{thr}}^{\mathrm{eff}} / \,\mathrm{PeV} &= \left[\left(\frac{N_i \ln 10}{\xi_i I_{\mathrm{PeV,lg}}} + \left(\frac{E_{\mathrm{k}}}{1\,\mathrm{PeV}}\right)^{\gamma_1+1}\left(\frac{1}{\gamma_1+1} - \frac{1}{\gamma_2+1}\right)\right)\cdot(\gamma_1+1)\right]^{\frac{1}{\gamma_1+1}} \\ &= \left[\frac{N_i}{\xi_i}\cdot 9.72\cdot 10^5\,\mathrm{m}^2\,\mathrm{s}\,\mathrm{sr} + 0.065\right]^{-0.585} \end{aligned} \tag{8.3}$$

The systematic uncertainty in this threshold estimator is the same as the uncertainty on the absolute energy scale discussed later, i.e. about 10 %.

Table 8.1 shows the recorded events, exposures and effective thresholds of all Ω_i and both trigger modes. The errors on ξ are derived from the uncertainty of the effective areas, which are by far dominant over the others. As can be expected (for both trigger modes), the threshold increases significantly with higher inclination.

Table 8.1: Event numbers N, exposures ξ and effective thresholds of the data samples used for the analysis. ξ is given in units of $10^{11}\,\mathrm{m}^2\,\mathrm{s}\,\mathrm{sr}$, $E_{\mathrm{thr}}^{\mathrm{eff}}$ in PeV. The meaning of the SMT and SMT_L(arge) trigger modes and theta bins Ω_i is described in the text.

	Ω_0		Ω_1		Ω_2	
	SMT	SMT_L	SMT	SMT_L	SMT	SMT_L
N	148763	450006	64509	206512	23499	78464
ξ	0.362(6)	1.81(3)	0.246(6)	1.23(3)	0.164(6)	0.82(3)
$E_{\mathrm{thr}}^{\mathrm{eff}}$	0.441(9)	0.588(11)	0.570(16)	0.73(2)	0.80(3)	1.00(4)

8.2 Systematic Effects and Uncertainties

There are several systematic uncertainties involved in this analysis, some of which might be eliminated in future, some are connected to the detector principle or hardware limitations and will probably remain. The following paragraphs will discuss them, their impact on the energy spectra and probable ways to overcome them in future.

All uncertainties effectively appear in $\log_{10} E$ or $\log_{10}(dI/d\log_{10} E)$. Therefore all values below are given as errors on that, i.e. $\sigma \equiv \sigma_{\log_{10} E}$. Because of the power law correlation, energy and flux uncertainties can be converted for comparison:

$$\begin{aligned} \sigma_I &= \frac{\partial}{\partial \log_{10} E} \left(\log_{10} \frac{dI}{d\log_{10} E} \right) \sigma_E \\ &= \frac{\partial}{\partial \log_{10} E} \left(\log_{10} k + (-\gamma + 1) \log_{10} E \right) \sigma_E \\ &= (-\gamma + 1)\, \sigma_E \\ &= 1.7 \ldots 2.0 \cdot \sigma_E \end{aligned} \tag{8.4}$$

Here, k is a flux constant that cancels out and $\sigma_{\mathrm{lg\,E}}$ and $\sigma_{\mathrm{lg\,I}}$ are the errors on $\log_{10} E$ and $\log_{10}(dI/d\log_{10} E)$, respectively. In the few cases this conversion is applied, it is done with a γ that avoids underestimation of the error.

8.2.1 Inconsistencies between Data and Simulation

Most of the systematic problems involved with the reconstruction algorithms occur both in the treatment of experimental data and simulations. By the usage of the response matrix, they are corrected for and do not lead to any effect in the unfolded spectrum.

In particular, biases caused by the choice of lateral distribution function, or tendencies of the fit variables not caused by the shifted threshold function of the DOMs, such as the uneven core distribution, can be expected to be reproduced in simulation. Also biases introduced by the cuts and effects from zenith migration should cancel out.

The main issues that can be considered as causing a difference between data and simulation are the observed inconsistency of discriminator behaviour, the lack of snow at the outside walls of the tanks and the lack of simulations at high energies, where PMT saturation effects might gain significance.

Threshold Inconsistency

The underlying assumption of the silent likelihood (eq. 5.5) is that the discriminator threshold follows a step function in dependence of pulse charge. The actual pulse spectra, however, are no step functions. Presently, it is unclear how to define the location of the step S_{thr} under these conditions, and it is set to a value of 0.17 VEM. This is derived from calibration measurements, assuming the average muon calibration constant of 181 PE/VEM [60]. In addition, the tank correlation factor C_t in eq. 5.5 is unknown and assumed to be 0.

Both of these problems would not be severe if the discriminator behaviour was reproduced in simulations. However, as shown in fig. 6.5, the found charge threshold functions after LC was required do not agree between simulations and data.

To estimate the impact of this difference, the pulse threshold in simulations was reset by simply omitting all pulses below a given modified threshold. Two thresholds were tried out, namely $S_{\mathrm{thr}} = 0.13\,\mathrm{VEM}$ and $0.17\,\mathrm{VEM}$. This corresponds to a difference of $\Delta \log_{10} S_{\mathrm{thr}} = +0.117$. As can be seen in fig. 8.1, this leads to an overall increase of assigned energy of about $\Delta \log_{10} E = +0.016$. As a first-order approximation, the energy misreconstruction due to a threshold that is misplaced from the simulated threshold by $\sigma_{\mathrm{S_{thr}}} = \log_{10}(S_{\mathrm{thr,real}}/S_{\mathrm{thr,MC}})$ can be estimated as

$$\frac{\partial \log_{10} E}{\partial \log_{10} S_{\mathrm{thr}}} \approx \frac{\Delta \log_{10} E}{\Delta \log_{10} S_{\mathrm{thr}}} = +0.14. \tag{8.5}$$

From fig. 6.5, the actual $\Delta \log_{10} S_{\mathrm{thr}}$ can be extracted to be between +0.1 and +0.2, depending on where the curves are compared. This leads to a systematic shift due to the threshold simulation inconsistencies of

$$\Delta \log_{10} E = +0.014 \ldots 0.028. \tag{8.6}$$

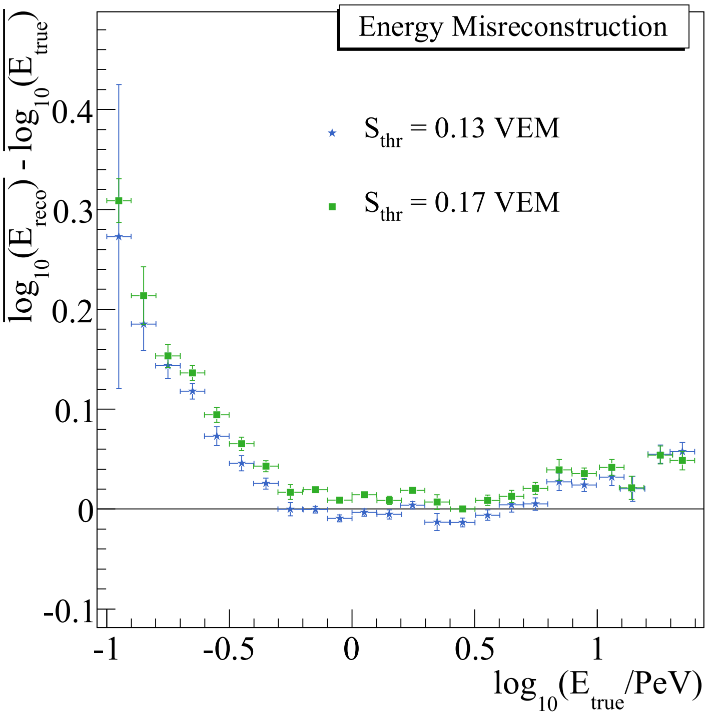

Figure 8.1: Energy assignment of proton showers with $\theta < 30^\circ$ under two different threshold assumptions. The threshold value assumption of the likelihood was kept constant to see only the effect of a wrong threshold simulation.

Since it is clear that this shift will be there, one can apply a correction of $\Delta \log_{10} E = +0.021$ to the unfolded spectrum, and the remaining uncertainty is

$$\sigma_{\mathrm{thr}} = \pm 0.007. \tag{8.7}$$

In future, this inconsistency might be solved by an improvement in the discriminator simulation or, if this is the problem, a more precise generation of PMT pulse shapes. If it remains impossible to reproduce the threshold functions, an alternative could be to apply a software trigger both on data and on simulation. This would equalise the two samples and simplify the definition of the silent likelihood. However, it has the disadvantage that it has to be done at least at a level of 0.5 VEM, so it raises the reconstruction threshold of the array by approximately a factor of three. On the other hand, an acceptance correction may then be trustworthy to do, which might give back the sensitivity at low energies.

Lack of Snow

The highest shower inclination accepted in this analysis is 46 °. For these showers, roughly 35 % of all recorded particles reach the tanks through an outside wall, passing through 65 cm of snow on average. Assuming a snow density of $\rho_{\text{snow}} \approx 0.3 \cdot \rho_{\text{water}} = 0.3\,\text{g/cm}^3$, this effectively corresponds[1] to a prolongation of the atmosphere by $X_{\text{snow}} \approx 6.5\,\text{g/cm}^2$. It is thus in the same order as the daily pressure fluctuations discussed below and can be expected to lead to an effect in the order of

$$\sigma_{\text{snow},\Omega 2} \approx \pm 0.017. \tag{8.8}$$

The equivalent maximal uncertainty values for the less inclined zenith bins are

$$\begin{aligned} \sigma_{\text{snow},\Omega 0} &\approx \pm 0.009 \\ \sigma_{\text{snow},\Omega 1} &\approx \pm 0.014. \end{aligned} \tag{8.9}$$

PMT Saturation

The PMT simulation also includes saturation effects. From the pulse distibution (fig. 6.5), no obvious problems of that simulation could be found. In both simulation and data the highest available pulses are at around 2500 VEM. Therefore, saturation effects should be reproduced well within the energy range that could be covered by shower simulation (up to 30 PeV). However, at higher energies the impact of saturation may increase in a way that is not described by plain extrapolation of the found response parametrisations. To study that, the value of saturation was artificially lowered by a factor of 10. Crudely, this can be expected to bring down the effects of saturation to 1/10 of the energies where they actually occur.

Figure 8.2 shows the relative change of energy assignment with the lowered saturation level. A deviation starts at around 1 PeV and reaches −0.04 at 10 PeV. With the real saturation level, these energies correspond to 10 PeV and 100 PeV, respectively. However, since simulations are available up to 30 PeV, the uncorrected deviation that can be expected is only −0.02. How well this is covered by the extrapolation, and in which direction the deviations from that can be expected, is unknown. Therefore an energy dependent systematic uncertainty towards higher energies, starting at 30 PeV

---

[1] Neglecting the assumably small transition effect between air and water, which might cause further complication.

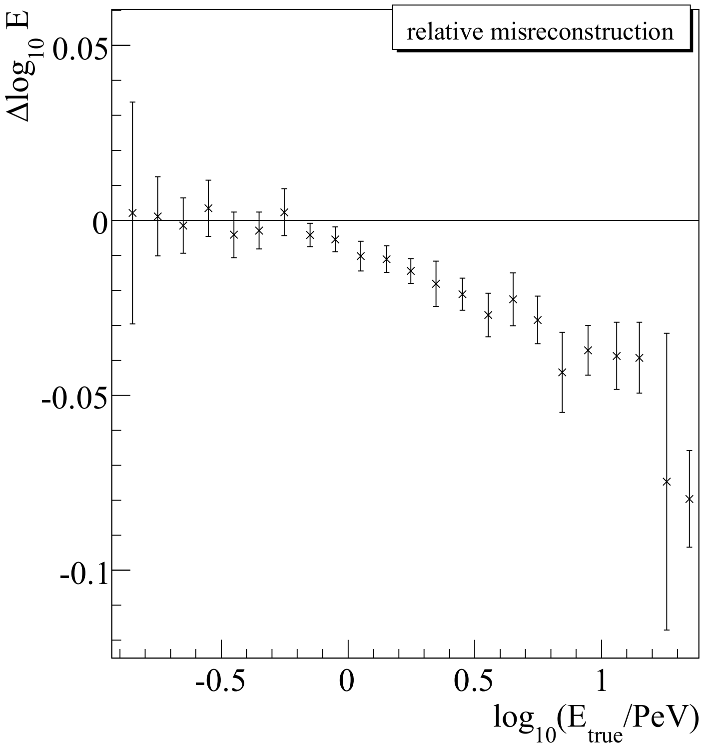

Figure 8.2: Misreconstruction of energies of proton showers with $\theta < 30\,^\circ$ and reduced PMT saturation level, relative to the response with regular saturation. The deviations that start at 1 PeV can be expected at around 10 PeV with the regular saturation (see text for further explanation).

and linearly increasing to

$$\sigma_{\mathrm{sat}} \approx \pm 0.02 \tag{8.10}$$

at around 100 PeV, which is the maximal analysed energy in this analysis, has to be assumed.

In 2008, the gain setting of the LG DOMs was lowered to encounter that problem, so this uncertainty should be better in future. Also, ways and time to generate higher energetic showers will be available soon.

8.2.2 Atmospheric Variations and Time Stability

The atmosphere above the IceTop detector is used as a converter material for the primary PeV cosmic rays. Its absolute thickness, in terms of atmospheric depth, varies over the year and also on a daily basis. Furthermore, but probably of less impact, its density profile changes with time. This influences the event rate and the shower sizes on ground level.

Atmospheric Model

All CORSIKA shower simulations that were generated for the presented analyses use the same atmospheric parameters. They are extracted from a December atmosphere calculated with the MSIS-90 code [52]. As mentioned in sec. 1.5.3, this assumably delivers a good parametrisation of the atmosphere above $10-20\,\mathrm{km}$, but is not particularly good to model the tropospheric layer. Besides that, the data used for this analysis were taken in August which might make a difference since at South Pole this is short after sunrise when the air is colder yet than in December, when temperatures have increased.

A comparison of the seasonal variation of ground pressures of the four available MSIS-90 atmospheres and mean measured data at South Pole [83] furthermore reveals no close correlation, which casts doubt about their general ability of tracing these variations properly. Two atmospheres parametrised by P. Lipari [50] seem to be more consistent in that point since they were extracted from profiles recorded in balloon measurements. However, they might have higher uncertainty at high altitudes.

The mean systematic uncertainty of the data sample was studied by simulating data samples of the Ω_0 bin for two different additional atmospheres. One is extracted with the MSIS-90 code for july. The other one is an August atmosphere after P. Lipari.

Figure 8.3 shows a comparison of the energy misreconstructions for the three models as a function of energy. The two alternative atmospheres lead to a visible change in the energy assignment that is approximately constant above threshold. Assuming complete ignorance about which of the atmospheres is realistic, the mean systematic uncertainty to be taken from the energy bins in the plot is

$$\sigma_{\mathrm{atm}} = \pm 0.014. \tag{8.11}$$

Daily Variations

Figure 8.4 shows the event rate relative to its mean value for all data used in the analysis. There are several significant deviations from the mean, most of which seem to follow an underlying time development and can be assumed to be caused by atmospheric variations. However, also detector instabilities might be involved, so the error that can be derived from the histogram inlet in the figure has to be refered to as the overall error due to time instabilities. For the histogram, all entries were weighted by the inverse of their statistical error. The derived relative error of the flux is

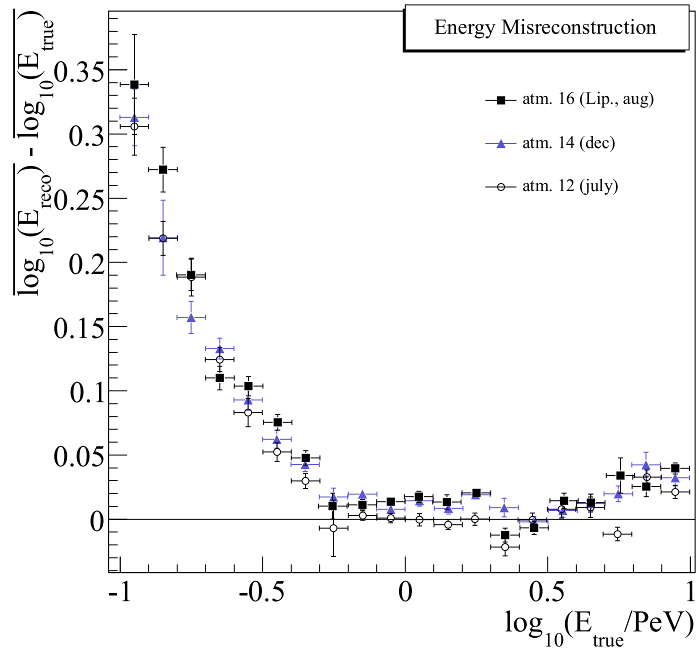

Figure 8.3: Energy assignment of proton showers with $\theta < 30^\circ$ under different atmospheric model assumptions. Compared to the detector resolution of 0.05, the variations are small, but significant.

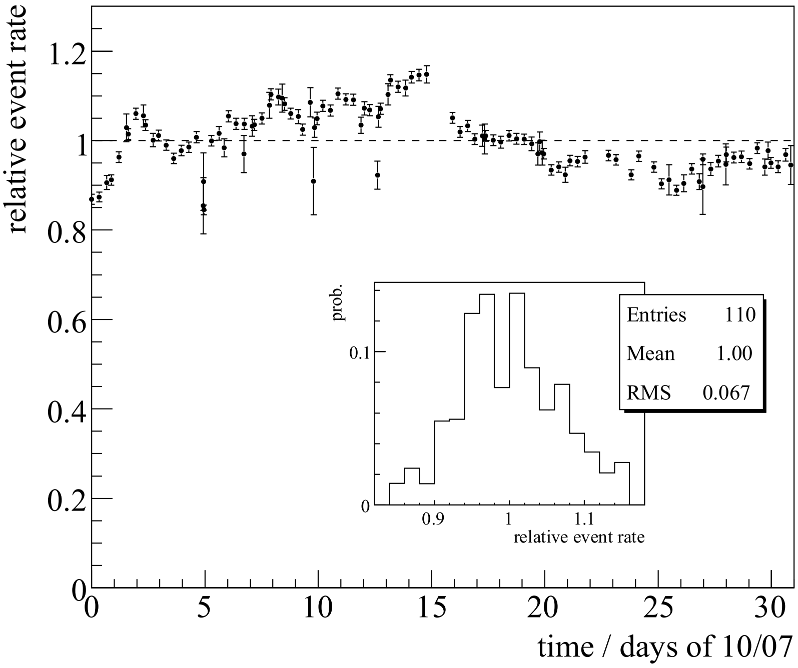

Figure 8.4: Time variation of relative event rates of the data sample used in the analysis. There are no probematic oddities, but significant increases and decreases as a function of time. The inlet is a histogram of all points in the graph, each of them weighted by the inverse of its error.

± 0.067, which equals an error on $\log_{10}(dI/d\log_{10} E)$ of 0.029. This flux variation, however, is caused by modified shower sizes at ground level and thus a different true energy threshold. That means that the error actually appears in $\log_{10} E$ rather than in flux. With eq. 8.4, the equivalent error in the logarithm of the energy is

$$\sigma_{\text{instab}} = \pm 0.017. \tag{8.12}$$

8.2.3 Interaction Models

The biggest uncertainty in the physics of the shower simulation lies in the hadronic interaction models at high energies. To estimate how big the influence of that on the energy assignment is, a sample of proton showers in the Ω_0 bin was simulated using the QGSJet03.c [47] code instead of SIBYLL2.1. Figure 8.5 shows a comparison of the found mean misreconstructions. No significant difference may be found. The simulated data sample sets an

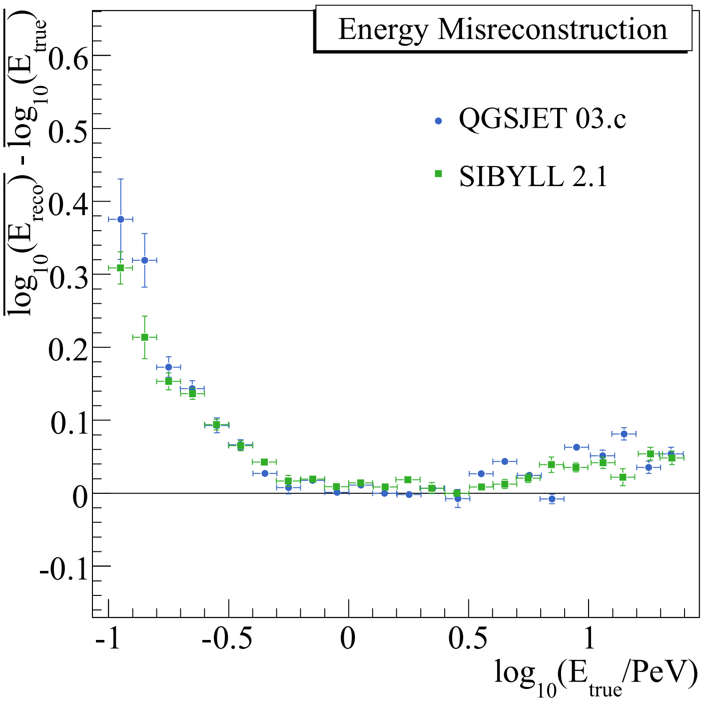

Figure 8.5: Energy assignment of proton showers with $\theta < 30^\circ$ with two different high energy hadronic interaction models. No significant tendency could be found.

upper limit on the systematic uncertainty due to interaction models of

$$\sigma_{\text{int}} \leq \pm 0.004. \tag{8.13}$$

However, since both models could be biased in the same direction, the actual uncertainty due to interaction models is in general unknown. For example, if one of the exotic explanations of the knee was true and undetected particles were produced at high energies (see sec. 1.4), the energy assignment becomes meaningless. For now, the small difference between the tested models is taken as an indication that the shower sizes measured by IceTop are not very sensitive to the interaction models.

An explanation for that could be the fact that the interaction models mainly influence the shower development, and not the maximal shower size. Since IceTop is located close to the maximum of the showers, the effect of the models may be less prominent than in other experiments

8.2.4 Calibration

All analysed data was calibrated using the muon calibration method introduced in sec. 3.3. The calibration constants are used in the simulation to estimate the charges in PE that arriving particles can be expected to produce. This makes the reconstructions practically insensitive to all calibration errors below the level of muon calibrations, such as the one of the ATWD bins or the PE calibrations of the PMT.

The dominant errors connected to the muon calibrations can be estimated as coming from three sources [84]:

1. The charge spectra of calibration runs are fitted by a function that parametrises the electromagnetic background and the muonic part of the distribution. One of its parameters is the calibration constant (in PE/VEM). Several functions were tried out [60], yielding calibration constants systematically differing by $\sim 5\,\%$.

2. The charge spectra in existing `tanktop` simulations of low-energetic showers are in disagreement with data in the order of $\sim 5\,\%$. This estimates the limit of general understanding of the method, such as the ratio of muons to electromagnetic particles in the "muon peak" of the calibration spectra.

3. The calibration runs are only done on a weekly basis. In between, the calibration constants can change by several percent. This, however, can be assumed to average out between the 52 tanks of the 2007 array, so it does not need to be taken into account here.

The relative systematic error of the calibration constant adds up to 0.07. This directly propagates to the estimation of the shower sizes and thus the primary energies. The error on $\log_{10} E$ is therefore

$$\sigma_{\mathrm{cal}} = \pm 0.03. \tag{8.14}$$

8.2.5 Unfolding Algorithm

There are three ways to get estimators for the systematic uncertainty involved with the unfolding. First, the results derived from the two unfolding algorithms can be compared. This is sensitive to principle problems intrinsic to the unfolding methods. Secondly, varying the iteration depth probes the stability of the result. The third approach was already shown in sec. 7.2, where folding a true spectrum led to randomised raw spectra, which can be used to generate a randomised sample of unfolded spectra. The difference between the mean of these unfolded spectra and the true spectrum gives another estimation of the systematic error.

All methods are based on the comparison of energy spectra. The strategy to derive a systematic error from two spectra $\vec{A}$ and $\vec{B}$ is to first calculate the logarithmic difference $\Delta \log_{10}(dI/d \log_{10} E)_i = \log_{10}(A_i/B_i)$ for each bin. With that, the mean of these differences is calculated, using the inverse errors as weights. If this mean deviates from zero, it is a systematic bias of the whole spectrum. If not, the error of the mean can serve as an upper limit on the uncertainty.

Difference Between the Algorithms

For all composition assumptions, an unfolding was performed with both the Gold and the bayesian algorithm. Figure 8.6 shows an example analysis done with a spectrum of zenith bin Ω_0 and poly-gonato assumption. The systematic difference in logarithm of flux in that case is 0.0018(3). With different response matrices and zenith bins, this value varies randomly, but its absolute value never gets beyond

$$\sigma_{\text{alg}} = \pm 0.006, \tag{8.15}$$

which can thus be regarded as the uncertainty in the logarithm of flux due to the unfolding algorithm.

Iteration Depth

In sec. 7.3, $\Delta\chi^2_{k:k-1} = 1.3$ was defined as the iteration depth of choice for the unfolding procedure. The range in which all points of maximal convergence lie was found to be 0.4 . . . 4.0. Therefore, a comparison of two deconvolutions that were interrupted at 0.4 and 4.0 can deliver the error that can be expected if 1.3 was not the ideal point of convergence for the spectrum investigated.

Figure 8.7 shows the same example unfolding as in the previous paragraph, tested for different iteration depths and using the bayesian unfolding. The systematic shift in logarithm of flux to be taken from this histogram is −0.00290(15). The deviations that could be found for other zenith ranges and response matrices again vary randomly, but always stay below

$$\sigma_{\text{iter}} = \pm 0.013. \tag{8.16}$$

which is the uncertainty in the logarithm of flux due to the iteration depth chosen.

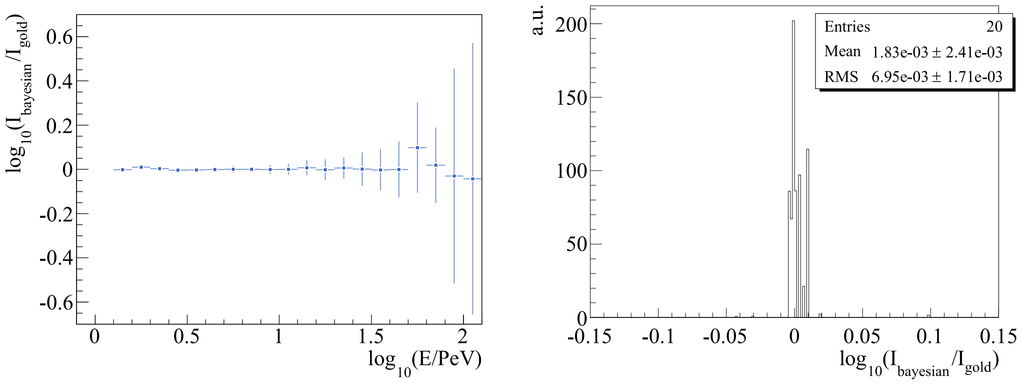

Figure 8.6: Comparison of spectra unfolded with Gold and bayesian unfolding. The raw spectrum from zenith bin Ω_0 was used assuming poly-gonato composition. The left plot shows the logarithmic flux differences of all valid bins. The right plot is a histogram of these points, weighted by $1/\sigma_i$. The mean of that is the systematic difference between the two spectra.

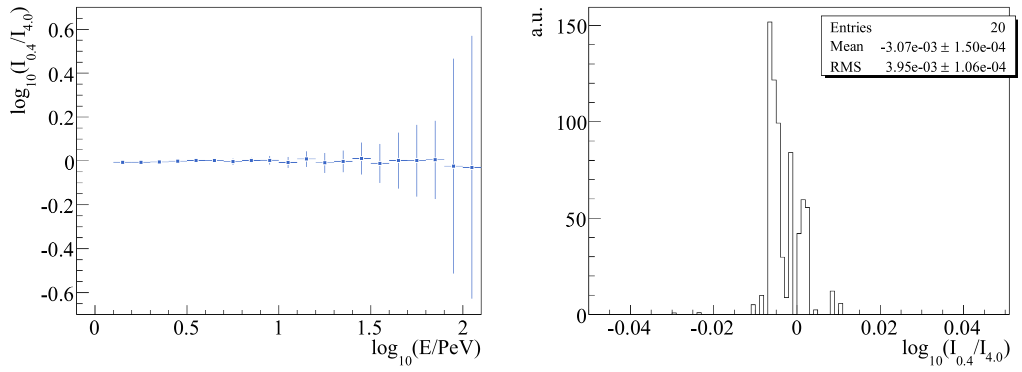

Figure 8.7: Comparison of spectra unfolded with two different iteration depth settings. The raw spectrum from zenith bin Ω_0 was unfolded with the bayesian algorithm, assuming poly-gonato composition. The left plot shows the logarithmic flux differences of all valid bins. The right plot is a histogram of these points, weighted by $1/\sigma_i$. The mean of that is the systematic difference between the two spectra.

Toy Simulation

The toy simulation introduced in sec. 7.2 indicated an upper limit for the systematic uncertainty of the flux of about 1.3 %. This is equivalent to a logarithmic error of

$$\sigma_{\mathrm{toysim}} = \pm 0.005. \tag{8.17}$$

Although this should be bigger than the above, it is smaller, but still in the same order of magnitude.

The total uncertainty caused by the unfolding procedure, to be on the safe side, is assumed to be the sum of σ_{alg} and σ_{iter}. It is

$$\sigma_{\mathrm{unf}} = \pm 0.014 \tag{8.18}$$

in logarithm of flux.

8.2.6 Response Matrix

The response matrix is derived from simulations that carry a limited statistical quality. The response was parametrised by continuous functions to level these out, but the errors of the function parameters still lead to an uncertainty in the calculated efficiency, energy misreconstruction and resolution of each zenith bin and primary species.

The uncertainty of the efficiency of the three zenith bins can be taken from eqs. 5.23. In the unfolding, these values are projected as errors on the flux, namely

$$\begin{aligned}\sigma_{\mathrm{eff},\Omega 0} &= \pm 0.007\\ \sigma_{\mathrm{eff},\Omega 1} &= \pm 0.011\\ \sigma_{\mathrm{eff},\Omega 2} &= \pm 0.015.\end{aligned} \tag{8.19}$$

An estimator for the uncertainties on the mean and width of the gaussian response functions can be taken from the errors of the p_0 parameters of eqs. 6.5 and 6.6. They both cause an uncertainty in the energy. The sums of errors found are

$$\begin{aligned}\sigma_{\mathrm{mat},\Omega 0} &= \pm 0.0015\\ \sigma_{\mathrm{mat},\Omega 1} &= \pm 0.003\\ \sigma_{\mathrm{mat},\Omega 2} &= \pm 0.004.\end{aligned} \tag{8.20}$$

Table 8.2: Summary of all systematic uncertainties with respect to $\log_{10} E$ and $\log_{10}(dI/d\log_{10} E)$. For comparison, an equivalent error on the energy is given in percent of E. (*) The uncertainty due to the HE interactions can be bigger, see sec. 8.2.3.

	$\log_{10} E$	$\log_{10}(dI/d\log_{10} E)$	E
threshold	0.007	–	1.6 %
snow, Ω0	0.009	–	2.1 %
snow, Ω1	0.014	–	3.2 %
snow, Ω2	0.017	–	3.9 %
saturation, $E < 30$ PeV	–	–	–
saturation, $E = 100$ PeV	0.02	–	4.6 %
atmosphere	0.014	–	3.2 %
instability	0.017	–	3.9 %
interaction model	0.004*	–	1.0 %*
calibration	0.03	–	6.9 %
unfolding	–	0.014	1.90 %
response matrix, Ω0	0.0015	0.007	1.01 %
response matrix, Ω1	0.003	0.011	1.6 %
response matrix, Ω2	0.004	0.015	2.2 %

8.2.7 Summary of Systematic Uncertainties

All values of uncertainties on $\log_{10} E$ and $\log_{10}(dI/d\log_{10} E)$ are summarised in tab. 8.2. In addition to these, an equivalent error on E is calculated using the conversion eq. 8.4. The errors apply after the spectrum is shifted by $\Delta \log_{10} E = +0.021$ to compensate for the misreconstruction due to the discriminator threshold inconsistency.

The snow and response matrix related errors depend on inclination, and the error from PMT saturation is energy dependent. Therefore the sum of uncertainties was calculated for each zenith bin and for energies below 30 PeV and at 100 PeV, which is the maximal energy of the presented results. Table 8.3 puts together all derived numbers.

Besides these errors of the whole spectrum, the energy dependent error σ_{sat} causes an uncertainty on the power index γ_2. With regular error propagation, and assuming a power law that is fitted over a range $\Delta_{\text{fit}} \log_{10} E$, this error can be estimated as

$$\sigma_\gamma = (-\gamma + 1) \frac{\sigma'_{\text{sat}}}{\Delta_{\text{fit}} \log_{10} E} \tag{8.21}$$

Table 8.3: Sum of systematic uncertainties of $\log_{10}(dI/d\log_{10} E)$ and $\log_{10} E$ for the zenith bins Ω_i and for energies below 30 PeV and at 100 PeV. The relative errors in the energy σ_E are calculated for comparison and include the uncertainty caused by the flux errors.

	flux	$E < 30\,\mathrm{PeV}$		$E = 100\,\mathrm{PeV}$	
zenith bin	$\sigma_{\lg I}$	$\sigma_{\lg E}$	σ_E	$\sigma_{\lg E}$	σ_E
Ω_0	0.016	0.039	9.3 %	0.044	10.3 %
Ω_1	0.018	0.041	9.7 %	0.045	10.7 %
Ω_2	0.021	0.042	10.0 %	0.046	11.0 %

where σ'_{sat} is the error on $\log_{10} E$ that can be expected in the fitted range. With the range that was fitted below, this yields a systematical error on γ_2 of

$$\sigma_{\gamma_2} = \pm 0.08 \tag{8.22}$$

For the comparison of spectra of individual zenith bins it is necessary to distinguish between errors that apply on all spectra equally and errors that might cause differences between the zenith bins. Uncertainties that apply independently on different inclinations are σ_{snow}, σ_{eff}, σ_{mat} and σ_{iter}. Minor effects can also be expected from different mean shower development under different atmospheric conditions or for different interaction models. These biases should however be correlated between the zenith bins and can thus be assumed to be comparably small.

The sum of independent errors for the Ω_i with respect to the flux, as they will be needed later, are

$$\begin{aligned} \sigma_{\mathrm{I},\Omega 0} &= \pm 0.026 \\ \sigma_{\mathrm{I},\Omega 1} &= \pm 0.034 \\ \sigma_{\mathrm{I},\Omega 2} &= \pm 0.041. \end{aligned} \tag{8.23}$$

8.3 Energy Spectra for Different Zenith Bands and Composition Assumptions

The four composition models introduced in sec. 6.1 are used to deconvolute the three raw spectra for the zenith bands Ω_i. The idea of analysing these zenith bands separately is that they can be expected to lead to compatible results if the response matrices are correct. Since the response matrices mainly depend on the unknown composition, requiring this compatibility may give a handle on composition.

The variations between the algorithms and different iteration depths turned out to be small and are included in the systematic errors. Hence, the following unfoldings will be performed using only the bayesian unfolding and an iteration depth of $\Delta\chi^2_{k:k-1} = 1.3$. The spectra and the gained fit parameters will be presented, and an analysis of the self-consistence of the results from different zenith bins will be performed that will be discussed in the next section.

8.3.1 Unfolded Spectra and Knee Fit Parameters

Figures 8.8 and 8.9 show the derived spectra. All spectra were fitted with the knee function as defined in eq. 6.1. The thresholds of the spectra, as defined in tab. 6.2, allow us to fit the ε and E_{knee} parameters only in the spectrum of zenith bin Ω_0. Since the reliability of the unfolding algorithm decreases with increasing statistical uncertainty, the upper end of the fit range was defined as the last unfolded bin with a relative error below 0.5. Supposing a poissonian origin of the statistical errors, this equals a requirement of 4 events per bin. Mostly, the upper end of the fitted range is about 1.9 in $\log_{10}(E/\,\mathrm{PeV})$, or 80 PeV.

Table 8.4 is a listing of all fit parameters. The error on γ_2 is only statistical and does not include the systematic uncertainty caused by saturated signals at high energies (eq. 8.22). The flux constant and knee position were corrected for the bias due to incorrect threshold simulation.

Here and in the following, averages are calculated from three bin or fit values derived from the three zenith bins. These values have a known statistical error, but the fact that they are from different zenith bins adds an additional systematic difference whose size is not known a priori. How the error of these three values with unknown systematic uncertainty is determined is described in appendix A.

Something that is not taken into account is the fact that the unfolded bins are correlated. These correlations are mainly to the nearest neighbour

Table 8.4: Knee fit parameters of all 12 unfolded spectra, as defined in eq. 6.1. $I_{\text{PeV,lg}}$ is given in terms of $10^{-6}\,\text{m}^{-2}\,\text{s}^{-1}\,\text{sr}^{-1}$, E_{knee} in PeV. The errors do not take into account the correlations of the unfolded bins to their nearest neighbour, which is in the order of $10-20\,\%$.

model	θ bin	$I_{\text{PeV,lg}}$	$-\gamma_1$	$-\gamma_2$	E_{knee}	ε	χ^2/ndf
only protons	Ω_0	3.61(10)	2.66(8)	3.05(2)	2.8(3)	5.8(3.4)	14.2/14
	Ω_1	3.23(5)	–	3.08(3)	–	–	11.6/12
	Ω_2	3.3(2)	–	3.17(6)	–	–	5.7/9
poly-gonato	Ω_0	4.21(9)	2.71(7)	3.12(3)	3.1(3)	4.7(2.7)	9.5/13
	Ω_1	3.92(7)	–	3.10(2)	–	–	14.2/12
	Ω_2	4.2(2)	–	3.13(4)	–	–	5.2/9
two-comp.	Ω_0	4.43(9)	2.75(6)	3.12(3)	3.1(3)	5.4(3.3)	9.7/13
	Ω_1	4.15(5)	–	3.11(2)	–	–	16.2/12
	Ω_2	4.6(2)	–	3.16(4)	–	–	5.4/9
only iron	Ω_0	8.39(4)	3.074(9)	3.29(2)	3.7(3)	2.7(7.0)	11.7/13
	Ω_1	9.91(9)	–	3.28(2)	–	–	21.7/13
	Ω_2	14.2(7)	–	3.37(4)	–	–	6.3/9

bins and in the order of $10-20\,\%$, depending on the unfolding matrix and also the shape of the raw spectra. Due to the relatively homogeneous response, this will most likely not influence any fitted parameters, but only the estimation of their errors. This treatment is an issue that may be addressed more precisely in future.

8.3.2 Compatibility between Zenith Bands

A remarkable point that will be discussed later is that some response matrices lead to more consistent spectra of the investigated zenith bins than others. Therefore, the agreement of the fit variables was studied and three quantities were calculated that characterise the compatibility between the data points of the spectra. Since generally an infinite statistical quality can rule out any a priori composition model, the calculated absolute probabilities should not be regarded a standalone result. Instead, they are converted to likelihood ratios, which give the relative probability of the models compared to the most probable of the four.

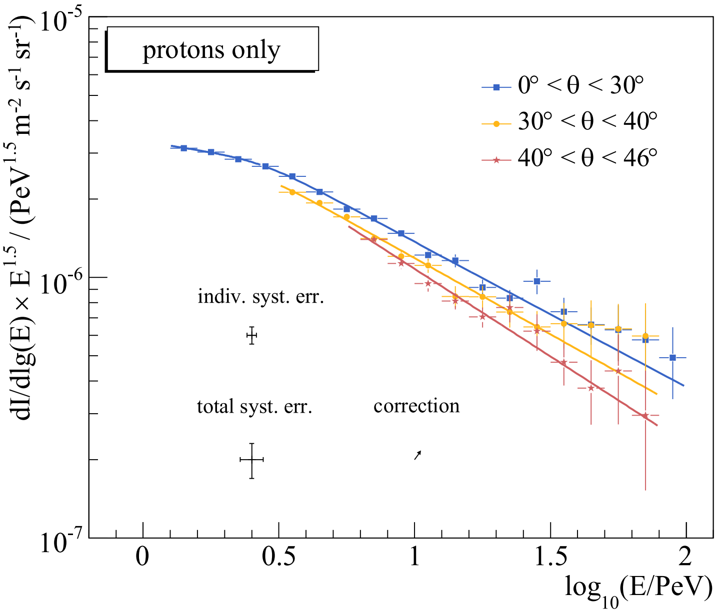

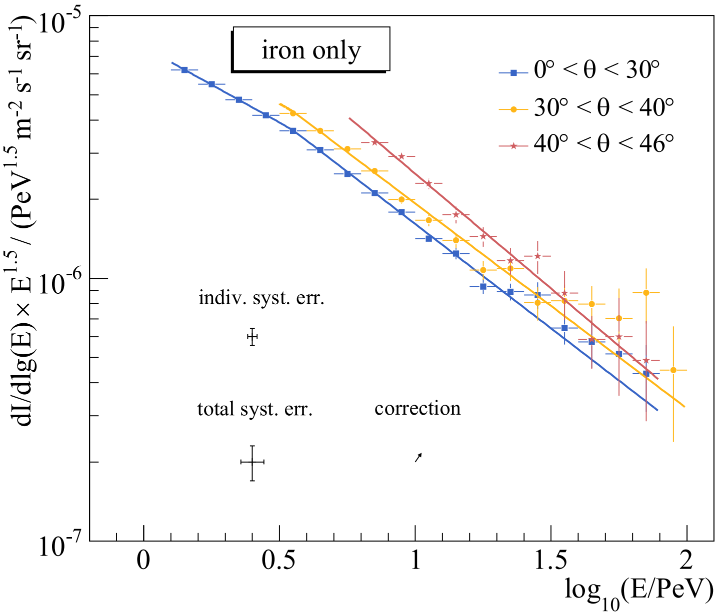

Figure 8.8: Unfolded spectra under pure proton and pure iron assumptions, derived with the bayesian algorithm and an iteration depth of $\Delta\chi^2_{k:k-1} = 1.3$. The black error bars are the total systematic error and the error afflicted independently on the individual zenith bins. The arrow indicates the correction to be applied due to inconsistent discriminator simulation.

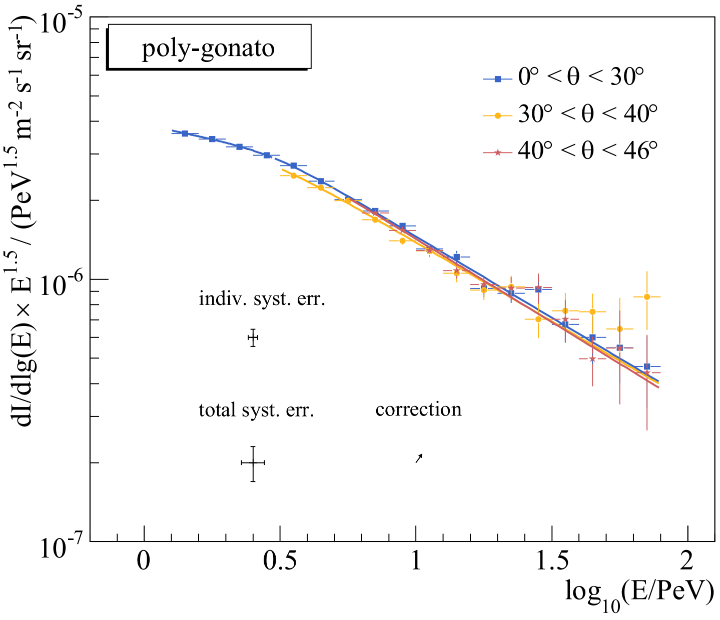

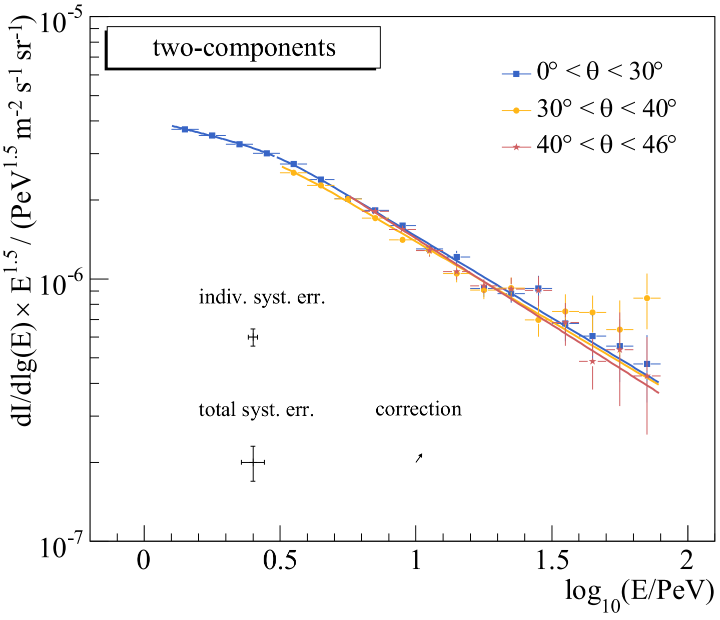

Figure 8.9: Unfolded spectra under the two mixed composition assumptions, derived with the bayesian algorithm and an iteration depth of $\Delta\chi^2_{k:k-1} = 1.3$. The black error bars are the total systematic error and the error afflicted independently on the individual zenith bins. The arrow indicates the correction to be applied due to inconsistent discriminator simulation.

Compatibility of the Fit Results

For the flux constant $I_{\mathrm{PeV,lg}}$ and the slope above the knee, γ_2, an average value can be calculated for each composition model. The comparison of the χ^2 function of the values with respect to this mean, and the number of degrees of freedom of this one-parameter fit ($N - 1 = 2$) can be used to calculate a probability that is an estimator of the compatibility of the three spectra. In the comparison of the flux constant, also the additional uncorrelated uncertainties of the zenith bins (eq. 8.23) are taken into account. Table 8.5(a) shows the means, χ^2 and probabilities for all four composition assumptions. As the poly-gonato matrix delivers the most probable results, the other probabilities are set in relation to that.

Compatibility of the Individual Energy Bins

A more general approach is to compare each individual energy bin of the spectra. For bins that are available in at least two zenith ranges, the mean, χ^2/ndf and probability can be calculated similarly to how it was done above. Multiplying all probabilities gained by the Ω_i of a given composition assumption leads to an overall probability for that assumption. Again, the independent systematic errors of the zenith bins (eq. 8.23) are added to the bin errors.

The results are listed in tab. 8.5(b). The two-component spectra show the biggest compatibility.

Compatibility of the Integral Flux

With the proton and iron assumption, the three unfolded spectra seem to be systematically shifted in flux. To emphasise this in the compatibility analysis, the integral fluxes can be compared, using the errors in the same manner as in the individual bin analysis before. Table 8.5(c) shows the χ^2/ndf, probabilites and likelihood ratios gained with this method. The integral flux was calculated using only bins that are available in all three unfolded zenith bins.

Table 8.5: Results of compatibility evaluations performed on the found spectra of different zenith bins under four composition assumptions. The three methods are described in the text. $I_{\mathrm{PeV,lg}}$ is given in terms of $10^{-6}\,\mathrm{m}^{-2}\,\mathrm{s}^{-1}\,\mathrm{sr}^{-1}$. It is defined in eq. 6.1.

	only protons	poly-gonato	two-components	only iron
(a) fit parameter compatibility				
$I_{\mathrm{PeV,lg}}$	3.34(12)	4.05(10)	4.26(11)	8.8(5)
χ^2/ndf	10.0/2	6.9/2	8.4/2	257/2
prob.	$6.7 \cdot 10^{-3}$	$3.2 \cdot 10^{-2}$	$1.53 \cdot 10^{-3}$	$6.9 \cdot 10^{-11}$
$-\gamma_2$	3.07(2)	3.110(14)	3.120(14)	3.294(19)
χ^2/ndf	3.9/2	0.61/2	1.25/2	4.1/2
prob.	0.145	0.74	0.54	0.126
total prob.	$9.8 \cdot 10^{-4}$	$2.3 \cdot 10^{-2}$	$8.2 \cdot 10^{-3}$	$8.7 \cdot 10^{-12}$
llh. ratio	**0.04**	**1.0**	**0.35**	$\mathbf{3.7 \cdot 10^{-10}}$
(b) single bin compatibility				
prob.	$4.5 \cdot 10^{-11}$	$1.06 \cdot 10^{-3}$	$1.13 \cdot 10^{-3}$	$2.3 \cdot 10^{-17}$
llh. ratio	$\mathbf{4.0 \cdot 10^{-8}}$	**0.94**	**1.0**	$\mathbf{2.0 \cdot 10^{-14}}$
(c) integral compatibility				
χ^2/ndf	20.0/2	1.9/2	1.7/2	42.4/2
prob.	$4.6 \cdot 10^{-5}$	$4.0 \cdot 10^{-1}$	$4.2 \cdot 10^{-1}$	$6.2 \cdot 10^{-10}$
llh. ratio	$\mathbf{1.1 \cdot 10^{-4}}$	**0.95**	**1.0**	$\mathbf{1.5 \cdot 10^{-9}}$

Chapter 9

Discussion and Outlook

The unfolding led to primary energy spectra that in general agree with what can be expected from other experiments. The reduced χ^2 values of the fits performed with the knee function do not indicate any incompatibility (see tab. 8.4). The knee is seen in the Ω_0 spectra derived with all model assumptions, and is located between 2.8 and 3.7 PeV. The change of the power index $\gamma_2 - \gamma_1$ is between -0.2 and -0.4, depending on the composition assumption.

The indices and absolute scale of the spectrum depend on the assumed composition. Taking into account the compatibility of the spectra from the three zenith bins, which was quantified in the previous paragraph, can help making a judgement about which composition model, and hence which spectral parameters, are more probable than others.

9.1 Sensitivity to Composition

As can be seen by eye in the spectrum plots (fig. 8.8 and 8.9) and in all probability estimations (tab. 8.5), the three spectra derived with the assumption of pure proton or pure iron composition are not compatible with each other. The most stringent likelihood ratios can be extracted from the comparison of individual energy bins. From this, a pure proton composition is disfavoured by $4 \cdot 10^{-8}$, and a pure iron composition by $2 \cdot 10^{-14}$. There is no clear preference between the two mixed composition models.

At this stage of investigation, several systematic errors are still estimated very crudely, for example the number of interaction models studied, and the detailed energy dependence of the systematic effects. The likelihood ratios might also vary if not a superposition of two response matrices was used but matrices were explicitely simulated for intermediate groups of nuclei (although this is unlikely to change the overall preference of the analysis). Because of these reasons, one should not overestimate the absolute rejection power of the probabilities. The meaning of the result to be emphasised at this point is that assuming isotropy of cosmic radiation can give a sensitive handle on composition using the presented unfolding method. In this analysis, a clear preference for the mixed composition models with increasing mass was found.

It is important to note that the overall uncertainty in the energy for the big part applies on all zenith angles equally, so this result holds despite the fact that the spectrum slightly deviates from the spectra of other experiments. Thus the presented analysis can be regarded a solid indication that the mixed composition and increase of mass, which is observed by other experiments, and which the poly-gonato and two-components model both inherit, is necessary to explain our data. The need for an increase of mass can also be seen qualitatively in the fact that in fig. 8.8, the spectra unfolded under proton assumption diverge towards higher energies, while the iron-based spectra converge, i.e. become more probable. As discussed in chapter 1, an increasing mean mass is a basic, but no exclusive feature of most astrophysical explanations of cosmic rays in the knee regime.

9.2 Comparison to Other Experiments

The calculated likelihood ratios do not show any clear preference between the two mixed composition models. Also, the fitted indices and flux constants are highly compatible. Therefore, only the spectrum derived with the poly-gonato assumption is chosen as the most probable all-particle spectrum for comparison with other experiments. To avoid discrete steps in the spectrum, the average of all three spectra is only calculated above 10 PeV, where the statistical errors dominate. Below that, the Ω_0 spectrum delivers sufficient data to be taken on its own. The derived spectrum is listed in tab. A.3 in Appendix C.

Figure 9.1 shows a comparison of this spectrum to previously measured data from other experiments. By eye, and in numbers, the knee position of $3.1 \pm 0.3\,(\text{stat.}) \pm 0.3\,(\text{sys.})$ PeV and the indices below the knee $\gamma_1 = -2.71 \pm 0.07\,(\text{stat.})$ and above the knee $\gamma_2 = -3.110 \pm 0.014\,(\text{stat.}) \pm 0.08\,(\text{sys.})$ agree within the uncertainties with what was found by other measurements. Table 9.1 gives a comparison with indices measured by the experiments introduced in sec. 1.5.2.

It might be worth mentioning that the indices derived for pure proton, mixed and pure iron assumptions coincide quite well with the corresponding

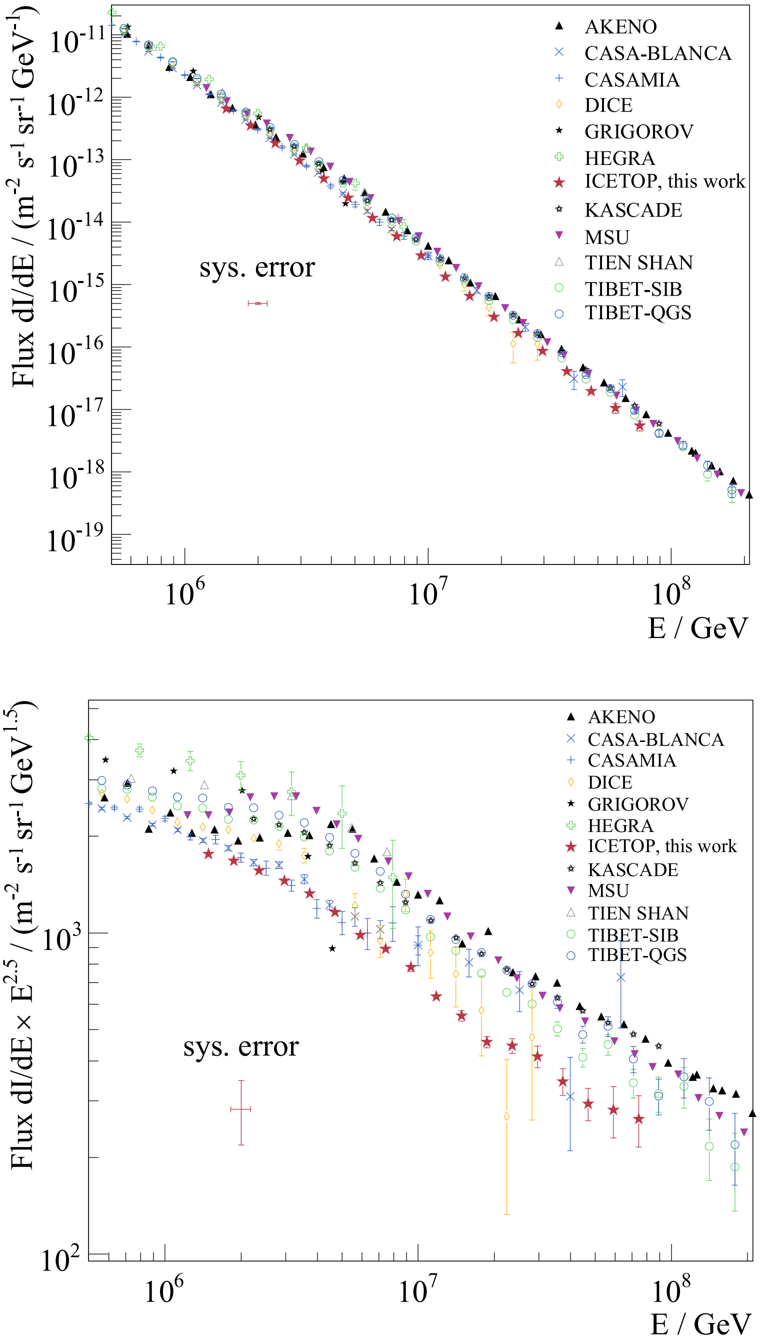

Figure 9.1: All-particle spectrum derived under poly-gonato composition assumption from all showers < 46° as described in the text. In the lower plot, the flux is multiplied by $E^{2.5}$, which is also taken into account in the shown systematic error bars. Compared to other experiments, the detected flux is lower, but still has high systematic uncertainty. The plotted data from other experiments were compiled by [7].

Table 9.1: Comparison of power indices and knee position in [10, 43, 85] and this work. E_{knee} is given in PeV. A range is given if several values for different assumptions are stated in the reference.

	E_{knee}	$-\gamma_1$	$-\gamma_2$
KASCADE	4.0(8) – 5.7(1.6)	2.70(6)	3.10(7) – 3.14(6)
TIBET	3.8(1) – 4.0(1)	2.65(1) – 2.67(1)	3.08(5) – 3.12(1)
TUNKA	—	2.71(5)	3.22(5)
this work	3.1(4)	2.71(7)	3.11(8)

values given in [43], where also spectra were calculated for different composition assumptions. The change of knee position under different assumptions is similar as well. This is although the assumptions in that analysis are taken into account differently — they are included in the energy estimator beforehand and not corrected by unfolding. Also, the energy estimator is taken from the integral of the LDF rather than at a fixed distance from the shower axis. Still, as can be seen in fig. 1.9, the similar altitude of the Tibet-III experiment ($606\,\mathrm{g/cm^2}$, IceTop: $680\,\mathrm{g/cm^2}$) leads to a similar response: The main effect of composition is at PeV energies, and becoming smaller at higher energies.

Although our spectrum roughly matches the CASAMIA result at low energies, and the DICE spectrum at higher energies, the absolute flux or energy scale appears to be lower than in most other spectra, for example those from the KASCADE or TIBET-III experiments. The systematic flux uncertainties of these other spectra, depending on energy, are in the order of 20 – 25 %. Taking into account our own systematic uncertainty (∼27 – 33 % in flux), the difference is only about $1.3\,\sigma$, so no clear deviation can be stated at this point. The fact that our found knee energy is slightly lower than in other experiments indicates that the difference might be in the energy assignment rather than in the flux estimation.

Instead of being a straight power law above the knee, the measured spectrum indicates a slight positive curvature (in log-scale) up to around 20 PeV, where it stabilises. Although its statistical significance is too small to judge from our spectrum alone, it might be worthwhile mentioning that the spectra from KASCADE, MSU and TIBET show a similar feature.

9.3 Prospects and Outlook

The presented energy spectrum is the first quantitative investigation of the PeV cosmic ray flux with IceTop. Besides collecting and analysing more data, several of the systematic uncertainties, and also the analysis techniques, can be improved in future to test the validity of the above spectrum, its features and absolute scale.

Data Sample

In the near future, the whole SMT data taken in 2007 is available, which has a lifetime of approximately 6 months. Since most of the presented data was taken from the SMT_Large-triggered sample, there is not much to be expected from the omitted prescale factor, but still the statistical power will be increased by a factor of six. This can extend the upper end of the energy spectrum to about 150 PeV.

In future years, the detector is growing, and at the same time data will be taken, which should rapidly increase the amount of available data. However, the response matrix has to be reevaluated for each year, since the containment criteria, which are the dominant data cuts, will change.

Reduction of Systematic Uncertainties

Some systematic problems might in the long term be reducible. The threshold function of the single pulse detection, and its impact on the silent likelihood (see sec. 5.3) can be regarded among the most urgent of them. A detailed study of pulse width and amplitude distributions, and a systematic comparison of the pulse discrimination behaviour in data and simulation, might shed light on the issue and allow us to improve the performance of the fit. In particular, this might extend the range of understood data to lower energies.

The possible increase of signal attenuation due to PMT saturation might already be solved for data taken in 2008 or later since the gains of the LG DOMs were lowered by a factor of five. If not, the issue can be solved by simulating showers up to higher energies. At present, this is quite inefficient due to the huge amount of particles that the CORSIKA code has to deal with. In future, this can be improved either by making use of the thinning option (see sec. 1.5.3), which requires a concept of how to treat weighted particles on ground level, or by using faster shower simulation packages such as SENECA [86]. This package uses cascade equations to speed up the generation of the electromagnetic shower component.

Improving the atmosphere related uncertainties might need a detailed comparison and understanding of measured pressure profiles and existing CORSIKA parametrisations. The simulations for future analyses should then be produced in well consistence with the season that the target data is supposed to be taken in.

The uncertainties from the unfolding and the response matrix are comparably small, but can also be reduced if needed. The quality of the response matrix can be increased by simply simulating more showers. It might serve the transparency of the response matrix estimation to circumvent the binwise analysis of responses and do a two-dimensional fit on all (reweighted) data at once. The unfolding algorithms might profit from trying out smoothing algorithms that take into account the fact that no spikes or edges are expected in the spectrum. To some extend, this was already tried out for this thesis, but turned out to be more complex an intervention than expected — the iteration process becomes less predictable and probably needs a different characterisation of convergence.

As mentioned before, there is no efficient concept yet how to parametrise the impact of the snow on the data. The problem about it is that particles do not only lose energy, but might produce more particles that enter the tank, depending on energy. At the time of this analysis, it might only have a small influence, but each year the overall snow level above the tanks rises by about 30 cm, depending on the physical surrounding of the tank. So it might soon not only be a crucial effect for particles that enter the tanks from the side, but actually for all detected particles.

Although the muon calibration helps avoiding all uncertainties connected to what happens inside the detector tanks, it is still the biggest uncertainty in this analysis, and a topic that a lot of efforts have already been put into. The problem about it is the understanding of the calibration spectra to a level of a few percents, which can only be established by simulations. The low-energetic shower simulations that are needed for that are however very inefficient. In addition, the inner surface materials in the `tanktop` simulation still do not reproduce width, height, and charge of muon pulses at the same time, so they can not be trusted on the percent level. Although it is unlikely to see a major breakthrough in the issue soon, it should be mentioned that despite its size, it can be regarded the most unproblematic uncertainty, because it is independent of energy, zenith angle and composition. So it does not qualitatively influence the analyses.

Improvements of the Analysis

In the forthcoming seasons, with a bigger array, more stations will be contained within the outer row of tanks. With that it might be possible to analyse showers of smaller multiplicity than five. This will probably require a fixed lateral index parameter and a more consistent description of the silent likelihood (eq. 5.5), including the correct correlation factor C_t between signals of a station. An additional option to lower the degrees of freedom, and thus the station multiplicity requirement, is to fix the core position of a contained event to its COG, and only fit the shower size. This will probably lead to an unprecise or biased energy estimation, but since it can be expected to be reproduced in simulation, it might be understood and corrected for.

A way to proceed with a composition analysis could be to construct a flexible parametrisation of the relative composition and perform a fit of its parameters by maximising the likelihood quantities discussed in the previous chapter. Since it cannot be presumed that there is only one unique relative composition that leads to an isotropic appearance of the flux, the number of parameters should however be small to avoid multiple maxima of the likelihood function. For example, in the energy range visible to all zenith bins, every single spectrum is effectively defined by one power index γ_2 and one flux constant. Thus the number of measured variables with three zenith bins is six. Subtracting the true flux and index parameters from that, four degrees of freedom remain. Hence, with the presented setup of the analysis, no more than three additional parameters can be expected to be fitted well. Also, a better understanding of all systematic uncertainties might be necessary to assign error bars to the found probabilities.

Using the presented unfolding method to investigate composition is quite complementary to the approach pursued in an IceTop-IceCube coincident measurement — while the unfolding method uses the mass dependence of the shower evolution, a coincident analysis makes use of the particle mixture. The development of a combination of the two might thus lead to a reduction of systematic problems of both analyses.

Chapter 10

Summary

The main goal of this thesis was the investigation of the all-particle energy spectrum of charged cosmic rays in the regime between 1 and 80 PeV at the South Pole. This was done using the new km^2-scale IceTop air shower array, which is part of the presently constructed IceCube Observatory. Since it is the first analysis of this kind with IceTop, reconstruction algorithms for air showers had to be established, and a deconvolution procedure was developed to derive energy spectra for given assumptions on the chemical composition. Using data from different inclinations, the self-consistency of the assumptions could be estimated, which is a test of their correctness. This is a new analysis technique that shows that IceTop alone can be sensitive to cosmic ray composition. The parameters of the all-particle energy spectrum derived with the most likely composition model agree with those found in other experiments, if the systematic uncertainties are taken into account.

⋆⋆

The development of air shower reconstruction algorithms was based on the studies presented in chapter 4, where the single-particle light response of the IceTop Cherenkov tanks was characterised in dependence of particle species and energy. This was done using a detailed detector simulation package which realistically traces all particles and photons and simulates their reactions and absorption.

Based on this, algorithms were developed to interpret the shower events recorded by the array, which consist of time stamps and integrated lightcurves measured by photomultiplier tubes in the detector tanks. This required the definition of a lateral distribution function of shower signals, and a corresponding likelihood function. It includes all information of the measured signals, but also from detectors that did not have a trigger. From a fit of this likelihood function, the direction and centre of a shower, the shower size, an age parameter, and an estimator of the primary energy can be extracted. With a minimal number of essential cuts, resolutions were achieved that are well competitive with those of other air shower experiments. In the energy regime of full acceptance, which is above $1 - 3\,\mathrm{PeV}$, depending on inclination, the 68 % resolutions are $1.5(2)\,^\circ$ in direction, $8.8(5)\,\mathrm{m}$ for the shower centre, and about 12 % in energy. The effective area of the 2007 array in the regime of constant efficiency turned out to be between 0.0936(16) and $0.0792(27)\,\mathrm{km}^2$ for zenith angles between $0\,^\circ$ and $46\,^\circ$.

An extensive simulation and quantitative survey of the reconstructed energy response in dependence on primary energy and zenith angle led to the definition of response matrices in chapter 6. These were developed for proton and iron primaries and for showers of three inclination bins: $\Omega_0 = [0\,^\circ, 30\,^\circ]$, $\Omega_1 = [30\,^\circ, 40\,^\circ]$ and $\Omega_2 = [40\,^\circ, 46\,^\circ]$. With the response matrices, expectations of reconstructed energy distributions could be calculated for different assumptions on primary chemical composition. These were compared to energy distributions gained by full detector simulations and experimental data. It led to the insight that there is a general qualitative agreement, but the influence of the chemical composition on the measurement is not negligible. Also, a disagreement in the position of the threshold between data and simulation was found. It was determined as most probably being caused by an inconsistency in the discriminator simulation. Thresholds were defined above which the agreement between data and simulation is sufficiently good to perform an unfolding.

Two iterative unfolding methods were implemented, namely a bayesian unfolding and the Gold algorithm, described in chapter 7. Their performance was scrutinised, the optimal iteration depth was defined and a method was established to assign statistical error bars on the unfolded spectra.

Chapter 8 contains the main results on the investigation of the energy spectrum. Using data from August 2007, with a lifetime of $2.30 \cdot 10^6\,\mathrm{s}$, a total of 734982 events were analysed. The total exposure of all three zenith bins is $3.86 \cdot 10^{11}\,\mathrm{m}^2\,\mathrm{s}\,\mathrm{sr}$.

Two mixed composition models, and the assumptions of pure proton and pure iron composition, were used to unfold the distributions of reconstructed energies. The all-particle energy spectra for the three zenith regimes gained under these composition assumptions are shown in fig. 8.8 and 8.9. An obvious zenith bin inconsistency of the spectra found with pure proton and pure iron assumption was noticed, and likelihood ratios were defined that can serve as a measure for the largeness of this disagreement. All of these likelihood ratios indicate a strong preference for the two models with mixed composition. The statistical and systematic errors were however not small enough to find a clear statement which of the two is more likely.

This result means that requiring an isotropic flux of cosmic rays can be used to perform a composition sensitive measurement with only a surface detector array. Given the fact that up to now, composition analyses were mainly tried using additional information from muon detectors or from observations of the longitudinal shower development, this is the main finding of this thesis.

The composition assumption with the highest likelihood ratio was used to extract an all-particle energy spectrum. The so-called knee feature was found at

$$E_{\text{knee}} = 3.1 \pm 0.3\,(\text{stat.}) \pm 0.3\,(\text{sys.})\,\text{PeV}. \tag{10.1}$$

The indices below and above that were determined to be

$$\begin{aligned} \gamma_1 &= -2.71 \pm 0.07\,(\text{stat.}) \\ \gamma_2 &= -3.110 \pm 0.014\,(\text{stat.}) \pm 0.08\,(\text{sys.}). \end{aligned} \tag{10.2}$$

This supports other recent measurements of the spectrum, which verifies the general performance of the method, and the general ability of IceTop to competitively investigate PeV cosmic rays. The absolute flux is comparably low, which could already be observed before the unfolding. Yet it turns out to be still compatible within about $1.5\,\sigma$ of the systematic uncertainty. The found spectrum is compared to other measurements in fig. 9.1.

Table 8.2 summarises the overall systematic errors of the energy spectrum that presently remain. The biggest impacts come from the calibration, the uncertainty of atmospheric parameters and the snow around the tanks, which at present is not taken into account in the simulation.

The next steps that have to be done to improve future possibilities are to systematically study the problem of the discrimination threshold and to figure out a way to parametrise or simulate the snow masses that will continue to pile up above the detector tanks in future years. Also, an intensive study of measured pressure profiles of the south polar atmosphere might improve the understanding of the data significantly. Once these systematic problems are reduced or understood in more detail, the presented analysis method can be used to make quantitative statements about the composition evolution in the regime that is most interesting for the understanding of galactic and extragalactic cosmic radiation.

Appendix A

On the Error Estimation of a Weighted Mean Derived from Few Measured Values of Differing, Unknown Systematic Uncertainty

> *"Le doute n'est pas une condition agréable, mais la certitude est absurde."*
>
> Voltaire,
> *Letter to Frederick II of Prussia*

If a quantity x is to be determined from N comparable measurements x_i with errors σ_i, it can be estimated by calculating the weighted mean:

$$\bar{x} = \frac{\sum_i \frac{x_i}{\sigma_i^2}}{\sum_i \frac{1}{\sigma_i^2}} \tag{A.1}$$

The error of that, derived with error propagation, is

$$\sigma_{\bar{x},\mathrm{prop}} = \frac{1}{\sqrt{\sum_i \frac{1}{\sigma_i^2}}}. \tag{A.2}$$

It is equivalent to the error derived from the $\chi^2(\bar{x})$ function of the values x_i. This assumes that the measured values follow a gaussian distribution around the true value of x. If this is not the case, for example because the measured values come from different measurement techniques that bear independent systematic errors, eq. A.2 will lead to an underestimation of the error. This is because it does not take into account the spread of the data caused by the the systematic difference.

In this case, the error of the weighted mean has to be calculated from the standard deviation of the data points [87] as

$$\begin{aligned}\sigma_{\bar{x},\mathrm{std}} &= \sqrt{\frac{\sum_i \frac{(x_i-\bar{x})^2}{\sigma_i^2}}{(N-1)\sum_i \frac{1}{\sigma_i^2}}} \\ &= \sqrt{\frac{\chi^2}{N-1}} \cdot \sigma_{\bar{x},\mathrm{prop}}\end{aligned} \tag{A.3}$$

For data dominated by statistical errors, usually $\chi^2/(N-1) \approx 1$, and $\sigma_{\bar{x},\mathrm{prop}} \approx \sigma_{\bar{x},\mathrm{std}}$. However, if the the amount of data points N is small, there is an increasing probability to randomly get a small spread of these points and therefore a $\chi^2/(N-1)$ well below 1. In this case, the error on the mean can become unrealistically small in comparison with the measurement errors σ_i.

The probability P that the data do follow a normal distribution, and A.2 applies, can be calculated from the χ^2 and the degrees of freedom $N-1$. The probability that the systematic uncertainties dominate, and eq. A.3 applies, is $1-P$. With this, the error of a weighed mean derived from values of different, but unknown systematic uncertainty can be calculated as a sum of $\sigma_{\bar{x},\mathrm{prop}}$ and $\sigma_{\bar{x},\mathrm{std}}$, weighted with the probabilities [88]:

$$\begin{aligned}\sigma_{\bar{x}} &= \sqrt{P\,\sigma_{\bar{x},\mathrm{prop}}^2 + (P-1)\,\sigma_{\bar{x},\mathrm{std}}^2} \\ &= \sqrt{\frac{1}{\sum_i \frac{1}{\sigma_i^2}}\left(P + (1-P)\frac{\chi^2}{N-1}\right)}\end{aligned} \tag{A.4}$$

It should be noted that this effectively scales up the errors to account for systematic differences between the measured values. If this is done with many quantities $x, y, z, \ldots$ that are estimated from measurements $x_i, y_i, z_i, \ldots$ that have correlated systematic offsets, this might lead to inconsistencies when these values are fitted together. An example of this is a set of N histograms where $x, y, z, \ldots$ are the bins. In this case, only eq. A.2 should be applied.

Appendix B

Simulated Shower Event Numbers

Table A.1: Number of independent showers simulated for the generation of the response matrices, and studies of detector resolutions and efficiencies. Each shower was resampled 200 times on a radius of 1200 m. The nomenclature of the zenith bins Ω_i follows sec. 8.1.

	proton			iron		
$\log_{10}(E/\mathrm{TeV})$	Ω_0	Ω_1	Ω_2	Ω_0	Ω_1	Ω_2
2.0 – 2.1	2200	2400	2200	2200	1600	2000
2.1 – 2.2	2040	2040	2040	1920	2040	1800
2.2 – 2.3	1900	2100	2000	2000	2000	1900
2.3 – 2.4	1800	2100	2100	1900	2000	2000
2.4 – 2.5	585	585	585	495	540	585
2.5 – 2.6	585	585	540	585	540	585
2.6 – 2.7	440	480	520	440	520	520
2.7 – 2.8	200	520	520	440	480	520
2.8 – 2.9	540	540	500	540	520	500
2.9 – 3.0	525	495	495	495	510	435
3.0 – 3.1	225	210	210	195	225	210
3.1 – 3.2	220	210	200	200	210	210
3.2 – 3.3	210	200	190	200	200	210
3.3 – 3.4	213	100	110	110	100	95
3.4 – 3.5	210	110	110	90	90	100
3.5 – 3.6	96	51	45	54	54	54
3.6 – 3.7	96	54	45	51	54	51
3.7 – 3.8	96	54	45	51	54	51
3.8 – 3.9	86	44	42	48	48	52
3.9 – 4.0	87	50	41	49	50	50

	proton			iron		
$\log_{10}(E/\mathrm{TeV})$	Ω_0	Ω_1	Ω_2	Ω_0	Ω_1	Ω_2
4.0 – 4.1	21	22	22	22	20	21
4.1 – 4.2	20	22	21	21	21	22
4.2 – 4.3	19	20	21	21	18	20
4.3 – 4.4	19	14	19	19	17	20
4.4 – 4.5	22	7	15	14	20	21

Appendix C

Listing of Energy Spectra

Table A.2: Listing of the raw energy spectra shown in fig. 6.7, as reconstructed under proton assumption. The energy bin borders are given in $\log_{10}(E/\mathrm{PeV})$, N is the number of events in that bin, and $dI/d\log_{10}E$ is the flux per unit $\log_{10}E$ in $1/\mathrm{m}^2\,\mathrm{s}\,\mathrm{sr}$. This flux is corrected by the efficiency of the energy bin (eq. 5.23). The event numbers that are reduced by a prescale factor of 5 are marked by $(^*)$.

$\Delta\log_{10}(E/\mathrm{PeV})$	N	$dI/d\log_{10}E$
Zenith Bin 0		
-0.05 – 0.00	7821^*	$4.33\cdot10^{-6}\pm4.89\cdot10^{-8}$
0.00 – 0.05	6407^*	$3.54\cdot10^{-6}\pm4.43\cdot10^{-8}$
0.05 – 0.10	5204^*	$2.88\cdot10^{-6}\pm3.99\cdot10^{-8}$
0.10 – 0.15	21698	$2.40\cdot10^{-6}\pm1.63\cdot10^{-8}$
0.15 – 0.20	17758	$1.96\cdot10^{-6}\pm1.47\cdot10^{-8}$
0.20 – 0.25	14307	$1.58\cdot10^{-6}\pm1.32\cdot10^{-8}$
0.25 – 0.30	11721	$1.30\cdot10^{-6}\pm1.20\cdot10^{-8}$
0.30 – 0.35	9381	$1.04\cdot10^{-6}\pm1.07\cdot10^{-8}$
0.35 – 0.40	7603	$8.41\cdot10^{-7}\pm9.64\cdot10^{-9}$
0.40 – 0.45	6159	$6.81\cdot10^{-7}\pm8.68\cdot10^{-9}$
0.45 – 0.50	4979	$5.51\cdot10^{-7}\pm7.80\cdot10^{-9}$
0.50 – 0.55	4077	$4.51\cdot10^{-7}\pm7.06\cdot10^{-9}$
0.55 – 0.60	3174	$3.51\cdot10^{-7}\pm6.23\cdot10^{-9}$
0.60 – 0.65	2581	$2.85\cdot10^{-7}\pm5.62\cdot10^{-9}$
0.65 – 0.70	2034	$2.25\cdot10^{-7}\pm4.99\cdot10^{-9}$
0.70 – 0.75	1587	$1.76\cdot10^{-7}\pm4.41\cdot10^{-9}$
0.75 – 0.80	1228	$1.36\cdot10^{-7}\pm3.88\cdot10^{-9}$

$\Delta\log_{10}(E/\mathrm{PeV})$	N	$dI/d\log_{10}E$
0.80 – 0.85	1022	$1.13 \cdot 10^{-7} \pm 3.54 \cdot 10^{-9}$
0.85 – 0.90	817	$9.04 \cdot 10^{-8} \pm 3.16 \cdot 10^{-9}$
0.90 – 0.95	651	$7.20 \cdot 10^{-8} \pm 2.82 \cdot 10^{-9}$
0.95 – 1.00	512	$5.66 \cdot 10^{-8} \pm 2.50 \cdot 10^{-9}$
1.00 – 1.05	405	$4.49 \cdot 10^{-8} \pm 2.23 \cdot 10^{-9}$
1.05 – 1.10	333	$3.68 \cdot 10^{-8} \pm 2.02 \cdot 10^{-9}$
1.10 – 1.15	233	$2.58 \cdot 10^{-8} \pm 1.69 \cdot 10^{-9}$
1.15 – 1.20	195	$2.16 \cdot 10^{-8} \pm 1.54 \cdot 10^{-9}$
1.20 – 1.25	188	$2.09 \cdot 10^{-8} \pm 1.52 \cdot 10^{-9}$
1.25 – 1.30	124	$1.37 \cdot 10^{-8} \pm 1.23 \cdot 10^{-9}$
1.30 – 1.35	92	$1.03 \cdot 10^{-8} \pm 1.07 \cdot 10^{-9}$
1.35 – 1.40	77	$8.63 \cdot 10^{-9} \pm 9.77 \cdot 10^{-10}$
1.40 – 1.45	64	$7.08 \cdot 10^{-9} \pm 8.85 \cdot 10^{-10}$
1.45 – 1.50	66	$7.30 \cdot 10^{-9} \pm 8.98 \cdot 10^{-10}$
1.50 – 1.55	50	$5.64 \cdot 10^{-9} \pm 7.90 \cdot 10^{-10}$
1.55 – 1.60	36	$4.09 \cdot 10^{-9} \pm 6.73 \cdot 10^{-10}$
1.60 – 1.65	31	$3.43 \cdot 10^{-9} \pm 6.16 \cdot 10^{-10}$
1.65 – 1.70	23	$2.54 \cdot 10^{-9} \pm 5.30 \cdot 10^{-10}$
1.70 – 1.75	20	$2.21 \cdot 10^{-9} \pm 4.95 \cdot 10^{-10}$
1.75 – 1.80	16	$1.88 \cdot 10^{-9} \pm 4.56 \cdot 10^{-10}$
1.80 – 1.85	10	$1.11 \cdot 10^{-9} \pm 3.50 \cdot 10^{-10}$
1.85 – 1.90	15	$1.66 \cdot 10^{-9} \pm 4.28 \cdot 10^{-10}$
1.90 – 1.95	5	$5.53 \cdot 10^{-10} \pm 2.47 \cdot 10^{-10}$
1.95 – 2.00	9	$9.95 \cdot 10^{-10} \pm 3.32 \cdot 10^{-10}$
2.00 – 2.05	5	$5.53 \cdot 10^{-10} \pm 2.47 \cdot 10^{-10}$
2.05 – 2.10	3	$4.42 \cdot 10^{-10} \pm 2.21 \cdot 10^{-10}$
Zenith Bin 1		
0.30 – 0.35	6029	$9.89 \cdot 10^{-7} \pm 1.27 \cdot 10^{-8}$
0.35 – 0.40	4675	$7.67 \cdot 10^{-7} \pm 1.12 \cdot 10^{-8}$
0.40 – 0.45	3816	$6.26 \cdot 10^{-7} \pm 1.01 \cdot 10^{-8}$
0.45 – 0.50	3105	$5.09 \cdot 10^{-7} \pm 9.14 \cdot 10^{-9}$
0.50 – 0.55	2331	$3.82 \cdot 10^{-7} \pm 7.92 \cdot 10^{-9}$
0.55 – 0.60	1971	$3.23 \cdot 10^{-7} \pm 7.28 \cdot 10^{-9}$
0.60 – 0.65	1552	$2.55 \cdot 10^{-7} \pm 6.46 \cdot 10^{-9}$
0.65 – 0.70	1191	$1.95 \cdot 10^{-7} \pm 5.66 \cdot 10^{-9}$
0.70 – 0.75	965	$1.58 \cdot 10^{-7} \pm 5.10 \cdot 10^{-9}$
0.75 – 0.80	716	$1.17 \cdot 10^{-7} \pm 4.39 \cdot 10^{-9}$
0.80 – 0.85	626	$1.03 \cdot 10^{-7} \pm 4.10 \cdot 10^{-9}$

$\Delta\log_{10}(E/\mathrm{PeV})$	N	$dI/d\log_{10}E$
0.85 – 0.90	438	$7.18\cdot10^{-8}\pm3.43\cdot10^{-9}$
0.90 – 0.95	325	$5.33\cdot10^{-8}\pm2.96\cdot10^{-9}$
0.95 – 1.00	268	$4.41\cdot10^{-8}\pm2.69\cdot10^{-9}$
1.00 – 1.05	236	$3.87\cdot10^{-8}\pm2.52\cdot10^{-9}$
1.05 – 1.10	175	$2.89\cdot10^{-8}\pm2.18\cdot10^{-9}$
1.10 – 1.15	130	$2.15\cdot10^{-8}\pm1.88\cdot10^{-9}$
1.15 – 1.20	104	$1.71\cdot10^{-8}\pm1.67\cdot10^{-9}$
1.20 – 1.25	81	$1.33\cdot10^{-8}\pm1.48\cdot10^{-9}$
1.25 – 1.30	69	$1.13\cdot10^{-8}\pm1.36\cdot10^{-9}$
1.30 – 1.35	54	$9.02\cdot10^{-9}\pm1.22\cdot10^{-9}$
1.35 – 1.40	55	$9.19\cdot10^{-9}\pm1.23\cdot10^{-9}$
1.40 – 1.45	32	$5.25\cdot10^{-9}\pm9.28\cdot10^{-10}$
1.45 – 1.50	25	$4.10\cdot10^{-9}\pm8.20\cdot10^{-10}$
1.50 – 1.55	28	$4.76\cdot10^{-9}\pm8.83\cdot10^{-10}$
1.55 – 1.60	17	$2.79\cdot10^{-9}\pm6.76\cdot10^{-10}$
1.60 – 1.65	22	$3.61\cdot10^{-9}\pm7.69\cdot10^{-10}$
1.65 – 1.70	10	$1.80\cdot10^{-9}\pm5.44\cdot10^{-10}$
1.70 – 1.75	14	$2.46\cdot10^{-9}\pm6.35\cdot10^{-10}$
1.75 – 1.80	12	$1.97\cdot10^{-9}\pm5.68\cdot10^{-10}$
1.80 – 1.85	6	$9.84\cdot10^{-10}\pm4.02\cdot10^{-10}$
1.85 – 1.90	6	$1.15\cdot10^{-9}\pm4.34\cdot10^{-10}$
1.90 – 1.95	11	$1.97\cdot10^{-9}\pm5.68\cdot10^{-10}$
1.95 – 2.00	1	$1.64\cdot10^{-10}\pm1.64\cdot10^{-10}$
2.00 – 2.05	4	$8.20\cdot10^{-10}\pm3.67\cdot10^{-10}$
2.05 – 2.10	1	$1.64\cdot10^{-10}\pm1.64\cdot10^{-10}$
	ZENITH BIN 2	
0.55 – 0.60	1235	$3.05\cdot10^{-7}\pm8.67\cdot10^{-9}$
0.60 – 0.65	972	$2.40\cdot10^{-7}\pm7.68\cdot10^{-9}$
0.65 – 0.70	698	$1.72\cdot10^{-7}\pm6.51\cdot10^{-9}$
0.70 – 0.75	553	$1.36\cdot10^{-7}\pm5.80\cdot10^{-9}$
0.75 – 0.80	466	$1.15\cdot10^{-7}\pm5.33\cdot10^{-9}$
0.80 – 0.85	355	$8.75\cdot10^{-8}\pm4.64\cdot10^{-9}$
0.85 – 0.90	303	$7.47\cdot10^{-8}\pm4.29\cdot10^{-9}$
0.90 – 0.95	218	$5.37\cdot10^{-8}\pm3.64\cdot10^{-9}$
0.95 – 1.00	168	$4.14\cdot10^{-8}\pm3.19\cdot10^{-9}$
1.00 – 1.05	115	$2.83\cdot10^{-8}\pm2.64\cdot10^{-9}$
1.05 – 1.10	104	$2.56\cdot10^{-8}\pm2.51\cdot10^{-9}$
1.10 – 1.15	89	$2.19\cdot10^{-8}\pm2.33\cdot10^{-9}$

$\Delta \log_{10}(E/\mathrm{PeV})$	N	$dI/d\log_{10} E$
1.15 – 1.20	66	$1.65 \cdot 10^{-8} \pm 2.02 \cdot 10^{-9}$
1.20 – 1.25	41	$1.01 \cdot 10^{-8} \pm 1.58 \cdot 10^{-9}$
1.25 – 1.30	40	$9.86 \cdot 10^{-9} \pm 1.56 \cdot 10^{-9}$
1.30 – 1.35	31	$7.64 \cdot 10^{-9} \pm 1.37 \cdot 10^{-9}$
1.35 – 1.40	34	$8.63 \cdot 10^{-9} \pm 1.46 \cdot 10^{-9}$
1.40 – 1.45	27	$6.65 \cdot 10^{-9} \pm 1.28 \cdot 10^{-9}$
1.45 – 1.50	12	$2.96 \cdot 10^{-9} \pm 8.54 \cdot 10^{-10}$
1.50 – 1.55	16	$4.19 \cdot 10^{-9} \pm 1.02 \cdot 10^{-9}$
1.55 – 1.60	12	$2.96 \cdot 10^{-9} \pm 8.54 \cdot 10^{-10}$
1.60 – 1.65	8	$1.97 \cdot 10^{-9} \pm 6.97 \cdot 10^{-10}$
1.65 – 1.70	6	$1.48 \cdot 10^{-9} \pm 6.04 \cdot 10^{-10}$
1.70 – 1.75	4	$1.23 \cdot 10^{-9} \pm 5.51 \cdot 10^{-10}$
1.75 – 1.80	3	$7.39 \cdot 10^{-10} \pm 4.27 \cdot 10^{-10}$
1.80 – 1.85	6	$1.73 \cdot 10^{-9} \pm 6.52 \cdot 10^{-10}$
1.85 – 1.90	1	$2.46 \cdot 10^{-10} \pm 2.46 \cdot 10^{-10}$
1.90 – 1.95	3	$7.39 \cdot 10^{-10} \pm 4.27 \cdot 10^{-10}$
1.95 – 2.00	2	$4.93 \cdot 10^{-10} \pm 3.49 \cdot 10^{-10}$
2.05 – 2.10	1	$2.46 \cdot 10^{-10} \pm 2.46 \cdot 10^{-10}$

Table A.3: Listing of the unfolded energy spectrum shown in fig. 9.1, as extracted under poly-gonato assumption. The energy bin borders are given in $\log_{10}(E/\mathrm{PeV})$, $dI/d\log_{10} E$ is the flux per unit $\log_{10} E$ in $1/\mathrm{m}^2\,\mathrm{s}\,\mathrm{sr}$. All systematic errors are converted and included in the given flux error.

$\Delta \log_{10}(E/\mathrm{PeV})$	$dI/d\log_{10} E$	stat.	syst.
0.1 – 0.2	$2.14 \cdot 10^{-6}$	$\pm 1.1 \cdot 10^{-8}$	$\pm 6.0 \cdot 10^{-7}$
0.2 – 0.3	$1.45 \cdot 10^{-6}$	$\pm 8.8 \cdot 10^{-9}$	$\pm 4.0 \cdot 10^{-7}$
0.3 – 0.4	$9.53 \cdot 10^{-7}$	$\pm 7.1 \cdot 10^{-9}$	$\pm 2.7 \cdot 10^{-7}$
0.4 – 0.5	$6.27 \cdot 10^{-7}$	$\pm 5.3 \cdot 10^{-9}$	$\pm 1.7 \cdot 10^{-7}$
0.5 – 0.6	$4.05 \cdot 10^{-7}$	$\pm 5.4 \cdot 10^{-9}$	$\pm 1.1 \cdot 10^{-7}$
0.6 – 0.7	$2.51 \cdot 10^{-7}$	$\pm 4.2 \cdot 10^{-9}$	$\pm 7.0 \cdot 10^{-8}$
0.7 – 0.8	$1.51 \cdot 10^{-7}$	$\pm 3.7 \cdot 10^{-9}$	$\pm 4.2 \cdot 10^{-8}$
0.8 – 0.9	$9.68 \cdot 10^{-8}$	$\pm 2.0 \cdot 10^{-9}$	$\pm 2.7 \cdot 10^{-8}$
0.9 – 1.0	$6.01 \cdot 10^{-8}$	$\pm 1.9 \cdot 10^{-9}$	$\pm 1.7 \cdot 10^{-8}$
1.0 – 1.1	$3.44 \cdot 10^{-8}$	$\pm 9.3 \cdot 10^{-10}$	$\pm 9.6 \cdot 10^{-9}$
1.1 – 1.2	$2.12 \cdot 10^{-8}$	$\pm 9.3 \cdot 10^{-10}$	$\pm 5.9 \cdot 10^{-9}$
1.2 – 1.3	$1.24 \cdot 10^{-8}$	$\pm 4.7 \cdot 10^{-10}$	$\pm 3.5 \cdot 10^{-9}$
1.3 – 1.4	$8.58 \cdot 10^{-9}$	$\pm 4.3 \cdot 10^{-10}$	$\pm 2.4 \cdot 10^{-9}$
1.4 – 1.5	$5.63 \cdot 10^{-9}$	$\pm 4.8 \cdot 10^{-10}$	$\pm 1.6 \cdot 10^{-9}$
1.5 – 1.6	$3.33 \cdot 10^{-9}$	$\pm 3.0 \cdot 10^{-10}$	$\pm 9.4 \cdot 10^{-10}$
1.6 – 1.7	$2.01 \cdot 10^{-9}$	$\pm 2.4 \cdot 10^{-10}$	$\pm 5.8 \cdot 10^{-10}$
1.7 – 1.8	$1.36 \cdot 10^{-9}$	$\pm 2.4 \cdot 10^{-10}$	$\pm 4.0 \cdot 10^{-10}$
1.8 – 1.9	$9.03 \cdot 10^{-10}$	$\pm 1.9 \cdot 10^{-10}$	$\pm 2.7 \cdot 10^{-10}$

Bibliography

[1] V. F. Hess. Über Beobachtungen der durchdringenden Strahlung bei sieben Freiballonfahrten. *Phys. Z.*, 13:1084–1091, 1912.

[2] T. K. Gaisser. Cosmic rays at the knee. *astro-ph/0608553*, 2006.

[3] W.-M. Yao et al. Review of Particle Physics. *J. Phys. G*, 33:1, 2006.

[4] T. H. Johnson. The azimuthal asymmetry of the cosmic radiation. *Phys. Rev.*, 43(10):834–835, 1933.

[5] B. Wiebel-Sooth, P. L. Biermann, and H. Meyer. Cosmic Rays VII. Individual element spectra: prediction and data. *A&A*, 1997.

[6] J.R. Hoerandel. On the knee in the energy spectrum of cosmic rays. *Astropart. Phys.*, 19:193–220, 2003.

[7] T. K. Gaisser. personal communication, 2007.

[8] R. Abbasi et al. Observation of the GZK cutoff by the HiRes experiment. *ArXiv Astrophysics e-prints*, 2007.

[9] M. Roth et al. Measurement of the UHECR energy spectrum using data from the Surface Detector of the Pierre Auger Observatory. In *Proc. 30th ICRC*, Mérida, Mexico, 2007.

[10] T. Antoni et al. Kascade measurements of energy spectra for elemental groups of cosmic rays: Results and open problems. *Astropart. Phys.*, 24:1–25, 2005.

[11] H. Ulrich. Untersuchungen zum primären Energiespektrum der kosmischen Strahlung im PeV-Bereich mit dem KASCADE-Experiment. Doctoral thesis, Universität Karlsruhe, 2003.

[12] M. Unger et al. Study of the Cosmic Ray Composition above 0.4 EeV using the Longitudinal Profiles of Showers observed at the Pierre Auger Observatory. In *Proc. 30th ICRC*, Mérida, Mexico, 2007.

[13] A. M. Hillas. Cosmic Rays: Recent Progress and some Current Questions. *ArXiv Astrophysics e-prints*, 2006.

[14] A. Achterberg, Y. A. Gallant, J. G. Kirk, and A. W. Guthmann. Particle acceleration by ultra-relativistic shocks: Theory and simulations. *Mon. Not. Roy. Astron. Soc.*, 328:393, 2001.

[15] A. Weigert, H.J. Wendker, and L. Wisotzki. *Astronomie und Astrophysik: Ein Grundkurs*. Wiley-VCH, Weinheim, 2005.

[16] Wikipedia. Supernova — wikipedia, the free encyclopedia, 2007. URL `http://en.wikipedia.org/w/index.php?title=Supernova&oldid=175512443`. [Online; accessed 6-December-2007].

[17] P. L. Biermann. *Nucl. Phys. B*, 43:221, 1995.

[18] C. M. Urry and Paolo Padovani. Unified Schemes for Radio-Loud Active Galactic Nuclei. *PASP*, 107:803, 1995.

[19] V. Berezinsky, A. Z. Gazizov, and S. I. Grigorieva. Signatures of AGN model for UHECR. *ArXiv Astrophysics e-prints*, 2002.

[20] J. Abraham et al. Correlation of the highest-energy cosmic rays with nearby extragalactic objects. *Science*, 318:896–897, 2007.

[21] R. W. Klebesadel, I. B. Strong, and R. A. Olson. Observations of Gamma-Ray Bursts of Cosmic Origin. *ApJ*, 182:L85+, 1973.

[22] P. Meszaros. Gamma-ray bursts. *Rept. Prog. Phys.*, 69:2259–2322, 2006.

[23] J. Abraham et al. Properties and performance of the prototype instrument for the pierre auger observatory. *Nucl. Instrum. Meth.*, A523: 50–95, 2004.

[24] T. A. Ensslin, P. L. Biermann, U. Klein, and S. Kohle. Shock Waves of the Large-Scale Structure Formation in the Universe. *ArXiv Astrophysics e-prints*, 1998.

[25] M. Nagano and A. A. Watson. Observations and implications of the ultrahigh-energy cosmic rays. *Rev. Mod. Phys.*, 72(3):689–732, Jul 2000.

[26] J. Bagchi and et al. High & ultra-high energy cosmic ray acceleration in structure-formation shocks in Abell 3376 galaxy cluster. In *Proc. 29th ICRC*, volume 3, page 241, Pune, India, 2005.

[27] P. Bhattacharjee and G. Sigl. Origin and propagation of extremely high energy cosmic rays. *Phys. Rep.*, 327:109–247, 2000.

[28] A. Vilenkin and E.P.S. Shellard. *Cosmic Strings and Other Topological Defects.* Cambridge University Press, Cambridge, 2000.

[29] Andrew W. Strong, Igor V. Moskalenko, and Vladimir S. Ptuskin. Cosmic-ray propagation and interactions in the Galaxy. *Ann. Rev. Nucl. Part. Sci.*, 57:285–327, 2007.

[30] V. S. Ptuskin, S. I. Rogovaya, V. N. Zirakashvili, L. G. Chuvilgin, G. B. Khristiansen, E. G. Klepach, and G. V. Kulikov. Diffusion and drift of very high energy cosmic rays in galactic magnetic fields. *A&A*, 268: 726–735, February 1993.

[31] F. Aharonian et al. A low level of extragalactic background light as revealed by gamma-rays from blazars. *Nature*, 440:1018–1021, 2006.

[32] A. A. Arkhipov. The GZK Puzzle and Fundamental Dynamics. *ArXiv hep-ph e-prints*, 2006.

[33] E. G. Berezhko and H. J. Voelk. Spectrum of cosmic rays, produced in supernova remnants. 2007.

[34] S. I. Nikolsky. Break in the cosmic ray spectrum or confinement violation near 10^6 TeV? *Nuclear Physics B Proceedings Supplements*, 39: A228+, 1995.

[35] D. Kazanas and A. Nicolaidis. Cosmic Rays and Large Extra Dimensions. *General Relativity and Gravitation*, 35:1117–1123, 2003.

[36] B. Keilhauer. Investigation of Atmospheric Effects on the Development of Extensive Air Showers and their Detection with the Pierre Auger Observatory. Doctoral thesis, Universität Karlsruhe, 2004.

[37] T. K. Gaisser and A. M. Hillas. Reliability of the Method of Constant Intensity Cuts for Reconstructing the Average Development of Vertical Showers. In *International Cosmic Ray Conference*, volume 8 of *International Cosmic Ray Conference*, pages 353–+, 1977.

[38] L. Anchordoqui et al. High Energy Physics in the Atmosphere: Phenomenology of Cosmic Ray Air Showers. *Ann. Phys.*, 314:145–207, 2004. URL `http://www.citebase.org/abstract?id=oai:arXiv.org:hep-ph/0407020`.

[39] K. Kamata and J. Nishimura. *Progr. Theor. Phys. Suppl.*, 6:93, 1958.

[40] G. Navarra et al. KASCADE-Grande: A large acceptance, high-resolution cosmic-ray detector up to 10^{18} eV. *Nucl. Instrum. Meth.*, A518:207–209, 2004.

[41] N. Budnev et al. Tunka EAS Cherenkov Array – status 2001. In *Proc. 27th ICRC*, volume 2, page 581, Hamburg, Germany, 2001.

[42] D. Chernov et al. Primary energy spectrum and mass composition determined with the Tunka EAS Cherenkov Array. *Int. J. Mod. Phys.*, A20:6799–6801, 2006.

[43] M. Amenomori et al. Primary cosmic-ray energy spectrum around the knee energy region measured by the Tibet hybrid experiment. *J. Phys. Conf. Ser.*, 47:51–58, 2006.

[44] D. Heck, J. Knapp, et al. CORSIKA: A Monte Carlo Code to Simulate Extensive Air Showers. *Forschungszentrum Karlsruhe Report FZKA*, 6019, 1998.

[45] W. Ralph Nelson, H. Hirayama, and David W. O. Rogers. The egs4 code system. 1985. SLAC-0265.

[46] R. Engel, T.K. Gaisser, P. Lipari, and T. Stanev. Air shower calculations with the new version of SIBYLL. In *Proc. 26th ICRC*, Salt Lake City, 1999.

[47] S. Ostapchenko. Status of qgsjet. *AIP Conf. Proc.*, 928:118–125, 2007.

[48] S. Ostapchenko. High Energy Cosmic Ray Interactions - an Overview. In *Proc. TeV Part. Astrophys. II Workshop*, 2007.

[49] L. V. Gribov, E. M. Levin, and M. G. Ryskin. *Phys. Rep.*, 100, 1983.

[50] D. Heck and T. Pierog. *Extensive Air Shower Simulations with CORSIKA: A User's Guide.*

[51] A. Fasso et al. Fluka: a multi-particle transport code. *CERN*, 10, 2005.

[52] A. E. Hedin. Extension of the MSIS thermosphere model into the middle and lower atmosphere. *J. Geophys. Res.*, 96:1159–1172, 1991.

[53] A. Karle et al. IceCube - construction status and performance results of the 22 string detector. In *arXiv:0711.0353v1*, pages 7–10, Proc. 30th ICRC, Mérida, Mexico, 2007.

[54] J. Ahrens et al. Observation of high energy atmospheric neutrinos with the Antarctic Muon and Neutrino Detector Array. *Phys. Rev.*, D66: 012005, 2002.

[55] A. Achterberg et al. Five years of searches for point sources of astrophysical neutrinos with the AMANDA-II neutrino telescope. *Phys. Rev.*, D75:102001, 2007.

[56] M. Ackermann et al. Search for neutrino induced cascades with amanda. *Astropart. Phys.*, 22:127–138, 2004.

[57] J. Ahrens et al. Search for neutrino-induced cascades with the amanda detector. *Phys. Rev. D*, 67(1), 2003.

[58] J. Ahrens et al. Icecube preliminary design document. URL `http://www.icecube.wisc.edu/science/publications/pdd/`.

[59] A. Achterberg et al. First year performance of the icecube neutrino telescope. *Astropart. Phys.*, 26:155–173, 2006.

[60] M. Beimforde. Calibration of air shower signals in the IceTop detector using cosmic ray muons. Diploma thesis, Humboldt-Universität zu Berlin, 2006. URL `http://www-zeuthen.desy.de/nuastro/publications/diploma/arbeiten/ThesisBeimforde.pdf`.

[61] M. Ackermann et al. Neutrino Triggered Target of Opportunity (NToO) test run with AMANDA-II and MAGIC. In *arXiv:0711.0353v1*, pages 123–126, Proc. 30th ICRC, Mérida, Mexico, 2007.

[62] M. Ackermann. *Searches for signals from cosmic point-like sources of high energy neutrinos in 5 years of AMANDA-II data.* PhD thesis, Humboldt-Universität zu Berlin, 2007.

[63] T. Gaisser et al. Performance of the IceTop Array. In *arXiv:0711.0353v1*, pages 15–18, Proc. 30th ICRC, Mérida, Mexico, 2007.

[64] M. Gazdzicki and D. Roehrich. Pion multiplicity in nuclear collisions. *Z. Phys.*, C65:215–223, 1995.

[65] J. Ahrens et al. Measurement of the cosmic ray composition at the knee with the SPASE-2/AMANDA-B10 detectors. *Astropart. Phys.*, 21:565–581, 2004.

[66] C. Song et al. Cosmic Rays in IceCube: Composition-Sensitive Observables. In *arXiv:0711.0353v1*, pages 27–30, Proc. 30th ICRC, Mérida, Mexico, 2007.

[67] T. Kuwabara et al. Heliospheric Physics with IceTop. In *arXiv:0711.0353v1*, pages 19–22, Proc. 30th ICRC, Mérida, Mexico, 2007.

[68] S.R. Klein et al. Study of High p_T Muons in Air Showers with IceCube. In *arXiv:0711.0353v1*, pages 35–38, Proc. 30th ICRC, Mérida, Mexico, 2007.

[69] M. A. Lawrence, R. J. O. Reid, and A. A. Watson. The Cosmic ray energy spectrum above 4×10^{17} eV as measured by the Haverah Park array. *J. Phys.*, G17:733–757, 1991.

[70] L. Demirörs et al. IceTop tank response to muons. In *arXiv:0711.0353v1*, pages 47–50, Proc. 30th ICRC, Mérida, Mexico, 2007.

[71] T. K. Gaisser et al. IceTop: The Surface Component of IceCube. In *Proc. 28th ICRC*, Tsukuba, Japan, 2003.

[72] T. Stanev and R. Ulrich. IceTop Status in 2004. *ArXiv Astrophysics e-prints*, 2005.

[73] J. Allison et al. Geant4 developments and applications. *IEEE Trans. Nucl. Sci.*, 53(1):270–278, 2006.

[74] F. Kislat, S. Klepser, and A. Van Overloop. A lateral distribution function and fluctuation parametrisation for icetop. IceCube Internal Report 200702001, 2007.

[75] F. Kislat. Study of charge and time fluctuations of signals in the IceTop detector. Diploma thesis, Humboldt-Universität zu Berlin, 2006.

[76] S. Klepser et al. Lateral Distribution of Air Shower Signals and Initial Energy Spectrum above 1 PeV from IceTop. In *arXiv:0711.0353v1*, pages 43–46, Proc. 30th ICRC, Mérida, Mexico, 2007.

[77] T. Waldenmaier. personal communication, 2007.

[78] J. Ochab. Test of shower reconstruction procedures with the IceTop A, IceTopB subarrays. Internal Report, 2007. URL `https://docushare.icecube.wisc.edu/dsweb/Get/Document-45320/ABanalysis%_final.ps`.

[79] R. Glasstetter et al. Analysis of electron and muon size spectra of eas. In *Proc. 26th ICRC, Salt Lake City, USA*, 1999.

[80] G. D'Agostini. A Multidimensional unfolding method based on Bayes' theorem. *Nucl. Instrum. Meth.*, A362:487–498, 1995.

[81] R. Gold. *Argonne National Laboratory Report ANL-6984*, 1964.

[82] B. Efron and R.T. Tibshirani. *An introduction to the bootstrap.* Chapman & Hall/CRC, London, 1998.

[83] Internet Database, 2007. URL `http://amrc.ssec.wisc.edu/index.html`.

[84] L. Demirörs. personal communication, 2007.

[85] N. M. Budnev et al. Cosmic ray energy spectrum and mass composition from 10**15-eV to 10**17-eV by data of the Tunka EAS Cherenkov array. 2005.

[86] J. A. Ortiz, G. A. Medina Tanco, and V. de Souza. Longitudinal development of extensive air showers: Hybrid code SENECA and full Monte Carlo. *Astropart. Phys.*, 23:463–476, 2005.

[87] I.N. Bronshtein et al. *Handbook of Mathematics.* Springer, Berlin, 1998.

[88] T. Feusels, F. Kislat, S. Klepser, and A. Lucke. personal communication, 2007.

Abbreviations

AGN	Active galactic nucleus
ATWD	Analogue transient waveform digitiser
COG	Center of gravity
DAQ	Data acquisition
DLP	see eq. 5.8
DOM	Digital optical module
EAS	Extensive air Shower
EBL	Extragalactic background light
EeV	Exaelectronvolt, 10^{18} eV
eV	Electronvolt, $1.602 \cdot 10^{-19}$ J
FPGA	Field Programmable Gate Array
GeV	Gigaelectronvolt, 10^{9} eV
GRB	Gamma ray burst
GZK Cutoff	Greisen-Zatsepin-Kuzmin Cutoff
HG	High gain, operation mode of a DOM
LC	Local coincidence (of two tanks)
LG	Low gain, operation mode of a DOM
LDF	Lateral distribution function
Llh	Log-Likelihood
MC	Monte Carlo = simulation
MeV	Megaelectronvolt 10^{6} eV
NKG	see eq. 1.10
PeV	Petaelectronvolt 10^{15} eV
PMT	Photomultiplier tube
SMT	Simple majority trigger
TeV	Teraelectronvolt 10^{12} eV
VEM	Vertical equivalent muon

Alphabetical Index

Acknowledgements

I would like to thank Prof. Dr. Hermann Kolanoski, who was a Doktorvater wie er im Buche steht in all of the 38 months I was working with him. His profound knowledge of data analysis and weekly inquisition (in statistics) were essential for almost every plot in this thesis.

I always felt well supported by Dr. Stefan Schlenstedt and Dr. Christian Spiering, who both in their manner were good and understanding leaders of the astro-particle group in Zeuthen.

For his creative physical input and supporting me on my way to South Pole, I would particularly like to thank Prof. Dr. Tom Gaisser. Admitting us to the cosmic ray working group and sharing his experience and open mind taught us to be astro-particle physicists.

Four diploma students and a summer student made the Zeuthen CR group and gave endless help and insight concerning our detector, and my code. Therefore I am very thankful to have had the opportunity to supervise and work with Michael Beimforde, Fabian Kislat, Adam Lucke, Jeremi Ochab and Frigga Wendt.

Inside the cosmic ray working group, and besides the people mentioned above and below, I am thankful for the help and exchange with Dr. Xinhua Bai, Dr. Dima Chirkin, Tom Feusels, Dr. Tonio Hauschild, Prof. Dr. Katherine Rawlins, and Prof. Dr. Todor Stanev. My special thanks go to Dr. Sacha and Stoyan Stoyanov, Dr. Serap Tilav and Dr. Shijtan, who generously welcomed me and my family in their homes in Newark, Delaware.

In addition, the discussions with Prof. Dr. Karl-Heinz Kampert, Dr. Ralph Engel, Dr. Markus Roth, Dr. Holger Ulrich and Dr. Michael Unger were most inspiring and helpful.

The social environment among the Diploma/PhD/Postdoc-people in Zeuthen was exceptional during all the time it took care of me. Among the many people I met, I would especially like to thank Markus Ackermann, Jose Luis Bazo Alba, Jens Berdermann, Sebastian Böser, Martin Bothe, Robert Franke, Jan Kretzschmar, Raphael Lang, Robert Lauer, Eike Middell, Sirin Odrowsky, Sebastian Panknin, Damian Pieloth, Konstancja

Satalecka, Lazar Staykov, Bernhard “Ich hab da n Vorschlag, der fängt mit p an und hört mit ython auf” Voigt, Oxana Tarasova, Martin Tluczykont, Delia Tosi and Henrike Wissing for discussions, evenings and the patience of proof-reading this thesis. Also, I am very thankful to the excellent an honourable guy that I eventually forgot to mention here.

Big parts of the thesis were written in the library of the Humboldt-Universität zu Berlin, a charming place I am thankful to have been able to use. Even more charming was the food at lunch, which I dealt with in close collaboration with the groups of Dr. Marek Kowalski and Prof. Dr. Thomas Lohse, who I want to thank as well.

In preparation of my South Pole Travel, the advice of Paul Evenson, James Roth and Len Shulman was a most valuable input. During my stay there, the exchange with Paul McGuire and Mike Kleist was probably what kept me sane.

Elisa Bernardini, Julien Bolmont, Matthias Füßling and Matthias Kerschhaggl have been very enjoyable hostel and travel mates in Mérida, Mexico and around. I want to thank them for making an otherwise stressful journey a pleasant and long-lasting memory.

For more than three years, the IceCube family surrounded me, and most of the time it was rather good to me. I am exceedingly thankful to have made the acquaintance of Levent Demirörs, Peter Nießen, Elisa Resconi, Tilo Waldenmaier, Chris Wendt and Arne van Overloop.

I would also like to thank my parents for continuously keeping me solvent throughout my studies and never admitting any doubt about the profit of education (Maybe now?).

Finally, I would like to thank Sabine, my beloved wife, for sharing her beautiful mind, and little Zora, whose smile is just the best thing on Earth to talk about in the last wink of a thesis.

·א·

Selbständigkeitserklärung

Hiermit erkläre ich, die vorliegende Arbeit selbständig und ohne fremde Hilfe verfasst und nur die angegebene Literatur und Hilfsmittel verwendet zu haben. Ich habe mich nicht anderweitig um einen Doktorgrad beworben und besitze keinen Doktorgrad. Die Promotionsordnung der Mathematisch-Naturwissenschaftlichen Fakultät I der Humboldt-Universität ist mir bekannt.

Berlin, den 24.04.2008

Stefan Klepser